

A Thesis Submitted for the Degree of PhD at the University of Warwick

Permanent WRAP URL:

<http://wrap.warwick.ac.uk/106751>

Copyright and reuse:

This thesis is made available online and is protected by original copyright.

Please scroll down to view the document itself.

Please refer to the repository record for this item for information to help you to cite it.

Our policy information is available from the repository home page.

For more information, please contact the WRAP Team at: wrap@warwick.ac.uk

THE BRITISH LIBRARY DOCUMENT SUPPLY CENTRE

TITLE Development of a crossed beam instrument
for studying ion-molecule
reactions

AUTHOR John Roland Trainor

INSTITUTION
and DATE University of Warwick
1970

Attention is drawn to the fact that the copyright of
this thesis rests with its author.

This copy of the thesis has been supplied on condition
that anyone who consults it is understood to recognise
that its copyright rests with its author and that no
information derived from it may be published without
the author's prior written consent.

THE BRITISH LIBRARY
DOCUMENT SUPPLY CENTRE

500000 Ave, Wakefield
West Yorkshire
United Kingdom



REDUCTION X

20

CAMERA

3



**Development of a crossed beam instrument
for studying ion-molecule
reactions**

by

John Roland Trainor

**A thesis submitted for the degree of
Doctor of Philosophy**

**Department of Chemistry
University of Warwick
Coventry, CV4 7AL
England**

January 1990

The following extract is from the opening scene of act one of "Rosencrantz and Guildenstern are dead" Tom Stoppard, Faber (1987).

Rosencrantz and Guildenstern have been tossing coins and betting on the outcome.

Some eighty coins have come down heads consecutively...

ROS: Heads. Getting a bit of a bore, isn't it?

GUIL: A bore?

ROS: Well...

GUIL: What about the suspense?

ROS: What suspense?

GUIL: It must be the law of diminishing returns....I feel the spell about to be broken

Index of contents

Title page
Index of contents
List of figures, tables and plates
Acknowledgements
Declaration
Glossary of symbols and abbreviations
Abstract

Chapter 1: INTRODUCTION

1	Interest in ion-molecule interactions
1	The importance of theory
3	Generalities on structure and reactivity
3	Clusters
3	Discrete particles
3	Size and symmetry
4	Larger small molecules and ions
5	Branching and stereochemistry
5	Electronic structure and potential energy surface effects
6	Comment
7	Techniques in the study of ion-molecule chemistry
7	General
8	Swarm methods
9	Mass spectrometric techniques
12	Resonant methods and ion trapping
13	State selected chemistry and laser applications
16	Beam experiments
19	The crossed beam experiment
21	Key equations of reactive scattering
26	Requirements of the crossed beam experiment

27	Crossed ion-neutral beam instruments
28	Chemical dynamics using crossed beams
28	(Ne + H ₂) ⁺ bench mark reactions of group 18
30	4-centre reactions of CO ⁺ with O ₂ and NO
33	Reactions on surfaces with a double potential minimum well
34	Kinetic spectroscopy in charge transfer reactions
36	Reactions of doubly charged ions
37	Reactions of polyatomic ions
37	Aims

Chapter 2: EXPERIMENTAL

39	Description of the instrumentation
39	The crossed beam apparatus
39	Vacuum system
40	The neutral beam vacuum test cell
40	Construction and performance
41	Operation
41	The gas handling inlet system
40	Construction (figure 8)
42	Modes of operation
42	Detection
42	The ion detector
43	TOF analysis of the neutral beam
44	Beam generation
44	Ion beam generation
44	The generation of a neutral beam
45	Electronic apparatus and detection
45	Free electrodes
45	The electrostatic octopole
46	Alignment

46	Computation of ion energy spectra
47	Analysis of errors
50	General experimental practice
51	Computer programs for simulation and data transfer
51	Supplement 1: Setting up the pulsed valve
51	Silicone procedure
52	Ribbon installation notes
52	Supplement 2: A jet test for nozzles
53	Supplement 3: The line of sight experiment
Chapter 3: ION OPTICS	
54	Introduction to ion optics
54	Concepts of electrostatic ion optics
54	Historical basis
58	The equivalent lens
67	The paraxial ray equation
68	The potential field
59	Computer modelling of trajectories
60	Aberrations: operation of a real lens
61	Electrodynamic fields: operation of the quadrupole mass filter
64	Real quadrupoles
66	Performance, observations, results and discussion
67	Stability and reproducibility
68	Electrons in the quadrupole
71	Ion energy
73	The effect of the RPD
77	The performance of the ion beam
77	Evidence of scattering in two body crossing experiments
78	Recommendations

78	Detector modifications
78	Ion beam source modifications
80	Conclusions
Chapter 4: NEUTRAL BEAM	
82	Introduction gas dynamics
84	Overview of pulsed beam sources
85	Elements of gas dynamics
85	Continuum fluid
86	Continuum steady flow mass rate
87	Terminal velocity of the beam
90	Skimmers
91	Considerations on incorporating the beam into the main apparatus
91	Mechanical considerations
92	Calculation of the pumping speed availability
95	Development of a simple motor valve
95	Preamplification
95	Magnetic flux
96	Pulsed source control unit
96	Nozzle
97	Valve body
99	Geometric considerations of the design specifications
99	Nozzle
100	Skimmers and turret
102	Loss calculations
104	Performance
104	Model for the pulsed beam shutter envelope
104	Preliminary considerations
107	An impulsively driven harmonic oscillator

109	The biased SHO model
110	Real biased oscillator
112	Bursting force on the ribbon
115	Forces acting on the ribbon to oppose opening
115	The barrier energy
116	Discussion
116	Mechanisms of loss
116	Frequency dependence of the pulse
117	The deposited substance underneath the nozzle
118	Secondary pulses
118	Performance of the model
119	Prognosis
119	Pulse trailing edge
120	Calculation of the flow field properties
120	Measurement of the distribution of velocities function
121	Quitting surface and sudden freeze
121	Conclusion

Chapter 8: CONCLUSIONS

124	Summary of the positive aspects of this work
124	Prognosis for the neutral beam model
124	Prognosis on chemistry
126	Summary of conclusions (further work)
127	Final comments

APPENDIX 1: REFERENCES

APPENDIX 2: DESIGN DRAWINGS

APPENDIX 3: COMPUTER PROGRAMS

List of figures, tables and plates

Chapter 1: INTRODUCTION

- 2 **Figure 1.1:** Pictorial representation of the driving forces to the study of reactions with microscopic resolution.
- 7 **Figure 1.2:** Representation of the relationships between various differential cross sections and the thermal rate constant.
- 20 **Figure 1.3:** Newton diagrams to illustrate some of the experimental conditions in vector space.
- 24 **Figure 1.4:** Diagrams to illustrate how isotropic distribution of product flux into $l(\theta)\sin(\theta) d\theta$ leads to a build up of polar intensity
- 24 **Figure 1.5:** Diagram to show the significance of symmetry in the Newton diagram.
- 33 **Figure 1.6:** The reaction coordinates for $\text{NH}_3^+ + \text{D}_2$ and $\text{Li}^+ + \text{RX}$ (alkyl halides).
- 26 **Table 1.1:** Conditions required for a crossed beam experiment.

Chapter 2: EXPERIMENTAL

- 39 **Figure 2.1:** Diagram of the instrument from above and below as a third angle projection.
- 40 **Figure 2.1a:** Diagram of the main components of the apparatus inside the vacuum chamber.
- 40 **Figure 2.2:** The neutral beam vacuum test cell.
- 41 **Figure 2.3:** Circuit diagram for the pulsed beam control unit.
- 41 **Figure 2.4:** The schematic lay out of the gas handling inlet system.
- 42 **Figure 2.5:** Diagram showing the detailed construction of the rotatable ion detector.
- 44 **Figure 2.6:** Some configurations of the ion beam source used in this work.
- 44 **Figure 2.6 (continued):** Three configurations of the octopole.

- 45 **Figure 2.7:** Block diagram of the electronic controller interconnections.
- 45 **Figure 2.8:** Diagram of the triggering sequences for a crossed beam experiment using a pulsed neutral beam.
- 45 **Figure 2.9:** Logic of data collection for experiments such as figure 2.8.
- Figure 2.10:** There is no figure 2.10.
- 45 **Figure 2.11:** Circuit diagram for the precision ramp generator.
- 45 **Figure 2.12:** Circuit diagram for the 9301 preamplifier and power supplies.
- 45 **Figure 2.13:** Circuit diagram for the FIG preamplifier and power supplies.
- 45 **Figure 2.14:** Circuit diagram for the buffer amplifier of the precision ramp generator.
- 50 **Figure 2.15:** Spare data sheet.
- 40 **Plate 1:** Photograph of the main components of the apparatus.

Chapter 3: ION OPTICS

- 57 **Figure 3.1:** Ray diagrams to illustrate the cardinal points in an equivalent lens P,P' - principal points, N,N' - nodal points and F,F' - focal points.
- 59 **Figure 3.2:** Diagram to show the network established for a computer calculation of the electric field gradient.
- 61 **Figure 3.3:** Ray diagrams to illustrate the exaggerated effects of space charge, spherical aberration and chromatic aberration.
- 64 **Figure 3.4:** Diagram to show the stability regions in an operating quadrupole mass filter.
- 66 **Figure 3.5:** Mass spectrum of Air/He.
- 68 **Figure 3.6:** Mass spectra recorded of Air, He and H₂.
- 68 **Figure 3.7:** Mass spectrum of CS₂.

- 66 **Figure 3.8:** Angular profile showing poor collimation and the spherical aberration.
- 66 **Figure 3.9:** CS^+ energy profile.
- 68 **Figure 3.10:** A diagram showing the decoupling collar in the gap between the quadrupole and the octopole.
- 69 **Figure 3.11:** The ion source.
- 69 **Figure 3.12:** Plots of electron trajectories over a simulated electrode array for modelling the operation of the ion source.
- 69 **Figure 3.13:** Plots of electron trajectories over a simulated electrode array for modelling the operation of the ion source. Showing the focussing of electrons into the QMF entrance plate.
- 69 **Figure 3.14:** Plots of electron trajectories over a simulated electrode array for modelling the operation of the ion source.
- 71 **Figure 3.15:** Ion energy profiles indicating the improvement of resolution obtained when the QMF is earthed.
- 72 **Figure 3.16:** Ion energy profiles for standard conditions with and without the a RF only QMF.
- 72 **Figure 3.17:** Ion energy profiles for CS^+ with the source recessed from the QMF.
- 73 **Figure 3.18:** Diagram to show how a RF modulated field can induce changes in ion energy.
- 73 **Figure 3.19:** A series of experimental results exposing a systematic error in the RPD analyser.
- 74 **Figure 3.20:** SIMION plots of 143 ion trajectories over a simulated RPD electrode array.
- 75 **Figure 3.21:** Performance plots for the RPD model.
- 75 **Figure 3.22:** Performance plots for the RPD model.
- 75 **Figure 3.23:** Fitting plots using the RPD model.
- 75 **Figure 3.24:** Fitting plots using the RPD model.

- 76 Figure 3.25: Data showing the power of resolution and pole bias in masking detector aberrations.
- 77 Figure 3.26: Integral ion energy profile showing the extreme selectivity towards mass selected ions possible.
- 77 Figure 3.27: Angular and energetic evidence for ~~slow~~ ^{slow} number of ion-molecule collisions.

Chapter 4: NEUTRAL BEAM

- 88 Figure 4.1: A cross section from a sonic nozzle giving rise to a free jet expansion.
- 91 Figure 4.2: An exploded view of the pulsed beam source.
- 91 Figure 4.3: Diagram to represent the neutral-beam differentially pumped vacuum chamber.
- 96 Figure 4.4: A schematic representation of the relative pulse shapes and pulse heights, between the PSCU of Gorry and the original PSCU of the Warwick.
- 97 Figure 4.5: A sketch of the sort of result obtained, using the water jet test, if the nozzle is not aligned.
- 99 Figure 4.6: A cross section of the pulsed beam nozzle with a supposed shock structure drawn on.
- 103 Figure 4.7: A reproduction of a Polaroid photograph of > 4500 pulses.
- 103 Figure 4.8: Two pulses, A and B, recorded and archived using the DBA 524A in digital averaging mode.
- 103 Figure 4.9: A plot of the background pressure in the pulsed beam vacuum test cell versus a function of the driving pulse energy.
- 104 Figure 4.10: Diagram showing a control volume around the nozzle which would be used in momentum equation calculations of the flow properties of the beam.

- 105 Figure 4.11: A plot of the bottle neck in the conductance of the pulsed valve versus the height above the valve seat.
- 109 Figure 4.12: A diagram to show the simple harmonic oscillator model and the effect of applying a barrier or bias.
- 112 Figure 4.13: Diagram showing a) the relationship of forces acting on the ribbon, b) the sections drawn for the magnetic field in a calculation (see text).
- 114 Figure 4.14: Oscilloscope polaroid photograph of the electronic impulse from the PSCU. Compare to figure 4.4.
- 118 Figure 4.15: Plot of the leading edge of the pulse shown in figure 4.8b, the data is reduced and superimposed on to a plot of $\sin^3 \theta$.
- 118 Figure 4.16: a) Plot of the leading edge of the pulse shown in figure 4.8a, the data is reduced and superimposed on to a plot of $\sin^3 \theta$. b) Plot $\sin^3 \theta$ of vs the leading edge of figure 4.8a. θ is derived from the points for which data is available, and the data is in reduced units.
- 88 Table 4.1: Comparison of four valve types.
- 100 Table 4.2: Sample calculations of the α, β, γ angles as a function of P .
- 104 Table 4.3: Measured and calculated quantities in the determination of the ribbon lifting force.
- 91 Plate 2: Photograph of the assembled pulsed valve.
- 82 Plate 3: Photograph of the pulsed beam stagnation chamber and adjuster.

Acknowledgements

The final form of this project has been moulded with the help and influence of many different people. I would like to thank the following people.

Dr D.M. Hirst - For introducing me to the fascinating subject of reaction dynamics. The inspiration for this project comes from him.

Professor P.J. Derrick and Professor K.R. Jennings - for advice.

SERC - for providing an equipment grant and studentship.

Harry Wiles and the staff of the mechanical workshop - for fabricating some of the designs described in this thesis and for allowing me to use some of the machines in the workshop.

Pat McCheaney and Mark Thomas in the electronic workshop - for some design and fabrication work, and for rapidly repairing deceased or ailing equipment.

Alex Colburn - my particular thanks for his assistance and companionship, and all his intelligent comments.

Dr A. O'Hagan (Statistics), **Dr M.G. Dowsett** (Physics), **Dr A.P. Boldy** and **Mr C.J. Carpenter** (Engineering), **Dr J.C. Whitehead** (University of Manchester) and **Dr M.J.C. McCoustra** (University of East Anglia) for useful discussions.

Dr P.A. Gerry (University of Manchester) - for his cooperation during a visit to his laboratory

Dr G. Dolnikowski - for introducing me to SIMION.

Dr S.D. Kelly -for basic training in the early stages.

Dr D.P. Newton - thanks for nothing.

Dr R.G. Whytaker - for reading the manuscript.

Mr S. Davies - for putting the finishing touches to the manuscript.

Mr R. McCleod - for his excellent photographs (costing an arm and a leg).

Dr A.P. Hill and Professor D.H.G. Creut - for the use of Macintosh in
preparing this manuscript.

Reminder - for her support and help with checking and collating the references.

To all my colleagues for their companionship in the pubs and bars of Warwickshire.

Declaration

All of the work described in this thesis is original and has been conducted solely by the author, except where indicated by reference to other sources.

J.R. Trainor (January 1990)

Glossary of symbols and abbreviations

a	Dimensionless parameter in the Mathieu equations
A	A scaling parameter for ion flux
A	An unspecified elemental particle
AC	Alternating current
B	An unspecified elemental particle
C	An unspecified elemental particle
C ₁	Symmetry group equivalent to having no symmetry, the element equivalent C ₁
CEM	Channel electron multiplier
CI	Chemical ionisation
CID	Collision induced decomposition
CM	Centre of mass
CT	Charge transfer
DC	Direct current
DOOS 3.3	Disc operating system (version 3.3)
e	The fundamental unit of charge
E	Energy
E _i	Electric field gradient in the direction of some specified i
E _T	Translational energy content
EE	Electron energy
e/m	Charge to mass ratio (one unit of charge)
F	Focus potential
F	Force
FA	Flowing afterglow
FD	Field desorption
FWHM	Full width half maximum
Group 18	IUPAC nomenclature for noble gas group.

GU	Grid unit
HR	High Rydberg
I	Intensity
I _E	Internal energy content
I(v)	An unknown function of voltage
ICR	Ion cyclotron resonance
J(v)	An unknown function of voltage
l	path length
LIF	Laser induced fluorescence
M	Generalised molecule or atomic species
M _e	Mass of an electron
M _i	Mass of an ion
MIKES	mass analysed kinetic energy spectroscopy
MS	Mass spectrometer, mass spectrometry
M	Mass
n	Refractive index
n _B	The number density per unit volume of the target. (beam)
Nb	Any noble gas
P	State symbol
P+	Product ion configuration considered
q	Dimensionless parameter in the Mathieu equations
Q	Charge on an ion in units of e
QMF	Quadrupole mass filter
Q _{max}	Maximum exoergicity
Q _{min}	Minimum exoergicity
REMPI	Resonance enhanced multi-photon ionisation
RF	Radio frequency
RPD	Retarding potential difference (energy analyser)
CHFC	Oxygen-free copper? oxygen free high conductivity

s	a distance
S	the action of a particle
SIMION	Ion trajectory simulation computer program
SIFDT	Selected ion flow drift tube
SIFT	Selected ion flow tube
r	A distance along a radial line in cylindrical polar coordinates
r_0	The minimum distance from the axis to the rod surface in a quadrupole
t	Time
TESICO	Threshold electron secondary ion coincidence
TOF	Time of flight
U	DC voltage
U	A velocity in the CM.
V	RF voltage
V	A velocity in the Laboratory frame of reference.
$V(t)$	A threshold energy
v_r	V_E
v_r	Initial relative velocity
V	An electrostatic potential
V_{DC}	DC voltage
V_{RF}	RF voltage
VG	Vacuum Generators Ltd
wpi	Wires per inch
x	A count rate
\bar{x}_1	Average value x_1 and with a probable error is $\sqrt{x_1}$
x	A coordinate axis in cartesian form
X	Product particle
X	Poisson's random variable
XA	Position of an aperture stop
y	A coordinate axis in cartesian form

Y	Product particle
γ_A	An aperture diameter
z	A coordinate axis in cartesian form
z	A coordinate axis in cylindrical polar form
α	Polarisability of a species
ϵ_0	Permittivity of free space.
ξ	Parameter in the Mathieu equations
λ	A sweep width \times channel width $\times \sum a_l(v)$ for all v .
μ	Reduced mass
σ	Full soft sphere cross section
σ_L	Langevin cross section
ϕ	The electrostatic potential
ϕ'	The electrostatic potential differentiated with respect to z
ϕ''	The electrostatic potential twice differentiated with respect to z
ϕ	A diameter measurement
$\phi(t)$	A time dependent potential field
Φ	Azimuthal polar angle θ_{ϕ}
Θ	Meridional polar angle θ_{θ}
ΔH_r	Change in the state function: enthalpy of reaction
ΔJ	Change in angular momentum quantum number

Abstract

This thesis describes the development of a Crossed Beam Instrument for the study of ion-molecule reactions. A full investigation of some gross systematic errors, in apparatus which had been previously installed, is made. Where time has prevented the further development, then conclusions have been transformed into specifications, and practical solutions described. Experimental data is presented which is interpreted as evidence that the beams intersect and that low intensity of the scattered products and the forementioned systematic errors veil these data. The reduction of data, containing such errors, to useful chemical interpretation is extremely difficult, hence the need for further modification.

Data are presented in chapter 3 consistent with the quadrupole acting as a linear particle accelerator. The effect on an initially monochromated beam is of causing an unacceptable energy spread. The spherical and chromatic aberrations of both source and detector are identified as the principal systematic errors using computer simulation (SIMION) for forward convolution.

The development of a pulsed neutral beam source is described in chapter 4. The performance of the beam source is critically analysed and compared to alternative sources. A generally applicable model is derived to predict the shutter opening function of pulsed sources. Such a study has not previously been made. It is anticipated that this model will be of use to the solution of non-steady flow problems i.e. calculation of time dependent flow field properties, or in the deconvolution of TOF spectra from beam sources. Performance data for the beam source and some calculated properties are given.

The subject of ion-molecule reactions is introduced by development from simple ideas. The subject matter covered is not intended to be exhaustive, but covers the examples of ion-molecule reactions of personal interest. Recent crossed beam studies are examined and suggestions of possible new experiments made.

1



INTRODUCTION

Interest in ion-molecule interactions

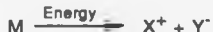
As energy is added to matter, characteristic changes are observed from solid to liquid and gas ¹. Injection of sufficient energy will result in plasma formation by the detachment of an electron:

[1]



or by some dissociative process eg. ion pair formation:

[2]



The ionisation or dissociation energy is analogous to the latent heat and hence such plasmas can be described as a fourth state of matter. In the presence of a large density of energy, ionisation will occur: ions are formed in nuclear reactions, mainly as by-products, and in flames where ion processes are important in flame propagation and combustion. These examples have sufficient exoergic energy releases to support ion formation.

Ions which persist for a long period of time have a high probability of interaction with a second particle. These bimolecular interactions are the basis of gas phase ion-molecule chemistry and have a general significance in the physical and applied sciences. Detailed study of ion chemistry provides data and techniques useful to disciplines as diverse as engineering (eg. combustion efficiency, semiconductor manufacture) and astronomy (eg. planetary atmospheres, solar wind etc.).

The importance of theory

Single measurements or results are rarely significant in any scientific discipline. Placed in the proper context amongst analogous data, the importance can

be seen by comparing and contrasting results. This practice makes theoretical predictions possible, i.e. demonstration of a quantitative understanding of unknown systems. The testing of theories is in itself an important driving force in science. This is particularly true for the type of chemical physics related to ion-molecule reactions, since questions are posed about the very nature of reactivity.

The first theory of ion-molecule reactions was formulated to explain the variation in kinetic rates of reaction in the gas phase. The model is taken from *Langevin theory* ² and describes the interaction of a structureless ion with a polarisable molecule. The resulting *Langevin equation* ³ has formed the basis a number of subsequent and improved theories ^{4,5}.

[3]

$$\sigma_L = \frac{2\pi Q}{(4\pi\epsilon_0)v_r} \left[\frac{\alpha}{\mu} \right]^{\frac{1}{2}}$$

Langevin cross section σ_L , Q = charge on the ion in units of e (the fundamental unit of charge), α = polarisability of the neutral species, μ = reduced mass, v_r = initial relative velocity, ϵ_0 = permittivity of free space.

Theoretical explanations of macroscopic (bulk) and microscopic (molecular level) behaviour are prominent in the literature ³⁻¹⁷. Early empirical and analytical theories have been superseded by complex theories upon the advent of powerful, fast computers. The growth of modeling, using detailed many state quantum dynamical ¹⁸ and trajectory calculations ^{14,16,26} on accurate *ab initio* potential surfaces ⁸⁻¹⁰, has produced a technology lag. Reducing the gap between the most advanced state-to-state calculations and what can be done to validate them by quantitative experiment, remains a principal driving force to the study of reaction dynamics.

This section is summarised by figure 1.1.

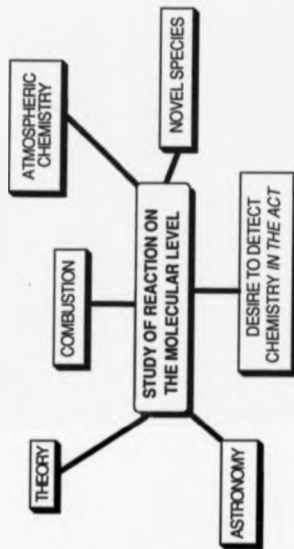


FIGURE 1.1: PICTORIAL REPRESENTATION OF THE DRIVING FORCES TO THE STUDY OF REACTIONS WITH MICROSCOPIC RESOLUTION

Generalities on structure and reactivity

The types of chemical species studied in the gas phase can be grouped into three categories: clustered molecules, neutrals and ions. Clusters may be charged or uncharged, but are worthy of separation from the other categories. The neutral and ionic groups can be further subdivided into open- and closed-shell reactants, and each includes monatomic species.

Clusters

The newest of the three fields is that of cluster chemistry ^{18,19}. A rapid growth in research effort has been directed by the semiconductor industry. This growth is due mainly to the search for moieties with properties intermediate between the bulk and the molecular. Properties of clusters do appear to be different: cluster formation is dominated by the so called *magic number* stability ^{19,53}. The chemical reactions of a substrate chemisorbed to a clustered molecule have energetics governed by the binding energy of the cluster, weighed against the energetics of the adsorbate undergoing a change ⁵³.

Discrete particles

Chemistry amongst discrete species is determined by a number of constraints:

Size and symmetry

Reactions between particles including only a small total number of atoms, often display pronounced selectivity between different reaction channels. The selectivity is caused by symmetry constraints in the part of the reaction co-ordinate leading to a minimum separation between the ^{REACTANTS} ~~reactants~~. Consideration of the least symmetric intermediate is required to map reactants on to products via the relevant angular momentum coupling schemes ²⁰, selection rules ²¹ and quantum state and molecular orbital correlations ^{22,23}.

One particular case is of interest. When a small molecule or ion includes a heavy atom this also means the presence of a large orbital angular momentum ²⁴. The reaction dynamics can be complicated considerably because of coupling of angular momenta, especially in the case of angle-resolved scattering studies. To a first approximation in the analysis of differential scattering data, the angular and kinematic parts of the potential are separable ²⁵. The approximation breaks ²⁶ down when coupling between the different angular momenta occurs i.e. the torque caused by high impact parameter collisions, orbital and rotational angular momenta. Iterative routines for the deconvolution of centre of mass (CM) scattering data have been developed ²⁷ to recover the correct differential cross sections from the CM data.

Larger small molecules and ions

As mentioned above the least symmetric combination of collision partners governs the symmetry restrictions on reaction. As the total number of atoms included in a reaction increases, then the least symmetric combination falls rapidly to C_1 . Symmetry restrictions are not often seen for reactions involving more than about ten atoms in total. Combinations of reactants with as few as four atoms may have a least symmetric geometry along the reaction coordinate of C_1 ²⁸. A large number of internal energy modes, such as is available to polyatomic species, generally extends the lifetime of a particle which has gained sufficient energy to dissociate. This effect can be predicted from the Ramsperger-Rice-Kassel-Marcus (RRKM) expression for the expectation lifetime of a particle undergoing a unimolecular decay ⁷.

Reactant internal energy also has a strong effect on reducing local symmetry particularly through vibration ²⁹.

Branching and stereochemistry

Molecular collisions in which the combined number of atoms in the reactants is large have chemistry governed by alternative constraints to symmetry. Many more competing channels in the chemistry may be observed. The formation of products by different routes is affected by the thermochemistry and by a new constraint caused by their larger size i.e. stereochemistry ³⁰.

Electronic structure and potential energy surface effects

Molecular neutrals and ions are termed closed shell if the outermost occupied principal electronic shell (valence shell) is complete. The neutral and ionised closed shell species have differences in electronic structure. Incomplete or open valence shell species also display electronic differences. The salient differences between these types can be summarised.

Neutral molecules with closed principal electronic shells, generally have a ground electronic potential energy surface (X -state) which is well separated from the excited states. Excited states are termed A, B, C, \dots etc. in ascending order of energy above that of the ground state. The separability of the states makes this type of molecule accessible to state selection; ~~and~~ this property has been exploited by chemists in exciting selected transitions using narrow band widths of laser light ^{31,32}.

In contrast, ionisation of a species causes contraction of molecular size and of the gap between electronic states. The influence of the large number of low lying excited electronic states on the chemistry of an ion compared to an iso-electronic neutral is to reduce the threshold energies at which branching reactions, avoided crossings and intersections of potential surfaces will alter the dynamics. For example a simple chemical reaction involving only two particles and three atoms ($A + BC$)^{*}, there exist two electronic potential manifolds for each set of reactants:

[4]



[5]



Moieties which have incomplete electronic shells may experience small barriers in the reaction coordinate. Some even have no barrier at all in excess of any endoergicity of the reaction ³³. The reactions of small molecules with open shell configurations therefore, can proceed upon every collision.

There are more differences in the typical electronic structures of open shell moieties: many of the higher electronic states may be degenerate. In cases such as Ar^+ and Cl which are iso-electronic, the ground electronic configuration has two spin orbit states ($2P_{3/2}$, $2P_{1/2}$) which are close to degenerate:



The nature and position of barriers and wells on an adiabatic reaction surface determine the gross energy requirements. An early barrier in the entrance valley of a surface will be surmounted efficiently by kinetic energy alone. Those surfaces with late barriers (eg. the microscopic reverse case of the above) are more efficiently surmounted by internal energy. This behaviour can lead to an increase or decrease of two orders of magnitude in rate of reaction, for the addition of a single quantum of vibrational energy per molecule. Large differences are still seen, even if the total energy content of the reactants (kinetic + internal) is kept constant.

Comment

In addition to the general scheme outlined above, detailed consideration of the energy disposal must be considered in interpreting reaction data. The microscopic

effect of energy on the reactivity of chemical species underpins thermal reaction rate theory.

In 1986 Herschbach ³⁶, Polanyi ³⁷ and Lee ³⁸ were awarded the Nobel prize for their pioneering work in the field of reaction dynamics, emphasising the importance of this field to the understanding of chemical reactivity.

Techniques in the study of ion-molecule chemistry

Two recent books have been published on the modern techniques used in the study of gas phase ion chemistry ^{39,40}. The review articles presented in those books contain substantial experimental detail, including mathematical analyses of the relevant kinematics. A brief comparison of the advantages and disadvantages of the alternative methods is desirable here, in order to evaluate the crossed-beam experiment.

General

The choice of techniques used to study an ion-molecule reaction or process depend upon the information sought. Experiments may be carried out on many different levels, from ultimate specification of reactant and product conditions to thermally averaged measurements. Figure 1.2 illustrates the relationship between all the different experiments, what each determines and the mathematical operations required to link them. There is a good deal of overlap in the ranges of study available from each type of experiment, due to the design of versatile equipment. The growth in interest in tandem techniques has led to the fabrication of some novel apparatus ^{41,42}, coupling together various different equipment for the study of reaction sequences.

**STATE RESOLVED
DETAILED STUDIES**

**NOT DETAILED
STATE UNRESOLVED**

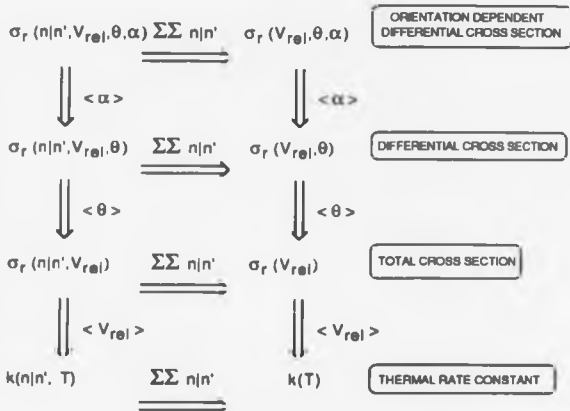


FIGURE 1.2: REPRESENTATION OF THE RELATIONSHIPS BETWEEN VARIOUS DIFFERENTIAL CROSS SECTIONS AND THE THERMAL RATE CONSTANT. ADAPTED FROM REFERENCE 40. NB. TRIANGULAR BRACKETS INDICATE AVERAGING OF THE ENCLOSED QUANTITY.

Swarm methods

The types of experiment can be divided into categories. Amongst these are the *Swarm* techniques ^{43,44} eg. *Flowing afterglow* (FA), *Selected ion flow drift tube* (SIFDT) etc. These are flow-tube experiments in which ions are typically formed in a discharge source and introduced to a carrier reagent gas flow. Historically products were detected by measuring a characteristic visible chemiluminescence, either directly or by the use of marker reactions which produce light. The most common method of detection is now mass selective achieved using *quadrupole mass analysis* and charge sensitive ion detecting apparatus. Selection of species of particular mass ions or products from reaction of a particular mass in drift tubes has been achieved with the use of radio-frequency electrodes. The analogy between the stop and go function of this type of mass filter has lead to the name *traffic light filters* ⁴⁵.

The reactants experience a large number of collisions throughout the reaction zone of a swarm apparatus, hence the energy content is averaged and can be defined by Maxwell-Boltzmann mathematics. The technique is, therefore, particularly attractive for the measurement of thermochemical and kinetic data. This advantage also limits the usefulness because no investigations can be made with non-thermal reactants. Electronic and some vibrational excitations are not efficiently quenched by multiple collisions. A study can be made of the effect of excess energy in an otherwise thermalised ion, when internal energy transfer depleting a particular vibrational mode or electronic state is slow.

An example of a chemical investigation using SIFT is the reaction ⁴⁶:

[6]



This reaction is studied at 300 K (0.02 eV) and provides the thermal energy limit to the low energy data obtained using a tandem mass spectrometer. In the SIFT study, the reactant ions are produced by electron impact ionisation of water vapour and mass selected for injection to the flow tube using a QMF. The observed reaction

channel, seen above, is interesting in view of the more exothermic channel producing solvated Br^- . This solvated leaving group ($\text{H}_2\text{O} \cdot \text{Br}^-$) constitutes less than 8% of the product yield in this channel, indicating that the precursor of the Br^- is not formed by CID of $\text{H}_2\text{O} \cdot \text{Br}^-$. This result indicates that the reaction coordinate does not efficiently couple the so called Walden inversion (or $\text{S}_{\text{N}}2$ mechanism) ⁴⁷ and the transfer of solvent molecule. Thus, it appears from the data that Br^- is formed directly, in contrast with the solution result in the presence of the bulk solvent ⁴⁸.

Mass spectrometric techniques.

The most common, non-analytical studies made with mass spectrometers are on the unimolecular decomposition of ions at kilovolt energies. The high energies used are necessary for transmission through the analysing sectors of the instrument. In the traditional *mass spectrometer* (MS) ion-molecule reactions can be performed in a high-pressure ion source. Equilibrium and thermodynamic measurements have been made in this way ⁴⁹.

In a standard electric and magnetic sector mass spectrometer, mass separation is made possible by a differential deflection the components of an ion beam according to energy and momentum respectively. Mass separation is achieved by passing an ion beam of narrow energy distribution through both an electric and a magnetic sector. High resolution can be obtained by selecting a narrow portion of the beam at strategic points along the flight path. The *quadrupole mass filter* (QMF) provides an alternative for mass selection, normally at low resolution. This latter type of analyser has a dynamic range of only a few electron volts. Many bond energies lie in the range 1-5 eV making techniques which access it very attractive. The QMF has become popular for ion trapping and collision-gas cell experiments; especially using the triple-quadrupole ~~tandem~~ mass spectrometer. MS-collision cell geometries allow the determination of total cross sections to reasonable accuracy, since the physical geometry of the cell is known ⁵¹. The principal drawback of the collision

cell geometry is the random thermal motion of the target gas. This effect limits the attainable resolution in the centre of mass quite severely.

Inaccuracies in measurements can be caused by scattering losses and the questionable integrity of the single collision regime. Cross section measurements can not be made unless the pressure in the collision cell is well characterized and the majority of ions undergo only one collision. Many collision-induced dissociation experiments are performed with gas admitted until the primary signal is attenuated by 50-60%. Under conditions where an attenuation of greater than a few percent observed, then multiple collisions are probable ⁵². In that case all dynamical information is lost. In the case of floated cells the question of the effect on molecular properties of the high potential and consequences for some measurements does not appear to have been addressed.

The investigations of aluminium cluster ions made by Jarrold and Bower illustrate the low-energy collision-cell technique and some of the properties of cluster ions. An example of their work is the collision induced dissociation (CID) of Al_nO_m $n>3$ -26 $m=1,2$ clusters ⁵³. In the experiment a laser ablates the surface of an aluminium rod. Small clusters aluminium with a bound oxygen are formed (Al_nO_m $n>3$ $m=1,2$). These clusters are ionised by fast-electron bombardment, then expanded in a He buffer gas in the hope of relaxing the varied internal energy content of the ions formed during the ionisation step. Ions are mass selected using a QMF and then dissociated in a collision cell using noble gas targets. The authors note that in the controlled conditions of the cell, multiple collisions are expected.

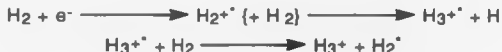
The relative abundance of the cluster and CID products are measured for selected ions. A strong dependence on cluster size of the effective total cross section supports the argument that stability varies with cluster size (magic numbers). The principal products of the dissociation are strongly bound molecules eg. the Al_2O neutral and the remaining ion $Al_{n-2}O_{m-1}$. In the initial cluster ion, the oxygen appears to be strongly bound (energies of 6-8 eV). This property is attributed to a rapid onset of metallic properties upon increasing the number of clustered atoms.

The change from molecular to metallic character appears to begin with relatively small clusters (Al_6^+).

An example of a fundamental reaction studied using a modified commercial mass spectrometer, is the collision induced dissociation and field ionisation studies of Bordas-Nagy and Holmes 54-56.

In one of these studies ⁵⁴ energy release measurements are made, using the technique of *mass-analysed kinetic-energy spectroscopy* (MIKES) on H_3^+ at 9.9 eV energy. The H_3^+ moiety is prepared predominantly in the ground state ion using a high pressure electron impact ionisation source by the sequence:

[7]



In the experiment the beam is attenuated (10%) in a collision cell and the energy released upon dissociation measured. The dissociation of H_3^+ using He and Ne target gases is interpreted as having two distinct channels. The first of these channels is a collisional excitation of the H_3^+ to the ^1A and ^1B states. The reactant states do not correlate directly with those of the products. A non-adiabatic transition between the reactants and ground state products occurs in the region of an avoided crossing in the potential surface. The most probable internuclear separation for a curve crossing is at an interatomic separation equal to the turning point of the ground state V=4 vibrational level. The difference between measured and calculated energy releases for the dissociation supports the claim that the V=4 level is most frequently populated. In the second channel, the formation of *high Rydberg* (HR) species changes the observations. The authors believe that the decomposition dynamics of the HR fragments is consistent with the three body dissociation reaction:

[8]



Total spin conservation is observed for collisions with He and Ne. The alternative target atoms Ar, Kr and Xe contrast by the different coupling scheme for the larger orbital angular momentum. This relaxes the selection rule conserving the total spin in favour of conservation of the total angular momentum.

Resonant methods and ion trapping

Experiments of this type utilise the different responses of ions to electric fields modulated at radio frequency. Formation and reaction of ions is performed in the same region, hence ions can have long residence times. These properties give the technique certain advantages. The ion trapping and long ion-residence time experiments are suited to ionisation techniques which have low signal generation and poor stability eg. *field desorption* (FD) ⁵⁷ or *resonance enhanced multi-photon ionisation* (REMPI) ⁵⁸. Using these tools photodissociation dynamics can be readily investigated. Alternatively long synthetic paths can be followed, in which the high sensitivity required is satisfied by forming, reacting and detecting ions non-destructively in the same physical space.

Ion cyclotron resonance (ICR) and related techniques ⁵⁹ have the advantage of enormous resolving power at low mass ⁶⁰. Ion-molecule reactions involving reactants of moderate or low mass, performed on these instruments take best advantage of the resolution. Accurate masses may be required in the analysis of experimental data. ICR can be applied to reactions with low yields caused by small reaction cross sections or an inefficient branching in the case of competition between channels.

ICR is disadvantaged by problems of near-resonant ion ejection. Similarly in quadrupole ion traps, trajectories of ions which lie just outside the stability region for transverse motions take many cycles of the applied RF field before ejection is induced. These techniques are not suited to the time-resolved study of very fast physical processes.

A study utilising two complementary ICR techniques has been made to investigate the energy disposal in non-resonant CT reactions of NH_3 with a variety of simple ions⁶¹. A variable voltage trapping cell ICR method was used to measure kinetic energy releases. The measurement of total rates of reaction and analysis of the internal energy content was made using a tandem ICR apparatus. The reaction of NH_3^{+} with H_2O was used to diagnose the internal-energy content of the NH_3^{+} ion. There are two product channels for this reaction: formation of H_3O^{+} and formation of NH_4^{+} . The reaction promoting NH_4^{+} is marginally exothermic and is seen exclusively at low internal-energy contents, whilst the reaction promoting H_3O^{+} is endothermic by 4.35 eV. By measuring the product branching ratios the authors were able to measure the average internal-energy content of NH_3^{+} up to a maximum of about 5 eV. Results indicate that the precursor CT reagent ions deposit between 1 and 4.9 eV of energy into NH_3^{+} . The observation that this transfer is less efficient for increasingly large precursor ions is a reflection of the greater number of modes to partition the energy released.

State selected chemistry and laser applications

The most detailed information on state resolved chemical reactions can be derived from laser experiments. The laser has contributed substantially to the study and the understanding of state-to-state reaction dynamics. There are two principal techniques used to investigate state-selected chemistry: they are laser based and coincident detection experiments.

Laser-based experiments normally involve more than one laser. Reactants are formed from the gas phase precursors by picking out transitions to select the rovibrational state required. A subsequent laser is typically used as a detector by the powerful method of *laser induced fluorescence* (LIF), first applied to reaction dynamics by Zare and co-workers⁶². The biggest advantage of the use of lasers is in the excitation of forbidden transitions. These transitions use *virtual states* to provide a stepping stone to higher states by the coherent absorption of photons of a particular

wavelength. Problems can result from power broadening of states and relaxation of selection rules. These effects have been used to advantage in the *dressing* of reactant states to produce novel reactions ⁶³.

The coincidence techniques work by detecting an ion gated with the collection of the electron expelled by threshold ionisation. An example ion-molecule experiment of this type is the *threshold electron secondary ion coincidence* (TESICO) developed by Koyano and Tanaka ⁶⁴. In the TESICO experiment a precursor photoion is used to synthesise secondary ions of interest in addition to providing the threshold electron to start the reaction clock. The disadvantage of the experiment is the ~~the~~ scattering loss of products in 'close' collisions.

The reactions of CH_5^+ are of considerable interest and have been widely studied, because of the use of this reagent as in the *chemical ionisation* (CI) technique. A systematic study of the reactions:

[9]



which form this reagent in the source are of interest. A study of this reaction has been made in a collaborative study between groups using the complementary techniques of TESICO and of crossed beams ^{64,65}.

The crossed-beam study, between 0.6 and 3 eV, showed that three mechanisms were in simultaneous operation. Two of these reactions were interpreted as H⁺ and H transfer reactions at the CM angles of 180° and 0° respectively. There was also a small quantity of the CH_5^+ formed from a C_2H_8^+ intermediate complex whose lifetime was greater than about 10^{-12} s over the energy range 0.6-2.5 eV. Although the mechanisms were distinct in this crossed beam study, the internal energy dependence of the branching ratios could not be investigated. The average energy content in this study of the combined internal modes was 1.0 eV and this was spread over the estimated range of energies: 0.2-1.3 eV.

In contrast, the dependence of these reactions upon internal energy could be analysed by TESICO to the resolution allowed by the overlapping states of the CH_4^+ ion. The magnitude of the internal energy content was defined precisely for five values in the range 0.13-1.07 eV. Information upon the actual modes populated was not available due to the intractable threshold photoelectron spectrum. These reactions showed additional information about the total cross section. Surprisingly, it diminished with an increase in both internal and translational energy. The branching ratios of the isotopomer reactions, including the charge-transfer channel, were measured and used to distinguish between the different mechanisms seen in the crossed-beam reaction. The results indicate that the CT reaction channel is never more than 50% of the total ion yield. Furthermore, the proportion of product giving rise to the dominant H^+ transfer channel goes up with internal energy and, to a lesser extent, with kinetic energy at the expense of the other reactive channels.

Some of the work on orientation effects has been done with lasers. One of the most interesting experiments that has been performed is the femtosecond time resolved photodissociation dynamics⁶⁸⁻⁷⁰. *Snapshot* data can be transformed into information on the repulsive potential surface on which the projectiles move.

A most elegant example of the femtosecond time resolved photodissociation dynamics, made by Zewail and co-workers, is the hot-atom reaction⁶⁸:

[10]



proceeding via a bent HOCO transition state.

In this study a supersonic expansion of HI and CO_2 is made under conditions promoting the formation of a 1:1 mixed bimolecular cluster. This cluster is a van der Waals linear molecule bound by a single $\text{H}\cdots\text{O}$ hydrogen bond. A picosecond laser pulse starts the reaction clock and dissociates the HI bond. A second laser (probe) maps the progress of the developing reaction recording snapshots in time with a resolution of a few femtoseconds. A number of advantages are gained by the cunning

use of the aligned clustered precursor. The H atom is released with a velocity of 20 km s^{-1} (2.07 eV) directed initially along the OCO bond. This energy release gives the collision energy in the CM framework directly. The impact parameter for collision has a reduced range of values because the precursor molecule is a locked rotor. The signal to noise ratio is greatly enhanced by clustering the precursor and by limiting the potential surface to a single orientation.

Beam experiments

Beam techniques to be discussed here are the *guided ion-beam*, *merged beam* and the *crossed-beam* experiments. These experiments have been kept separate from the section on mass spectrometry, because the reactions are always performed outside the source area.

The guided ion-beam experiment ^{13,33,52,71} involves the production of a mass selected, low energy ion beam which is injected into an ion guide. The ion guide consists of long multipole rod system to which a modulated inhomogeneous electric field is applied. Ions confined to motion within the guide are steered though a gas cell, where reaction products are formed. Products are trapped within the ion guide and are transported to the detector for mass analysis. The technique is suited to absolute determinations of total reaction cross sections, because products are collected from all 4π steradians of solid angle. The presence of the strong inhomogeneous electric field at the point of ion formation provides the advantage and limitation that nascent internal excitation is efficiently relaxed.

A recent paper by Boo and Armentrout ³³ illustrates the guided ion beam technique. The energetics and reaction mechanisms of $\text{SiH}^+ + \text{D}_2$ and $\text{SiD}^+ + \text{H}_2$ are presented together with a study of the collision induced dissociation of SiD_3^+ . The reaction $\text{SiH}^+ + \text{D}_2$ proceeds to form three distinct products: SiHD^+ , Si^+ , and SiD_2^+ . The absolute cross sections for these reactions are measured and the threshold energies for each of the channels are compared to literature values. Results indicate a lack of barriers in excess of the endothermicities of these channels, but the

measured cross sections are smaller than the Langevin cross section by half an order of magnitude. The difference is attributed to the difference in zero point energies not accounted for in the model.

For the reaction $\text{SiH}^+ + \text{D}_2$ (and $\text{SiD}^+ + \text{H}_2$), the reaction mechanism is interpreted as consistent with the formation of a transient SiHD_2^+ (SiH_2D^+) intermediate: 1.6 eV more stable than the reactants. The transient is supposed to dissociate according to a thermodynamic control consistent with statistical population of the different exit channels in the reaction coordinate. By that argument the transient must be long-lived on the scale of intramolecular energy transfer i.e. more than several rotational periods. Direct evidence for the intermediate is not available. This reaction has not been studied by the crossed-beam technique which might verify the mechanism ⁷².

The merged-beam experiment ^{13,52,71,73-76} is rather different in nature. It begins by the formation of two ion beams. The first of these is the neutral beam precursor, which is formed as an ion beam for the purpose of acceleration and manipulation. The beam is neutralised by resonant charge transfer before being passed into a merging magnet. The merging magnet is used to direct the second reactant ⁷⁷ beam on to the direction of the neutral beam. The magnet also induces rejection of any residual charged particles left in the neutral beam. The experiment has the largest range of initial relative collision energies. The initial relative velocity can be varied easily from zero to several kilovolts if desired. The most interesting prospects are in the study of subthermal collisions in ion-molecule reactions. The use of resonant charge transfer of the neutral beam can be used to provide internal excitation of the reactant. In fact it is unlikely that vibrationally relaxed beams can be produced after successive ionisation and neutralisation of the neutral reactant beam. The electronic transitions are governed by Franck-Condon factors and a large number of vibrations would be expected to be significantly populated.

A systematic study of the reaction of D_2^+ with X (X = C, N, O, F) has been made by Gentry and co-workers using the merged-beams technique ⁷³⁻⁷⁶. Two of these reactions are interesting to contrast ⁷³⁻⁷⁴. In each reaction the study has been made over the energy range from 0.002 eV to almost 30 eV. The total reaction cross sections are measured as a function of energy and decline rapidly as the energy is increased.

The reaction:

[11]



is adiabatic and direct at all energies. An inflection at 25 eV is observed in the declining total cross section as a function of energy. This inflection is interpreted as evidence of a second adiabatic channel which correlates the reactants to an endoergic channel involving the excited products $DF^+(^2\Sigma) + D(^2S)$.

In contrast the detailed dynamics of the X = O reaction are different. The $O(^3P)$ has an electrostatic quadrupolar moment dominating the dynamics. The approaching ion locks into the O atom according to the spatial orientation of the electronic angular momentum. This locking of the reactants reduces the ranges of symmetric combinations available and the efficiency of the reaction. There are six separate potential energy surfaces for the different (L_J) couplings in the long range part of the potential. In the closer approach these six surfaces correlate smoothly with just three symmetries. For the surface of A symmetry 87% of collisions lead to reaction and 53% for the B.

The crossed-beam experiment is considered in more detail in the next section.

The crossed beam experiment

In a crossed ion-neutral beam experiment relative differential cross-sections are measured as a function of energy at a known initial angle of incidence (normally 90°) and of scattering angle, all defined in the *laboratory frame of reference*. The differential cross section, $i_{LAB}(V, \Theta, \Phi)$, is the quantity of product flux scattered to within a small section of solid angle, defined by Θ, Φ , per unit time.

A considerable angular momentum results from the combination of large impact parameters and the initial relative velocities of the reactants. To a first approximation the product is confined to the plane containing the initial velocity vectors. Perturbations to this approximation exist and are many fold: for example, spread in the initial beam conditions, the 3D nature of the cross section of the target, molecular angular momenta (rotation, orbital...) etc. Nevertheless Φ will always be small, because of the magnitude of the torque of the initial velocity vectors and the differential cross section, $i_{LAB}(V, \Theta)$, is effectively just dependent on Θ . In addition the effect of the different perturbations is minimised by the detector resolution in the Φ plane.

In order to present the data in a tractable form the transformation of the data can be made into several different spaces. The most simple transformation for the data is into laboratory polar space, because the data is measured in this coordinate system. The other transformations are to CM polar and to ^C Gaussian coordinates. The reduced Jacobian transforms ^J 77.78 for each of these data are displayed below.

[12]

$$i_{LAB}(E)dE = i_{LAB}(V)dV$$

[13]

$$I_{\text{CART}} = \frac{1}{V^2} I_{\text{LAB}}(V, \Theta, \Phi)$$

[14]

$$I_{\text{CM}}(U, \theta, \phi) = \frac{U^2}{V^2} I_{\text{LAB}}(V, \Theta, \Phi)$$

I = Product flux, E = Energy, V = LAB frame velocity, U = CM frame velocity,

Θ = LAB frame meridional polar angle, Φ = LAB frame azimuthal polar angle,

CM = centre of mass, LAB = Polar laboratory frame, CART = Cartesian frame

ϕ = CM azimuthal angle, θ = CM meridional polar angle.

A full discussion of the derivation of the Cartesian Jacobian has been made by Ryan ⁷⁶. Alternatively, a rigorous presentation of vector space arithmetic for data reduction from any initial angle of incidence has been published by Herman and Friedrich ⁸⁰.

The Cartesian form has become standard because the volume elements have constant size and the representation is not changed by the choice of origin. The data can be presented in the form of a *Newton diagram*, which enables both the laboratory and CM representations to be reconciled on a single plot. The other representations each introduce a distortion of the data caused by their respective dependences on a reciprocal velocity term (see Herman and Birkinshaw) ⁷⁷.

Figure 1.3 shows two Newton diagrams. The first of these illustrates the connection between the initial and relative vectors in laboratory and CM velocity space. The second diagram in the figure shows the contribution to the differential cross section of various product velocity vectors and the detector resolution.

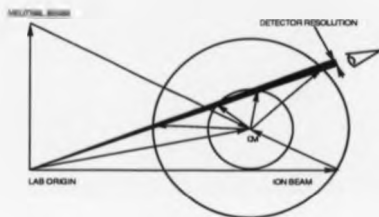
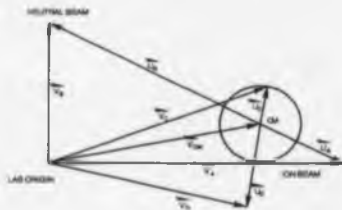


FIGURE 1.3: NEWTON DIAGRAMS TO ILLUSTRATE SOME OF THE EXPERIMENTAL CONDITIONS IN VECTOR SPACE.

Key equations of reactive scattering

Products with a given amount of kinetic energy are collected at a scattering angle measured in the laboratory. This data is then transformed into the *Cartesian centre of mass* (CM). In the CM frame, the observer appears to have travelled along the vector describing an elastic *sticky collision*. Under this mathematical transformation the motion of the centre of mass through space is removed. Only the relative motions of the reactants and products remain, and the dynamics are considerably simplified.

Referring to the vectors labelled in figure 1.3, two vector equations for the magnitudes of the relative velocities (V_{REL} , V_{REL}) can be written:

[15]

$$\vec{V}_{REL} = \vec{V}_C - \vec{V}_D$$

[16]

$$\vec{V}_{REL} = \vec{V}_A - \vec{V}_B$$

Applying the conservation of linear momentum in the CM framework one obtains the equation:

[17]

$$M_A U_A + M_B U_B = M_C U_C + M_D U_D = 0$$

M = Mass, U = CM velocity.

for each pair of reactants or products. Each laboratory velocity can be expressed by a sum of two vectors. The first of these for any moiety is the CM vector. The second is constructed from the relevant relative velocity vector for reactants or products. The equation is of the form:

[18]

$$U_B = \frac{M_A}{M_A + M_B} \vec{V}_{REL}$$

The relative kinetic energy (E_T) of the collision can be shown from this to be

[19]

$$E_T = \frac{M_A \cdot M_B}{2(M_A + M_B)} \left| \vec{V}_{REL} \right|^2 = \frac{\mu}{2} \left| \vec{V}_{REL} \right|^2$$

μ = reduced mass.

The energetics of the reaction are subject to the principle of the conservation of total energy. The sum of the total energy contained in the products and in the reactants, including the difference in zero point energies, is constant. This can be stated mathematically as:

[20]

$$E_T' + I_E' + \Delta H_r = E_T + I_E = E_{TOTAL}$$

I_E = Internal energy, E_T = Relative kinetic energy, ΔH_r = Enthalpy change of the reaction (prime indicates products).

From this equation it is possible to construct a series of circular zones around the CM origin. The locus of each circle depicts the threshold for formation or stability limit of a product in a specific state:

[21]

$$Q_{max} = E_{Total} - E_{Threshold}(P^+)$$

[22]

$$Q_{min} = E_{Total} - E_{Threshold}(P^+) - E_{Dissociation}(P^+)$$

Q = Exoergicity, E = Energy, P^+ = Ion state considered.

Product ion flux may be correlated to products with a particular level of excitation, or in a given state, if it appears between the circles describing the formation and stability limits of a particular quantum state. The limit imposed on the resolution of these states in a kinetic energy measurement is in the overlap between rotational or vibrational progressions or channels of reaction.

The angular distributions of the products in the CM ^Cartesian space are recoverable from the double differential cross section (that is differentiated with respect to U and θ)

[23]

$$I_{CM}(\theta) \propto U^2 \int_0^\infty I_{CART}(U, \theta) dU$$

and the relative translational energy of the products from the relation:

[24]

$$P(E_T) = U_C \cdot 2\pi \frac{M_C + M_D}{M_C \cdot M_D} \int_0^\pi I_{CART}(U_C, \theta) \sin(\theta) d\theta$$

The distributions of product ion flux can be drawn as contour or as axonometric plots. These plots are 3D pictorial representations of the differential cross sections. The form of the plot depends on the detailed reaction mechanism operating and the time window accessed. This time window is not variable, nor is it well defined. A molecule or ion has many of its own internal clocks which span different time scales: the time taken to excite an electronic transition ($\sim 10^{-16}$ s); the period of vibration ($\sim 10^{-13}$ s); the time lapse between absorption of energy to spontaneous phosphorescence ($\sim 10^{-3}$ s) etc..

The periods of vibration ($\sim 10^{-13}$ s) and of rotation ($\sim 10^{-12}$ s) are of interest here. No chemical change, with the exception of electron transfer, can occur in a time shorter than about 50% of a vibrational period, because this is the actual time taken to move atoms. Naturally there is some variation in vibrational periods depending on the reduced mass and energy content of the vibrator, but the range of values is within an order of magnitude. If the time scale for the interaction of the particles exceeds the rotational period the dynamics changes and the pictorial representation of the differential cross section changes in a characteristic manner.

The separating products retain a *sense of the direction* of the initial CM velocity vector of their precursors, providing that the minimum lifetime of the intermediate is greater than one rotational period. Under these conditions the product is distributed isotropically into a mathematical space, $I(\theta)\sin(\theta)d\theta d\phi$. The mathematical space is itself polarised, due to the factor of $\sin\theta$. This factor normally leading to a build up of intensity at the poles, because for the equation above to be constant $I(\theta)$ must be proportional to $\sin^{-1}\theta$. Figure 1.4.

In the complex case, the appearance of the product distribution map depends on the symmetry of the dissociating intermediate. This distribution is without exception symmetric to reflection in the plane intersecting the relative velocity vector perpendicular to the centre of mass: see figure 1.5.

The classification of crossed beam reactions is made according to the description of the mechanism. In the case of an asymmetric distribution of products with respect to reflection in the plane defined above, the reaction is said to be direct and proceeds without the formation of an intermediate complex. The reaction products are said to be long lived if they arise from a mechanism involving a intermediate complex. That means the products form via a metastable transient or *well* in the potential energy surface with a lifetime exceeding several rotational periods. There are intermediate cases between these extremes, the term *oculating complex* was coined by Herschbach⁸² to describe the interaction lasting close to one rotational period. The interpretation of results must be made with extreme care, because direct interactions can lead both to forward and to backward scattering. A change between one direct mechanism and another could be mistaken for evidence of a complex mechanism.

The strength of the crossed beam experiment is in elucidation of these very fast mechanisms. The measurements made on a crossed beam apparatus can have a high error caused by unknown systematic effects and great care must be taken to obtain reproducibility. The most obvious problem with the experiment is the unknown dimensions of the beam intersection (*crossing region*). All processes

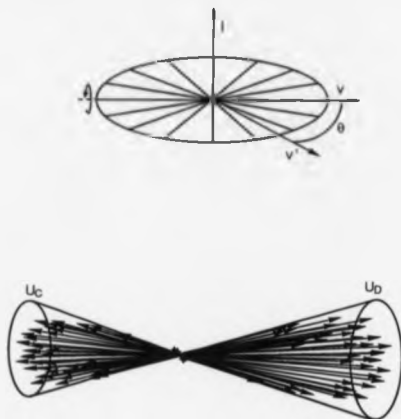


FIGURE 1.4: DIAGRAMS TO ILLUSTRATE HOW ISOTROPIC DISTRIBUTION OF PRODUCT ION FLUX INTO $I(\theta)\sin(\theta)d\theta$ LEADS TO A BUILD UP OF POLAR INTENSITY.

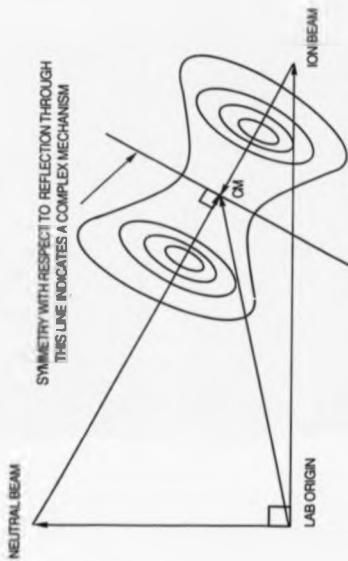


FIGURE 1.5: DIAGRAM TO SHOW THE SIGNIFICANCE OF SYMMETRY IN THE NEWTON DIAGRAM.

leading to scattering loss or attenuation of a reactant A, are linked to the Lambert-Beer law. Under single collision conditions this equation takes the form:

[25]

$$\frac{I}{I_0} = \exp(-\sigma n_B l)$$

For the absolute determination of the cross section of any process the path length (l) must be known as well as the total, soft-sphere cross section (σ) and the number density per unit volume (n_B) of the target. Unfortunately, l can only be estimated and hence only relative measurements of differential cross sections can be made. These measurements will be self-consistent for constant beam conditions.

Requirements of the crossed beam experiment

The successful performance of a crossed beam experiment depends on the satisfaction of some basic conditions. Each beam must be stable and reproducible, intense, collimated and near monoenergetic. The ranges of acceptable conditions are tabulated below:

Table 1.1: Conditions required for a crossed beam experiment.

CONDITION	NEUTRAL BEAM	ION BEAM
Angular divergence [#]	$1\text{--}4^\circ$ FWHM	$1\text{--}4^\circ$ FWHM
Beam flux [#]	10^{17} molecules s^{-1}	0.1-1 nA
Energy spread [*]	15-293 K	0.2-0.5 eV
Stability [#]	> 1 week	> 1 day
Reproducibility [#]	10%	10%

[#]denotes a minimum condition and ^{*} denotes a maximum.

NB. The extrema of these conditions can not be defined with absolute quantitative values. Some are formed from a further set of constraints unique to each apparatus and all are coupled together by their conflicting effects on intensity and resolution. The final choice of acceptable conditions is a balancing of local requirements, such as the size of the crossing volume in the light of detector acceptance (typically 2°), magnitude of the cross section or initial ion energy.

The background pressure must be kept low to ensure that the free path of the secondary ions is at least comparable to the dimensions of the vacuum chamber.

Using Kennard's value ⁸³ for the mean free path for a vacuum chamber of 1 m diameter the background should be of higher vacuum than 5×10^{-5} mbar ⁸⁴. Similarly, the ions traversing the target beam should have a significant probability of only experiencing a single collision. Routine maintenance to the vacuum system and the working parts is essential to good performance.

Crossed ion-neutral beam instruments

The first crossed ion-neutral molecular beam instrument was built by Turner *et al* in 1965 ⁸⁵. This instrument was designed for the measurement of differential cross sections and angular distributions. Since then over seven instruments ⁸⁶⁻⁹³ have been built for the study of angular and energy distributions from crossed ion-molecule reactions, in addition to the single-beam gas-cell instruments.

An apparatus for the study of total electron-transfer cross sections has been built by Ng *et al* ⁹⁴. The instrument uses two pulsed supersonic beam sources. The first source is the ion-beam precursor, state-selected ions are generated by pulsed laser photoionisation. Ions are extracted and focussed into a beam using traditional electrostatic ion optics. The angle-scanning detector has been removed from the design and replaced by a pair of quadrupole mass analysers, each in line with one primary reactant beam. The beam intersection is also reasonably well defined thus improving the accuracy of the measurements.

All the other crossed beam instruments, except the one stationed at the University of Warwick, have conventional sector ion optics for the production of the ion beam. There is some variation in the ionisation techniques used to produce the ions. *High pressure collisional stabilisation*, *electron impact* (EI), *resonant charge transfer* (CT) and *photoionisation* techniques have all been applied. The choice of neutral beam is either an effusive (eg. capillary array) or a supersonic beam.

By far the widest variety of innovative design in crossed beam instruments is in the detection system. An experiment requiring the measurement of product distributions as a function of scattering angle must have moving parts. An angle scanning detector and analyser is normally more simple to make. Moving parts should be light, hence a common choice of mass analyser is the QMF in the detector. Sectors and even *time of flight* (TOF) ⁹⁰ have also been used as detectors. Normally the detector is moved, however, there is a precedent for instruments with rotatable sources and a fixed detector ^{86,92}.

Chemical dynamics using crossed beams

The reactions investigated in early studies using crossed beams include examples of both the persistent complex mechanism and direct interactions. Products have been observed scattered forwards and also backwards with respect to the ion beam initial (CM) velocity vector (\hat{u}) and symmetrically around the CM. These are predominantly studies of proton transfer reactions and were made before about 1980. All these examples have been extensively and repeatedly reviewed in the literature ^{52,71,77,82,84-89}. For the purpose of illustrating statements on reactivity etc. made in this chapter a selection of recent, relevant and landmark papers is reviewed below.

(No + H₂)⁺ benchmark reactions of group 18

The reactions $H_2^+ + No$ where No = Xe, Kr, Ar, Ne, He are interesting. For No = Ne, He reaction is observed to produce exclusively the catalytic dissociation of H_2^+ . Reaction on the other charge exchanged manifold, however, produces NoH^+ . For No = Kr, Ar and Xe the NoH^+ ion can be formed from both surfaces. Mahan ²² analysed the strict symmetry restrictions on the reactions of noble gases with hydrogen. The different dynamics for the lighter noble gases in the reactions $No^+ + H_2$ and $No + H_2^+$ can be explained in terms of the orbital correlations of states.

Whilst all the $(\text{No}, \text{H}_2)^+$ reactions have been studied 92,100-109 the most widely known is the bench-mark reaction of $\text{No}-\text{Ar}$. These reactions are direct and lead to forward peaking with respect to the oncoming ion. The dynamics suggest large impact parameter reactions where a hydrogen atom is stripped from the target neutral with almost no momentum transfer to the remaining atom. This phenomenon has been approximated by a model called the spectator stripping mechanism which models the reaction dynamics and product energy disposal at intermediate energies.

In the high and low energy regime very significant deviations have been observed between the measured dynamics of $\text{Ar}^+ + \text{H}_2$ and the predictions of the SS model. These shortfalls even in the most simple of reactions, uncover the gross simplification of the model. The model represents an extreme limiting case of reactivity and is a good first approximation to use when analysing CM data. In the attempt to describe the actual high- and low-energy behaviour of reactions the model has been revised in several ways. Polarisation stripping includes a consideration of the acceleration and retardation induced by the attractive part of the long range interactions of the different ion-molecule pairs. The addition of a polarisation term modifies the low-energy behaviour and explains the increased forward peaking at low energies. The addition of the elastic scattering of the spectator satisfies the angular dependence of the differential cross section, whilst retaining good agreement with energy disposal for stripping reactions. The model can then be applied to rebound reactions 110.

Later studies performed with vibrationally excited H_2^+ scattered from He and Ne produces efficient reaction for v_23 111. The reaction has subsequently been used by Farrar in source reactions to quench H_2^+ excitation in order to crudely assess the role of vibration in $(\text{H}_2^+ + \text{Ar})$ reactions 101.

Jarrod *et al* studied three reactions of CO^+ . The first of these was:

[26]



$\Delta H = -0.58 \text{ eV}$; $1.81 \text{ eV} \leq \text{Energy range of study} \leq 10.12 \text{ eV}$

Several ionic species were detected: C^+ was of low intensity at all energies, O^+ intensity was thought to correlate with CO_2^+ dissociation and a broad band of O_2^+ was assigned to CT. No further studies were made on these species.

CO_2^+ was found to react by a direct mechanism at all energies and a barrier was discovered in the reaction coordinate leading to a peak at 5 eV in the kinetic energy dependence of the cross section. In the reaction there was a preponderance for forward scattering ~~although~~ backwards scattering: an increase in forward recoil takes the product outside the elastic circle at the highest energy studied. The efficiency of backwards scattering peak was assigned to a competing ideal knockout channel in a collinear reactant approach, and was observed to increase with energy. This could also be explained by an increased collection efficiency in the presence of discrimination effects in the detector.

There are three problems explained in the text. These are 1: discrimination against slow ions in the RPD analyser. 2: Further discrimination against slow product collected at large laboratory scattering angles. 3: the lack of detectable modulation of background pressure when chopping the neutral beam.

It is unfortunate in this study that the charge transfer cross section was not measured to normalise the differential cross sections of other process against literature results ^{11B}. This would have proven the authors claim that the appearance of the barrier in the reaction was due to an avoided crossing into the charge transfer surface, because the net effect would be to change the branching ratios sharply decreasing the quantity of O_2^+ formed by CT. A further study to include isotopic

resolution ^{18}O is suggested by the authors to enable the two different possible positions of attachment of the O- stripped to be assessed. Changing the source for a Cl source should improve the relaxation of nascent CO^+ vibronic excitation and remove the possibility that the reaction is driven by high cross section reaction of the higher vibrational CO^+ .

The reaction to form CO_2^+ is not observed in SIFT studies. This is perhaps not surprising considering kinetic energy dependence of the cross sections. The limit to the range of energies studied is about 5 eV for SIFT^{-DART}, this is just at the peak of the reaction cross section for CO_2^+ production. It is interesting that the reaction was not detected ^{above} ~~below~~ threshold since in the study made by Jarrold *et al*, the increase in the cross section is only 10 fold. The SIFT technique has substantially greater sensitivity than that of the crossed beam.

Also studied were the analogue reactions of CO^+ with NO. The reaction findings are summarised below.

[27]



$$\Delta H = +2.70 \text{ eV}$$

3.5 eV \leq Range of study \leq 10 eV

[28]



$\Delta H = +0.81 \text{ eV}$, lower process is a spin forbidden predissociation.

2.5 eV \leq Range of study \leq 13 eV

A CT product is expected in these reactions, however, other products to those noted above, were not reported. The significance of the CT channel is the same as discussed above.

The reaction to form $(\text{NCO})^+$ is complicated by the existence of three stable isomers. Formation of the highest energy isomer requires a concerted insertion into CO bond during reaction which is unlikely in view of the direct nature of the reaction for all energies. The NCO^+ appearance energy is not measured directly, but by extrapolation agrees well with the calculated appearance of NCO^+ . The calculated threshold of the next highest energy ion is plausibly close within the energy range over which the reaction was studied, taking into account the combined error of the experiment and calculation.

As was observed for the reaction with O_2 , a maximum is observed in a plot of ~~relative cross section versus kinetic energy (eV vs k.e.)~~ ^{relative cross section versus kinetic energy (eV vs k.e.)}. The barrier was assigned as before to ~~kinetic energy versus relative cross section~~ ^{maximum on the eV vs k.e. plot} an avoided crossing in the reaction coordinate. For NCO^+ this ~~barrier~~ ^{maximum} consisted of a broad maximum peaking about 8 eV and for CO_2 a sharper peak at 6 eV. No explanation is offered by the authors for the broadening of the peak. We note that the ion begins to dissociate before the calculated limit. The nature of the broadening may arise, therefore, from the contribution of a second NCO^+ isomer.

The authors speculate on the relative branching into the different channels of reaction. Qualitatively they attribute the closer collisions to the formation of NCO^+ , whilst grazing trajectories lead to CO_2^+ . At low energies NCO^+ gave rise to backwards scattering in contrast to the forward nature of the CO_2^+ peak. The authors note that the spectator stripping model does not explain their observations. This demonstrates the need for more accurate theories, such as can only be made after accurate ab initio potential energy surfaces have been calculated on which Monte-Carlo trajectory studies can be made.

The conclusions drawn in these papers are reasonable, but leave a lot of scope for confirmation. The authors have shown that the neglected area of four-centre reactions of substantial molecules is interesting and worthy of further study.

Reactions on surfaces with a double potential minimum well

Much of the recent work from the Farrar group, Rochester USA, has been concerned with a model of ion-molecule reactions proposed by Brauman ¹¹⁶. In the model, reaction is hypothesised to occur on a potential surface with two minimum potential wells. The wide variety of reaction rates is then rationalised on the basis of a reaction coordinate which samples both of these wells and of the barrier height separating them. The results of Brauman have been consistent with the model, but the crossed-beam technique is uniquely able to provide unambiguous confirmation of this mechanism if it occurs.

~~An example of a reaction which it is suggested~~

~~One such for which it is suggested that the reaction occurs on surface with a~~
double minimum, is the reaction of the ammonia ion with isotopic variants of hydrogen ¹¹⁷. This reaction has two competing channels going to different reaction products:

[29]



[30]



An early crossed beam study of $\text{NH}_3^+(\text{H}_2, \text{H})\text{NH}_4^+$ over the translational energy range $1.2 \text{ eV} \leq E_T \leq 4.6 \text{ eV}$ by Elsele *et al* ¹¹⁸ had not confirmed the low energy mechanism of reaction. At the higher energy the reaction was clearly direct. More recent studies of this reaction with vibrationally excited reactants using different techniques had been rationalised in opposing ways.

Farrar *et al* were able to produce high-quality reactant beams of initial relative kinetic energy of only 0.5 eV, substantially lower than the limit of Elsele's work. The study contains a number of interesting features.

Reactants were prepared with average vibrational energies of 3.3, 4.0 and 4.9 eV by resonant charge transfer. The rate of reaction was enhanced for an increase

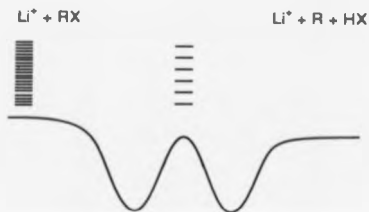
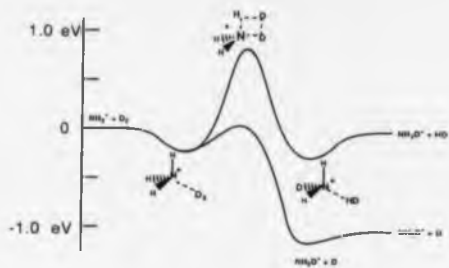


FIGURE 1.6: THE REACTION CO-ORDINATES FOR THE REACTIONS OF NH_3^+ WITH D_2 AND Li^+ WITH RX (ALKYL HALIDES)

in vibrational energy in both channels. The larger of the cross sections for the competing channels is that of $\text{NH}_3^+(\text{D}_2, \text{D})\text{NH}_3\text{D}^+$. The latter reaction showed symmetric peaking along the initial relative velocity vector. The authors regarded this as being consistent with a prolate symmetric top molecule dissociating along its reaction coordinate. The mechanism was assigned to an *osculating complex* mechanism, because the forward peak increases in intensity as the energy content of the intermediate molecule becomes higher, decreasing the lifetime of the ion. In contrast, the alternative channel is direct at all energies. Each of these reaction channels has a shallow pair of minima. The implication is that the second well is not sampled by the hydrogen atom exchange reaction. The schematic reaction coordinates are shown in figure 1.6.

A further series of reactions 119-122 has been studied where the analysis has not been so simple. Farrar has found the scientific community much more hostile to his views 123 on interpretation of the lithium ion catalysed elimination reactions of aliphatic halides and alcohols as proceeding via Brauman's model. In these cases the reaction coordinate has some different features to those of the $\text{NH}_3^+ + \text{D}_2$ system.

Kinetic spectroscopy in charge transfer reactions

Some important work has been produced by large group of Jean Futrell at Utah and subsequently at Delaware 124-132. This group has made a systematic study of the CT reactions of small molecules and found interesting differences between these and the chemistry of atoms and atomic ions. Following improvements in the quality of resolution obtainable on their instrument this group has also measured detailed cross sections for reaction.

Many charge or electron transfer reactions have been studied for atomic ion - atom systems. The role of resonant charge transfer is known and unsurprising for symmetric systems such as $\text{He}^+(\text{He}, \text{He})\text{He}^+ \Delta H = 0$. For the cases of long range interaction between the ion and the neutral weak coupling of the particle momenta results in the observation of near rectilinear trajectories. In the high-energy range

small deflection angles in the centre of mass is commonly observed. The energetics of the reactions of atomic ions with atoms considerably simplifies the dynamics due, in part, to the absence of vibrational modes of the separated reactants and products. Some complication is caused by the disposal of angular momentum in these reactions. This effect dominates the close-coupling interactions in this regime. The coupled spin and orbital angular momenta are split into two states that are separated by only a few tenths of an electron volt. These states are sufficiently low lying to be populated, and are sufficiently well separated to be resolved in a translational spectrum (accessible to a crossed beam study).

Recent publications from the Futrell group have demonstrated elastic, superelastic and subelastic charge transfer. The superelastic and subelastic processes arise from electron-ion recombination. Below a threshold impact parameter at sufficiently low energy, formation of a long-lived orbiting ion induced dipole complex is observed. At the higher energies low impact parameter collisions are observed. These observations are consistent with the prediction that the *Langevin* cross section for a process increases as the energy decreases. Both inelastic and elastic scattering channels were observed. The resonant symmetric charge transfer is elastic with near rectilinear trajectories. The second, non-reactive channel, demonstrates energy redistribution with an endoergic transition excited involving a change of $\Delta J=1$.

For the reaction of $\text{Ar}^+ ({}^2P_{3/2}, {}^2P_{1/2}) + \text{Ar}$ there is some evidence of superelastic scattering from the $\Delta J=1$ transition for which the energy release of $\Delta H=0.18$ eV is converted into translational energy.

This group has also presented a series of more adventurous two-body reactions involving more than two atoms. Here, the inclusion of the rotational and vibrational contents of the molecular ion and neutral molecule complicate the dynamics. New dynamics were observed for which theoretical studies are required. The resonant CT and presence of the low energy complex in $\text{N}_2^+ (\text{N}_2, \text{N}_2) \text{N}_2^+$ giving rise to a symmetric distribution are both observed at energies below 1.5 eV, with the

contribution from the complex diminishing as the energy rises above its dissociation threshold. The most surprising feature of the reaction dynamics is a phenomenological energy window in which population of all the allowed vibrational bands of the N_2^+ ground state are formed. The scattering is clearly separated in the kinetic energy part of the plot of the differential cross section. The $v=3$ level gives rise to backward scattering (with respect to the direction of the incoming ion) at the energy of 1.4 eV.

The reaction of Ar^+ with N_2 is quite interesting. Futrell and co-workers¹²⁹ developed the ability to vary the state population in the beam up to (essentially) pure $2P_{3/2}$. This was used effectively to allow linear deconvolution of CM data. The contributions to the total observed dynamics are quite different for the two states. The reaction was found suitable to make a formal study on the chemistry of the source, where ~~with~~ ^{was} the reaction ~~used~~ ^{was} to monitor the content of the effluent beam.

Reactions of doubly charged ions

Few crossed beam studies have been made on doubly charged ions to date. Herman and co-workers¹³³⁻¹³⁵ have studied the single electron transfer (SET) reactions of atomic double ions. In the studies that have already been made on these systems, large cross sections for SET are observed for reactions on potential surfaces where the cross over of the two CT surfaces is in the 2-6 Å range of reactant separation. Other features of the data are very similar to those of the charge transfer reactions in the section *Kinetic spectroscopy in charge transfer reactions* i.e. state separation is resolved in the double differential cross section $\sigma(U, \theta)$

Interest in the reactions of doubly charged ions is likely to grow. The full potential of the area will not be realised until scattering studies on molecular ~~double~~ ^{dication} ~~ions~~ have been performed. Ions such as CS_2^{2+} are easy to make and appear in 30 eV electron impact ionisation spectra of the CS_2 neutral molecule. A molecular ~~double~~ ^{dication} ~~ion~~ of this complexity (compared to Hg^{2+} or Kr^{2+} for example) might be expected to

show alternative reaction channels (to SET) provided the cross section for single electron transfer is low in the energy regime of study. Simple collision induced decomposition might not be interesting, but the reactions involving ion transfer and with a three body half collision (separating products) are plausible channels. It is quite interesting that the second product ion remains unobserved in these reactions. Measurement of the second ion would allow better resolution to be obtained and unambiguous interpretation of the differential cross sections.

Reactions of polyatomic ions

An example of one polyatomic reaction system⁶⁵ has already been given in this chapter (page 14-15). The reaction was seen to have considerable complexity. A second, similar system studied by Sonnenfroh and Farrar¹³⁸, illustrates the limitation of the technique. In the reaction of CH_3^+ with C_2H_4^+ , C_3H_3^+ is formed by the rapid sequential loss of two molecules of H_2 . In these conditions no useful dynamical information can be obtained without first observing and measuring the recoil of C_3H_5^+ transient. There are many other examples of the more complicated and varied reactions than just these two. As a rule of thumb the more atoms contained in a system, the less information can be derived about the detailed microscopic mechanisms.

Aims

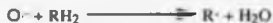
The aim of this study was to update the crossed beam instrument at the University of Warwick, to allow systems to be studied with more control over mass resolution and energy (both internal and kinetic) specification.

The study of four-centre reactions has been somewhat neglected falling between the smallest systems, from which much has been learned and the larger systems that groups would like to study in detail. One systems of interest is $\text{CS}^+ + \text{O}_2$. The interest lies in changes to the reaction dynamics between analogue reactions CS^+

and CO^+ . Some of the possible effects of low energy diffuse 3d orbitals and the higher angular orbital momentum have already been mentioned. There are also differences in other physical properties as with any homologous series.

There has been little attention paid to the study of angular resolved negative ion-molecule reactions. This may in part be due to the greater difficulty in producing negative ions precursors. Beam studies might be expected to solve some problems eg. the mechanism by which hydrogen abstraction occurs amongst simple hydrocarbons. For this reaction there are at least four plausible channels:

[31]



[32]



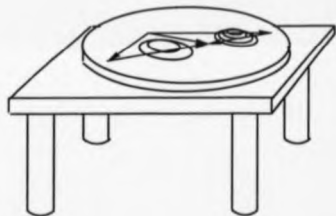
[33]



[34]



2



EXPERIMENTAL

Description of the instrumentation

Three different vacuum apparatus have been used during this study. They are the crossed-beam apparatus; containing two beam sources and a rotatable ion detector-analyser; a vacuum test cell for setting up the neutral beam; and a gas handling inlet system.

The crossed beam apparatus

Vacuum system (Figure 2.1)

The vacuum system consists of a high-and a low-vacuum. The low-vacuum manifold is constructed from a network of copper pipes. Semi-permanent, demountable joints are sealed with Viton elastomer O-rings. Four double stage rotary pumps ¹³⁷ evacuate the low-vacuum manifold. The network of pipes has been designed to be versatile, allowing pumps to be switched between several duties. The pressure is monitored continuously at strategic points in the vacuum lines using pirani ¹³⁸ and thermocouple ¹³⁹ gauges. The pressure is maintained of the order 10^{-2} to 10^{-3} mbar throughout the low-vacuum manifold.

The high-vacuum manifold is differentially pumped in three chambers: the large or main chamber and the neutral beam, and ion beam chambers. High vacuum is maintained by three diffusion pumps charged with Santovac 5 diffusion pump oil ¹⁴⁰. The pressure is monitored in each chamber by means of Bayard-Alpert type ionisation gauges ^{141,142} driven by IQC11 controller modules ¹⁴³. Each diffusion pump is backed by a dedicated mechanical rotary pump ¹³⁷ during operation.

The ion beam generator is located in a separate turret and is pumped by a 300 l.s⁻¹ diffusion pump ¹⁴⁴. The ultimate pressure for this chamber is 3×10^{-7} mbar and typical operating pressures are of the order of 1×10^{-8} mbar.

The neutral beam chamber is also pumped by a 300 l.s⁻¹ diffusion pump ¹⁴⁴. The turret is mounted on the top of a 500mm x ϕ 111mm (ϕ indicates a circular

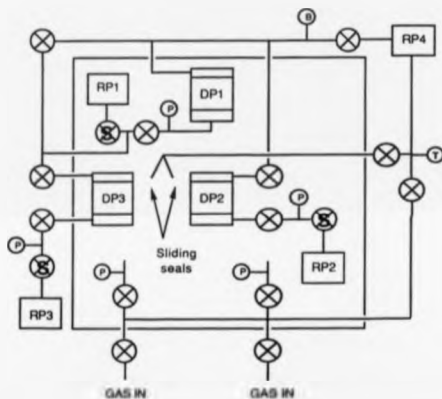
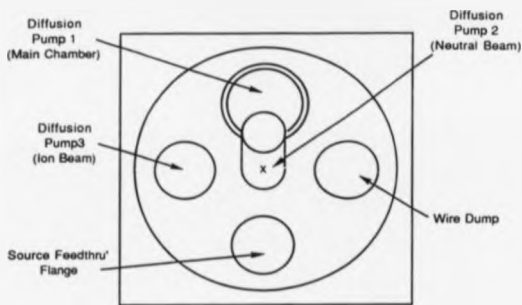


FIGURE 2.1: DIAGRAM OF THE INSTRUMENT FROM ABOVE AND BELOW AS A THIRD ANGLE PROJECTION

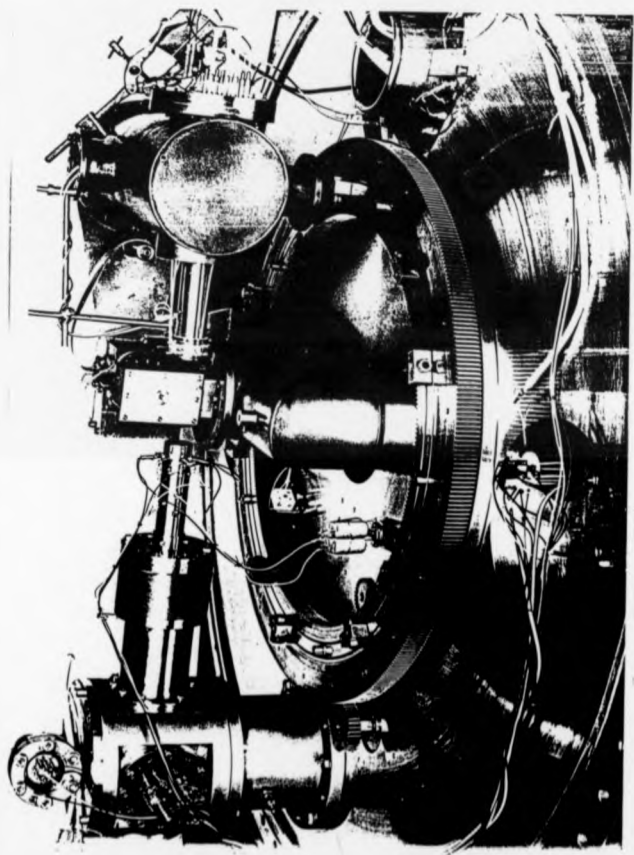
diameter) double elbow pipe which reduces the pumping speed at the orifice to 110 l.s^{-1} ¹⁴⁵. This chamber has an ultimate pressure of 8×10^{-7} mbar and is operated at up to 5×10^{-4} mbar.

The principal components of the instrument, including the two source chambers, are contained within the large vacuum chamber (Plate 1). This chamber is pumped by a 1700 l.s^{-1} diffusion pump ¹⁴⁶. The lid of this chamber consists of a $\phi 1\text{m} \times 0.75\text{m}$ bell with a thermally insulated copper inner jacket, to provide optional cryogenic differential pumping of condensable vapours. The interior of the apparatus is visible through a large porthole constructed out of 1" perspex sealed against a Viton O-ring. The lid of the main vacuum chamber is demountable by means of a 2D gantry hoist, to provide easy access to the working components. Under vacuum the lid is sealed by means of a large Viton O-ring positioned around an aluminium spacer. The ultimate vacuum, without cryogenic pumping, is about 6×10^{-7} mbar. Typical operating pressures in this chamber are of the order of 10^{-6} mbar. The liquid nitrogen supply for the cryogenic pump is made with an automatic level sensor and refill unit ¹⁴⁷ from a 200 l liquid reservoir ¹⁴⁸. Overpressure protection is provided using the main chamber pressure monitor.

The neutral beam vacuum test cell

Construction and performance

A self contained vacuum system was constructed (figure 2.2) to set up and to analyse the performance of the pulsed neutral valve ¹⁴⁹. This system is mounted on a trolley in order to make it portable and convenient to operate. Substantial benefits are achieved when using the test cell: the pump down time from atmospheric pressure to 10^{-6} torr is just three minutes for a favourable seal, compared with sixty minutes for the main vacuum equipment. In addition, the risk and consequences of a serious vacuum accident are both considerably reduced.



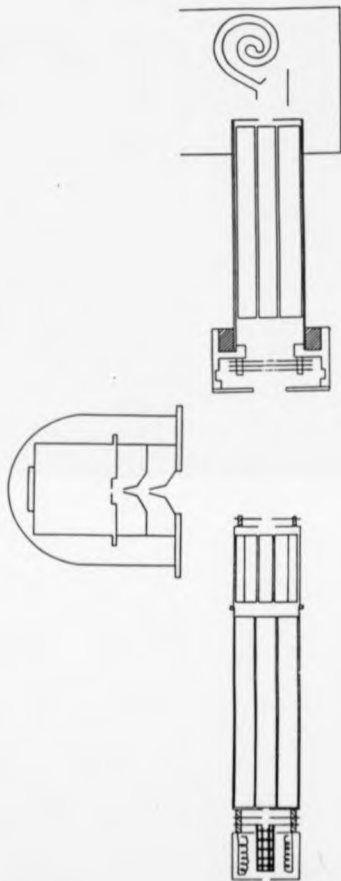


FIGURE 2.1A: DIAGRAM SHOWING THE MAIN COMPONENTS OF THE APPARATUS INSIDE THE VACUUM CHAMBER

The chamber is pumped by an oil vapour diffusion pump ¹⁴⁴, backed by a mechanical rotary pump ¹⁵⁰. Demountable sections of the low-vacuum lines are sealed with Viton O-rings. The rotary pump can be switched to roughing operation using Saunders valves ¹⁵¹ in the backing line. The ultimate pressure of this unit is of the order of 10^{-6} torr. The background is typically only 4.5×10^{-6} torr with a normally sealed valve mounted: indicating that the valve has a high "DC" leak rate.

Operation

The pulsed valve is assembled (supplement 2.1) and then mounted on the perspex flange at the top of the test cell. The valve is triggered and releases a pulsed jet of gas. The gas pulse passes through a fast-response ionisation gauge ¹⁵² before it is discharged directly into the orifice of a diffusion pump. Cations produced by the partial ionisation of the gas pulse are collected and processed by a fast preamplifier ¹⁵³. The preamplifier provides unit gain current-to-voltage conversion, with a 10ns rise time and fast slew rate. The output is displayed on a digital storage oscilloscope system ¹⁵⁴. Alterations to the pulse shape can be made as required using the built in adjustment of the valve and the pulsed beam control unit (figure 2.3).

The gas handling inlet system

Construction (figure 2.4)

The inlet system has been designed to be a portable and versatile tool. The system is compact and self-contained and all components including flow control units are trolley mounted. The vacuum line is demountable and is centrally pumped from a common mechanical rotary pump ¹⁵⁰ equipped with a glass foreline trap.

The vacuum system consists of a network of stainless steel 0.25" (Swagelok ¹⁵⁵ sealed), 0.5" (Cajon ¹⁵⁶ and OHFC copper gasket ¹⁵⁶ flange sealed) and assorted 1" (muff coupled ¹⁵⁷) tubes. VQ GH97 ¹⁵⁸ valves are mounted on the wider bore (0.5") stainless steel tubes. These valves restrict the safe upper limit for high

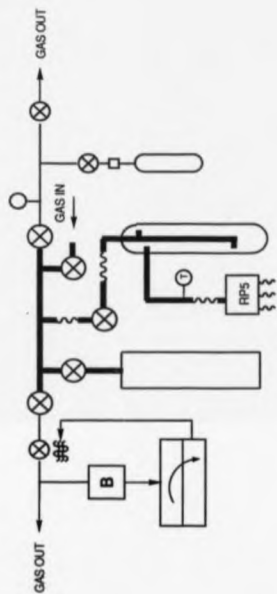


FIGURE 2.4: THE SCHEMATIC LAYOUT OF THE GAS HANDLING INLET SYSTEM

pressure operation to just 3 bar ¹⁵⁹. The gas handling system has been designed to withstand the use of corrosive materials and reagents in several forms.

Modes of operation

Volatile liquids can be introduced from a small quickfit test tube (B10 standard taper) connected by a glass to metal seal to the swagelok/0.25" stainless steel tubing. The temperature around the liquid reservoir is reduced in order to maintain a slight pumping effect. This ensures that the saturated vapour pressure is controlled by the equilibrium established between the liquid surface and the vapour above it, and not by the equilibria of condensation on the walls at room temperature. The vapour pressure can be predicted from the Clausius-Clapeyron ¹⁶⁰ equation to within 5% under these conditions.

Substances which are gaseous at room temperature can be mixed or stored in a stainless steel reservoir. Alternatively, provision is made to use gases directly from a regulated gas cylinder. The gas capacitance manometer (baratron) ¹⁶¹ can be connected to the instrument side of a solenoid operated feedback valve ¹⁶². The pressure is regulated from the measurements recorded by the baratron head by a set of feedback controllers ¹⁶³.

Detection

The ion detector (figure 2.5)

During the period of study the configuration of the rotatable ion detector and energy analyser has not been altered. In its present configuration this consists of an entrance plate leading to a retarding potential difference (RPD) energy analyser, a quadrupole mass filter ¹⁶⁴ and a channel electron multiplier ¹⁶⁵.

The RPD analyser consists of three independently charged electrodes. The electrodes are fabricated from thin circular stainless steel plates punctured by a central 5mm aperture. A fine stainless steel wire mesh is stretched, and spot welded,

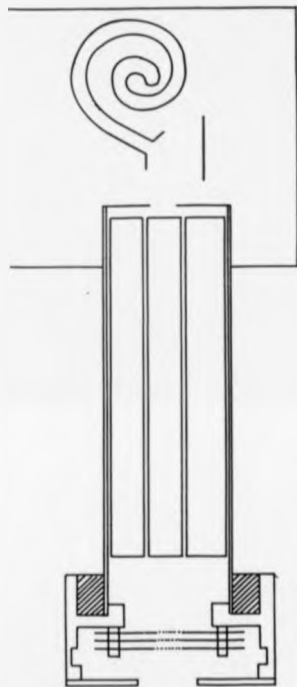


FIGURE 2.5: DIAGRAM SHOWING THE DETAILED CONSTRUCTION OF THE ROTATABLE ION DETECTOR

flat across the aperture. The transmission of the central electrode mesh is 73% (180 wires per inch (wpi)) ¹⁶⁶ and for the first and third electrode mesh is 81% (100 wpi) ¹⁶⁶. Under normal operating conditions the first and third electrodes are retained at earth potential and the central electrode is charged with a voltage ramp.

The ions passed by the RPD energy analyser travel through an electrode free region before mass analysis. The mass separation is made using a quadrupole mass filter (QMF) ¹⁶⁴ operated at 2MHz and tuned along a DC:RF scan line of 0.35 ± 13.5 VDC = VRF. Ions exiting the QMF are detected by a closed-ended channel electron multiplier (CEM) ¹⁶⁵, which is set off axis to reduce the noise level caused by stray high energy radiation and neutral molecules. The detector can be rotated under vacuum in both the azimuthal and meridional planes using a series of gear trains extending from out of the vacuum system. The sliding seals at the vacuum to atmosphere interlock are pumped to minimise the risk of virtual leaks.

The ion beam can also be monitored using a plate ion collector constructed and attached to the ion detector such that it can be rotated into the alignment with the primary ion beam.

TOF analysis of the neutral beam

A time of flight (TOF) analyser can be installed into the vacuum system for the purpose of characterising the neutral beam. This consists of two IQ5G ion gauges ¹⁵⁷, with their glass shields cut away and mounted on aluminium supports. The supports inhibit the movement of the rotatable detector and must be removed from the vacuum system during normal operation. The output is displayed on a digital storage system as in the vacuum test cell. *Hard copies* of the oscilloscope output have been obtained with an oscilloscope camera ¹⁶⁷, or by dumping data from the digital storage adapter to a dot matrix printer.

Beam generation

Ion beam generation (figure 2.6)

The ion beam was generated, by electron bombardment of the precursor gas or vapour, in a Bayard-Alpert type of ion-source. The ions were extracted from the ion source using a simple lens system, and injected into a naked quadrupole (VSW Mass analyst 200). The ion beam was then focussed by an electrostatic octipole lens, collimated and focussed using a final series of electrodes (denoted the exit assembly). The mass filters used in this project were commissioned as a special edition from VSW.

Both of the quadrupoles, in the source and in the detector, were originally made to be residual gas analysers. The detection assembly of these residual gas analysers was removed and discarded. The naked quadrupoles were incorporated into the vacuum equipment as shown in fig. 2.1a and 2.5.

The configuration of the ion beam generator has been changed many times in the duration of this study. The specific configurations and methodology used in shown in figure 2.6 and chapter 3. experiments are discussed in supplement 2.2. The basic apparatus for ion beam formation is: an electron impact source, a quadrupole mass analyser, an astigmatic octipole focuser ¹⁶⁸ and several electrostatic lenses and collimating apertures.

The quadrupole mass analysers in the ion source and detector are based on commercial residual gas analysers ¹⁶⁴. The system was produced as a special edition and has been further modified in this laboratory.

The generation of a neutral beam

The neutral beam is mounted into a differentially pumped turret which can be rotated from outside the vacuum system. During this study, four neutral beam generators have been used. They are a single glass capillary, a glass nozzle, a multichannel scintered glass capillary array ¹⁶⁹ and a pulsed valve ¹⁷⁰. The glass nozzle and capillary are mounted in an X, Y, pitch and yaw adjuster. The capillary

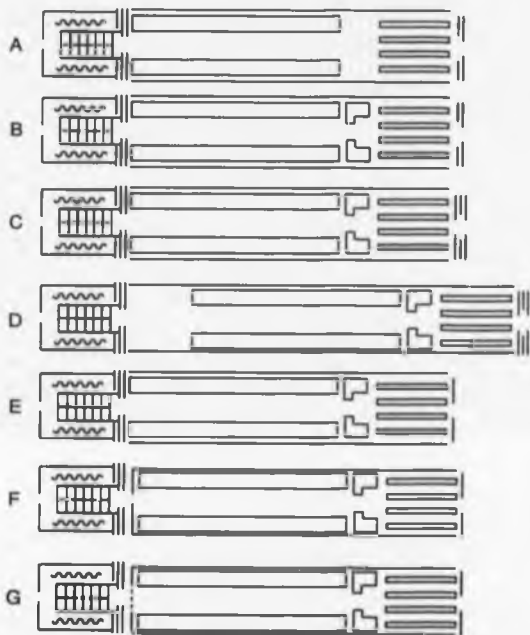


FIGURE 2.6: SOME CONFIGURATIONS OF THE ION BEAM SOURCE USED IN THIS WORK.

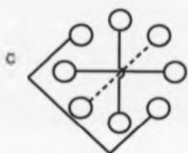
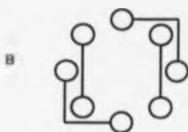
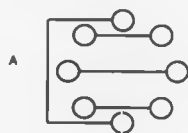


FIGURE 2.6 (CONTINUED): THREE CONFIGURATIONS OF THE OCTOPOLE.

array and pulsed valve are mounted in an enclosed box on to which a different, equal range adjuster is built.

The performance and specific experimental details for the pulsed neutral beam are presented in chapter 4. Experiments using other neutral beam sources have been performed to look for evidence of scattering. In these experiments the neutral beam is unmodulated and a change in detected product intensity, reaction product, angular and energy disposal is used to correlate results.

Electronic apparatus and detection

The treatment of the pulsed output from the CEM detector is best described by block and flow diagrams. (Figure 2.7-2.9). Several pieces of electronic equipment have been constructed during the period of study for this project. The circuit diagrams for these are shown in figures (2.11-2.14).

Free electrodes

The remaining free electrodes, shown in the configurations drawn in figure 2.6, can be raised to desired voltages by 30W power supplies ¹⁷¹. These electrodes are connected to a clean earth via a suitable capacitor to filter off noise.

The electrostatic octopole

The octopole is connected using the configurations shown in figure 2.6.(cont). Voltages are supplied from power supplies, stepped down over a potential divider and measured at source. The measured voltage can be used as a guide to the ^{actual} applied voltage. Empirical determinations suggest that the applied voltages measured at the voltage divider are reduced to 80% of their value when measured on the octopole rods inside the equipment.

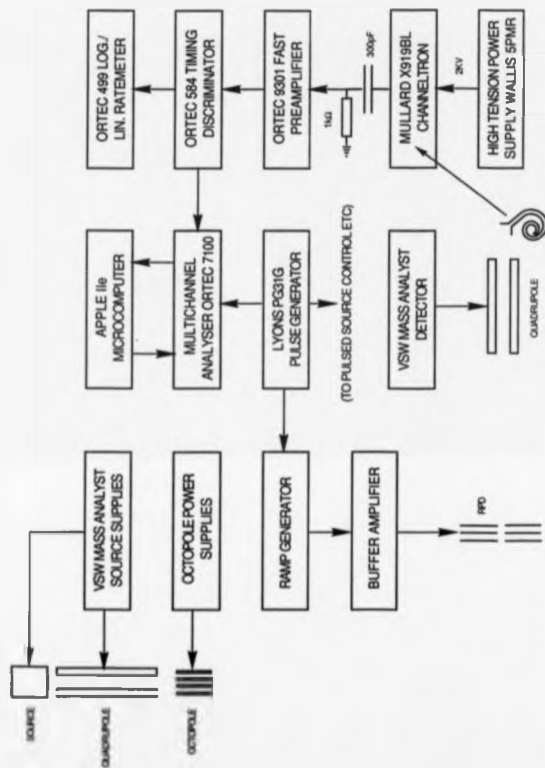


FIGURE 2.7: BLOCK DIAGRAM OF THE ELECTRONIC CONTROLLER INTERCONNECTIONS

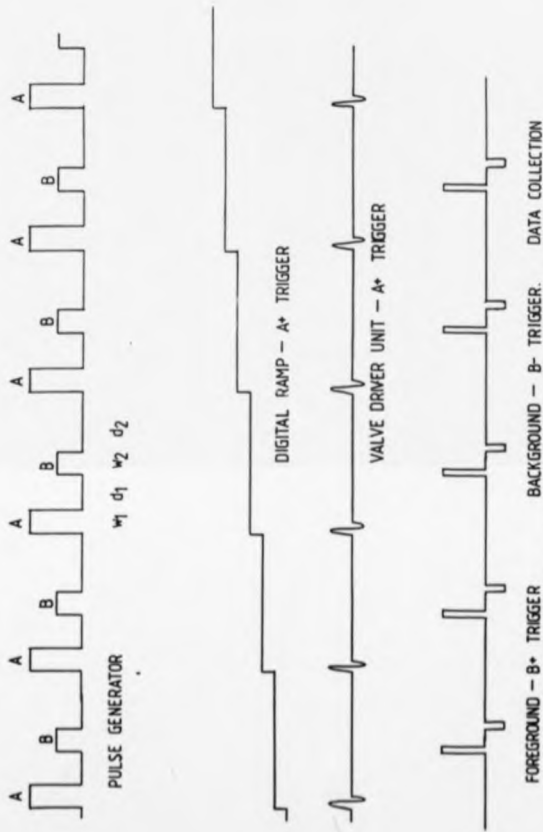


FIGURE 28: DIAGRAM OF THE TRIGGERING SEQUENCES FOR A CROSSED BEAM EXPERIMENT USING A PULSED NEUTRAL BEAM

```

START

FOR SWEEPS = 0 TO SWEEPmax

    DIGITAL RAMP = 0

    FOR CHANNELS = 1 TO CHANNELmax

        FLAG VALVE TO BEGIN PULSE

        TOFA DELAY TO DETECTOR

        COLLECT FOREGROUND BEGIN (selective start)

        COLLECT FOREGROUND END (selective stop)

        PULSE DATA END

        DUMP DATA

        COLLECT BACKGROUND BEGIN

        COLLECT BACKGROUND END

        rem. Same accumulation width

        DUMP DATA

        DIGITAL RAMP = DIGITAL RAMP + VOLTAGEIncrementDELTA

    NEXT CHANNEL

    SUBTRACT BACKGROUND SWEEP PER CHANNEL

NEXT SWEEP

STOP

```

FIGURE 2.9: LOGIC OF DATA COLLECTION FOR EXPERIMENTS SUCH AS
FIGURE 2.8

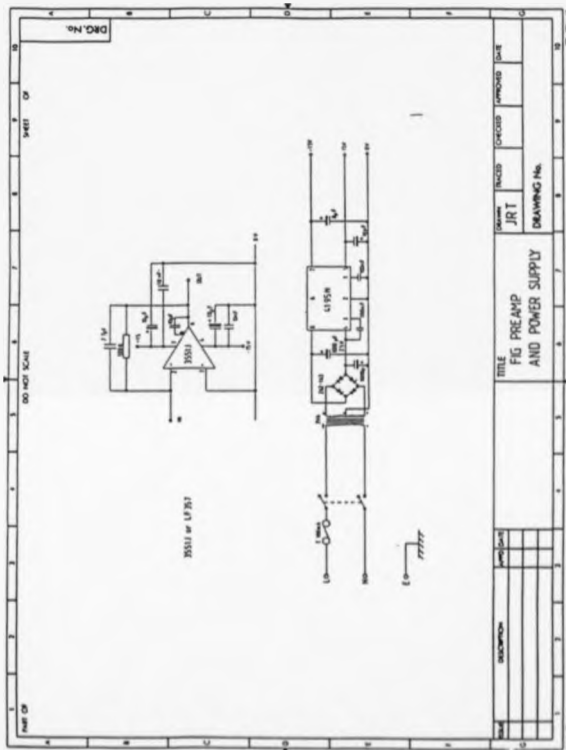


FIGURE 2.13: CIRCUIT DIAGRAM SHOWING THE FIG PREAMPLIFIER AND ITS POWER SUPPLIES

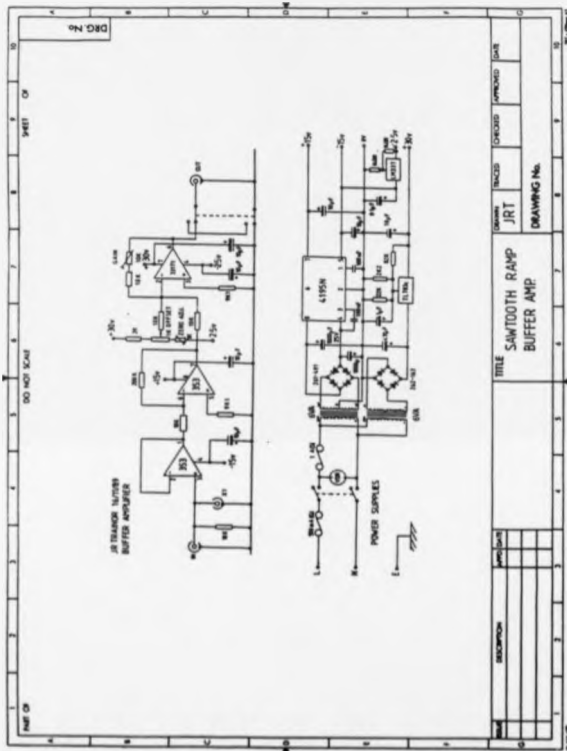


FIGURE 2.14: CIRCUIT DIAGRAM FOR BUFFER AMPLIFIER OF THE PRECISION RAMP

Alignment

The experimental apparatus has been aligned using a travelling telescope system equipped with spirit levels. The apparatus has a series of alignment marks cut during machining to which adjustment and alignment is referenced. The neutral beam elbow joint contains a socket coaxial with the centre of the table (tolerance $< 0.1\text{mm}$), checked by viewing the motion of the end of the point whilst the neutral beam turret is rotated by 90° .

A machined brass pointer is positioned in the central socket so that the tip of the pointer, the centre of the ion exit plate, and cross hairs positioned on an optical window behind the ion source are brought into line (with the ion source removed). The neutral beam is aligned at 90° to this original direction and the alignment is checked by placing a plane mirror at 45° to the ion beam through the central plane of the table, and superimposing the image of the ion beam exit plate on the neutral beam source, seen by removing the mirror.

Computation of ion energy spectra

Integral ion energy spectra were accumulated in a multi-channel analyser (Ortec 7100) using a *multi-channel scaling* mode. The spectra (or profiles) were transferred using an IEEE 488 Bus into an Apple IIe desk-top minicomputer. The data were converted from ASC11 to integer inside the minicomputer and differentiated by subtraction of adjacent channels.

The principal problem associated with using this method for the extraction of ion energy spectra is discussed in the section on analysis of errors below. Provision was made in the analysis to normalise the error of each channel. This was not found to be generally helpful.

Analysis of errors

The function probed by the retarding potential difference energy analysis is a continuous function describing the distribution of energies $I(v)$.

The integral of this ion energy function is sampled repeatedly by applying a stopping potential to reject all ions below a threshold energy $V(r)$. The energy is scanned as a time dependent voltage, turning the analysis into a stochastic function. Ion formation under given conditions is a random process, occurring with a constant rate. The randomness of the formation is not affected by an orderly transport through the ion optics, thus the energy content can be described by a Poisson probability function $\frac{\lambda^x}{x!} e^{-\lambda}$.

[35]

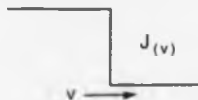
$$e^{-\lambda} \frac{\lambda^x}{x!}$$

λ = sweep width \times channel width $\times \sum I(v)$ for all v .

I = flux scaling X = Poisson's random variable.

For simplicity, we consider a non-continuous function at a resolution below the sampling width. The limit is effectively infinite resolution or singularity in the energy distribution $I(v)$. Such a function leads to a true step function in the integral ion energy spectrum $J(v)$.



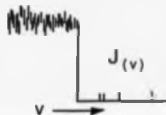


$$\text{For } 0 \leq v_r < V_{IES} \quad x = x_1$$

$$\text{For } v_r > V_{IES} \quad x = 0.$$

V_{IES} = A voltage in the ion energy spectrum, V_r = ramp voltage.

By chopping up the v axis into a series of time or voltage windows (channels), two functions emerge. For channels with $(v + \delta v) < V_{IES}$ there is one Poisson probability function with a most probable value x_1 . For those with $(v + \delta v) > V_{IES}$ there is another, equal to zero. After an experiment sampling $J(v)$ we might obtain:



A plot of the value x_v against frequency of occurrence would approximate to the density of individual frequencies of occurrence characteristic of each function. The first moment of this statistical sample is the mean = λ . The second (central) moment is the variance also = λ . The standard deviation is therefore $\sqrt{\lambda}$. This can be used as a suitable index of the random spread in the sample. To obtain information any information about $I(v)$, from a measure of $J(v)$, requires a transformation to be made. That transformation is the differentiation of $I(v)$, and is made by the subtraction of adjacent channels:

[37]

$$I(v+1) - I(v) = J(v+0.5)$$

The transformation causes noise amplification as shown below.

The standard deviation in both $l_{(v+1)}$ and $l_{(v)}$ is $\sqrt{\lambda}$, for channels falling into the range $0 \leq v_r < v_{r+1}$. The standard error in the difference $J_{(v+0.5)}$ can be calculated by combining the errors in each:

[38]

$$\left\{ \frac{\sigma l_{(v+1)}}{l_{(v+1)}} \right\}^2 + \left\{ \frac{\sigma l_{(v)}}{l_{(v)}} \right\}^2 = \left\{ \frac{\sigma J_{(v+0.5)}}{J_{(v+0.5)}} \right\}^2$$

In this special case $\sigma J_{(v+0.5)} = \sqrt{(2\lambda)}$.

For real distributions which may be as follows:



there are a significant number of single channels for which a unique Poisson distribution exists. Hence, only one datum (x_i) is available on the distribution function. The form of the function is not known (Poisson), hence the standard deviation can then be used to estimate if any given point is representative of the mean.

Nb. The specific probability of x_i equalling any particular single value is very small for large λ , i.e. $P(x_i = g) \rightarrow 0$ as $\lambda \rightarrow \infty$.

Normally, it is not possible to assume the form of $l_{(v)}$ probed and in the remaining cases it is unadvisable to do so. In these conditions the value of λ cannot be calculated. The reason for this is that real distributions are not singular and for a

usable choice of channel ^{width} or window on to the function $J(v)$. $J(v)$ is a continuously changing function of *partial flux*. Thus, the best approximation to x_i is x_i , and for the probable error is $\sqrt{x_i}$ (x_i is the number of counts actually recorded). The deviation of each single value from the most probable for a given Poisson function is related to ~~the third moment~~ $\lambda^{1/4}$. In the differentiation of real profiles the error is well represented by $\sqrt{(x_{v+1} + x_v)}$; nb. this is the general form of the error considered before as a special case.

A small, low energy component of $I(v)$ can be swamped by the error from much larger contributions to $I(v)$, because the error in a channel of $J(v)$ is due the sum of components higher than v . This problem is not encountered for band pass energy analysers such as electric sector analysers, and is a draw back specifically in the use of RPD analysers.

The analysis of errors here gives a background to the problems of data handling. Specific errors occur in other places eg. the random variation of pulses in the neutral beam target adding a *channelwise* error (which is independent of the voltage ramp); or the limit to resolution caused by field penetration between the mesh wires proportional to V_r and falling off with r^2 .

General experimental practice

All changes in experimental set-up are recorded in full in a laboratory note book updated daily. An experimental configuration is current for all investigations using that apparatus until notification of a new set-up is given. The variable conditions are noted on a specially designed spread sheet (figure 2.18), extraordinary conditions and observations are recorded separately following this sheet under coded heading of the investigation. It is intended that by this policy, all results and observations are available for reappraisal in the light of new knowledge or better insight.

DATE:

EXPERIMENT REFERENCE:

AMBIENT TEMPERATURE:

°C

CHAMBER	SAMPLE	INLET PRESSURE (mbar)	STATE	TEMPERATURE (°C)
ION				
NEUTRAL				

CHAMBER PRESSURES (mbar)

BACKING PRESSURES (mbar)

MAIN CHAMBER

 $\times 10^{-7}$

DP1 BACKING:

 $\times 10^{-7}$

NEUTRAL CHAMBER

 $\times 10^{-7}$

DP2 BACKING:

 $\times 10^{-7}$

ION CHAMBER

 $\times 10^{-7}$

DP3 BACKING:

 $\times 10^{-7}$

SOURCE QUADRUPOLE

DETECTOR QUADRUPOLE

FIRST MASS

amu

amu

SPAN

%

%

RESOLUTION

%

%

SCAN RATE

amu/s

amu/s

FOUR DIAB

V

V

ION SOURCE

OCTOPOL

ELECTRON ENERGY

eV

1(blue,black)

V

EMISSION CURRENT

mA

2(green,pink)

V

ION FOCUS

V

3(yellow,yellow)

V

ION ENERGY

eV

4(red,red)

V

EXIT PLATE

V

RFD SHATER POWER

W

NEUTRAL SOURCE

ENERGY ANALYZER

PULSE WIDTH VARIATION

%

PLATE 2

V V/s

REpetition RATE

Hz

PLATE 3

V

TRIGGER

vs

TRIGGER

vs

HIGH THRESHOLD

eV

DISCRIMINATOR THRESHOLD

PULSE GENERATOR

CHANNEL 1

PERIOD

s

WIDTH

s

DELAY

s

CHANNEL 2

PERIOD

s

WIDTH

s

FIGURE 2.15: SPARE DATA SHEET

The reproducibility of experiments has been enhanced by the use of the spread sheet. A set of data can be dialed up to reproduce the previously recorded data to better than 10%. A slight adjustment is usually necessary to tune the ion beam after such a cycle, due to local variations presumed to include unavoidable surface charging etc.

Energy profiles are smooth processed using a five point polynomial fit option of the MCA. All energy profiles recorded in a laboratory note book are archived. They^{is} archived^{is} contained on 5.5" floppy disc. To reduce storage requirements only raw data are archived in a manner suitable for processing or transferral back to the multichannel analyser for smoothing.

Computer programs for simulation and data transfer

Several simple computer programs, to expedite the processing of data, have been written for an Apple IIe microcomputer using Applesoft basic and DOS 3.3. The data transfer programs are modified from assembler source code (EG&G Ortec Apple IIe/7100/01A data transfer routines). These programs (appendix 3) are inefficient, but functional. There is considerable scope for improving these programs.

A commercial ion optic program (SIMION) was used to model parts of the apparatus and is discussed in chapter 3. A data processing program for the output data from SIMION is presented in appendix 3, with illustrative data from one run.

Supplement 1

Setting up the pulsed valve

Silicone procedure

Previous silicone sealant was removed mechanically from the ribbon carrier and nozzle orifice (no solvent has yet been found to dissolve the silicone). The naked

surface of the ribbon carrier was primed, taking care not to get primer down the nozzle orifice. A needle was inserted into the orifice and set perpendicular to the base plane of the nozzle. Fresh silicone was laid on to the ribbon carrier. A small piece of acetate sheet was cut with a central hole and placed over the needle and on to the silicone. The sheet was manipulated to remove air bubbles in the layer, and to ensure that the layer was flat and thin. The silicone was left to dry for a minimum of 12 hours, then the needle was removed. The acetate sheet was frozen with solid CO₂ and carefully peeled away. Excess silicone was cut from the ribbon carrier sides with a scalpel and the surface inspected under a microscope for flaws.

Ribbon installation notes

It has been found that, if the valve was constructed before the installation of the ribbon, then the procedure is simplified. Ribbons of approximately 1 mm width were cut from a sheet of phosphor bronze ¹⁷³ (50 x 50 mm x 25 µm) with a pair of sharp scissors. A flat ribbon was chosen and placed into the jaws and clamped into position. The ribbon was manipulated until it was taut and lying flat along the length of the ribbon carrier. The solder was applied *in situ* to the ends of the ribbon, taking care to minimise the time that the ribbon was heated, as this promotes brittleness and ultimately fracturing of the ribbon. Ribbons of the wrong dimensions, or which were curled or twisted were discarded.

Supplement 2

A jet test for nozzles

Jet tests were designed to expose problems with the cut of the nozzle orifice and to provide a quality control test for the rejection of unsuitable nozzles. In one experiment ^a pressurised stagnation volume of water was applied to the nozzle from the forward and the reverse direction. The divergence of the beam, from a reference plane (the base), is estimated by trigonometric methods. Ultimately, the nozzle is

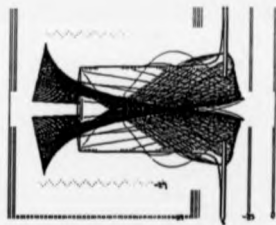
rejected if the jet of water will not pass through the skimmers assembly, located on to the valve base plate. This has been machined to be coaxial and orthogonal to the ~~datum, if the nozzle orifice is ideal.~~ ^{for an ideal nozzle}. Similarly, pressurised He was used to check if gas from the naked valve could penetrate through the skimmers, when the valve was mounted in the main apparatus.

Supplement 3

The line of sight experiment

A performance test for the ion optics is a line of sight experiment. In such experiments the detector and the ion source were aligned coaxially, and the ion optics and mass filters grounded. The characteristics of the source were recorded as a reference and the performance of other equipment recorded. The individual effects were investigated by systematically introducing each new piece of equipment.

3



ION OPTICS

Introduction to ion optics

Many of the physical and mathematical principles used in ion optics were known before the discovery of the first charged particles. The subject area can be divided up into static field ion and electron optics, and dynamic fields. The former case has been developed continuously and is well understood. Ion physics in the gas phase has been important in chemistry in the post war period (1945-present) when the power and possibilities of mass spectrometry as an analytical technique became apparent. Dynamic-field ion physics, however, is more recent and less well understood especially within chemistry.

Concepts of electrostatic ion optics

Historical basis

Hamilton 174,175 set up the basis for ion optics in describing the motion of a particle as a function of velocity and position. Using the integral of momentum over a given path, the *action* of the particle is described.

[39]

$$S = \int_A^B mv \, ds$$

S = Action of the particle, v = Velocity of the particle, ds = Small step along the path A, B, m = mass of the particle.

Applying the principal of least action (Maupertuis), the fractional change in path must vanish i.e. $\delta s \rightarrow 0$. Thus, the integral is minimised and the trajectory of the particle is described by the shortest path between A and B. For constant mass and velocity; and in the absence of external forces, the shortest path of a particle must also be the shortest time of travel. This can be shown from an alternative perspective. Expressing the integral again as a function of time:

[40]

$$S = \int_A^B m v^2 dt$$

m, v, S = defined as above, dt = short interval of time during which the particle moves closer towards B.

and applying the principle of least time (Fermat), the integral is again minimised and the same conclusion is reached.

In the case of non-relativistic motion, as described above, the energy of an ion at a point in an electrostatic field can be described exactly. The total kinetic energy (E_T) is given by sum of the difference in electrostatic potential between the point of interest (V_I) and the point of formation (V_f), and by the thermal kinetic energy (E_{MB}) prior to ionisation.

[41]

$$E_T = (V_I - V_f) + E_{MB}$$

Equation quoted for units of electron volts.

Only a small error is introduced if the prior thermal motion ($<0.1\text{eV}$) is ignored.

The equation can be then be written:

[42]

$$\frac{1}{2} m v^2 = e(V_I - V_f) = e\Delta V$$

Greater accuracy is obtained if the ion energy is referred to the potential of the formation point, especially at low energy.

The change in velocity of an ion in different electric fields, is analogous to the change in the velocity of light in a refractive medium. It can be shown¹⁷⁴ from these principles, that a practical refractive index for a charged particle moving in an electrostatic field is:

$$n = \sqrt{V}$$

n = Refractive index, V = electrostatic potential.

Thus, electrostatic fields exhibit the lensing phenomenon when an ion passes into regions of different potential. The analogy to light optics is limited for several reasons. One of these is that the electrostatic potential is *soft*, infinite and changes continuously as a function of distance from a point. The actual trajectory of the ion is modified continuously rather than sharply, through a gradually changing force between the regions of different electric field gradient. The refractive medium or lens in light optics in contrast is hard and finite, well defined and changes suddenly at an instant in the flight path. These differences gives rise to some idiosyncrasies in light optics, an example is the diverging lens. In ion optics, there is no formal equivalent of the diverging lens, since any lens ultimately focusses either positively or negatively charged particles passing through the lens and returning into the prior electric potential.

The equivalent lens

Provided the transformation to the final trajectory only is required, then a useful approximation to the action of an actual lens is the *equivalent lens*. This is the phenomenological lens which causes an equivalent deflection of incident ion trajectories, but which acts suddenly, like a hard optical lens.

There are six cardinal points of the equivalent lens: two foci, two principal points and two nodal points. These six points can be used to describe the action of the idealised equivalent lens. The points are distances from an axial reference position at which the six planes intersect the axis perpendicular to its direction of propagation. Rays incident on a perfect lens and travelling parallel to the axis are brought to a common axial point called the focus. The conjugate focus is defined similarly for parallel rays travelling from the reverse direction. The definition of

the focal lengths requires a reference point and two are in common use. The midfocal length is referenced to the geometric centre of the lens and the focal length is referred to the appropriate principal point.

The principal point is the projection of the point on to the axis, at which the extrapolated portions of the initial and final trajectory meet. The two principal planes have unit magnification, i.e. a ray entering the lens travelling towards a point on the first principal plane, exits the lens as if it has come from the conjugate point on the second. Physically these planes represent the hard refractive faces of the equivalent lens. The outstanding difference between this ion optic lens and the optical lens is that the principal planes are crossed over for the ion optic case.

Nodal points are the points on the axis towards which a ray can be directed to emerge from the second face with exactly the same angle as the initial angle of incidence.

These properties only apply to lenses where the midfocal lengths lie outside the principal planes, i.e. the rays do not cross over within the lens. A diagrammatic summary is provided in figure 3.1.

The paraxial ray equation

Rays which are close to the axis, with angles of incidence relative to the axis such that $\sin\theta \approx \theta$, are termed paraxial rays. A special analytical formula for these rays has been devised called the paraxial ray equation [174,175]

[44]

$$\frac{d^2 r}{dz^2} + \frac{\phi'}{2\phi} \frac{dr}{dz} + \frac{\phi''}{4\phi}(z) = 0$$

ϕ = Electrostatic potential, ' indicates differentiation with respect to z .

" indicates double differentiation with respect to z , z is the axial direction and r the radial direction in cylindrical polar coordinates.

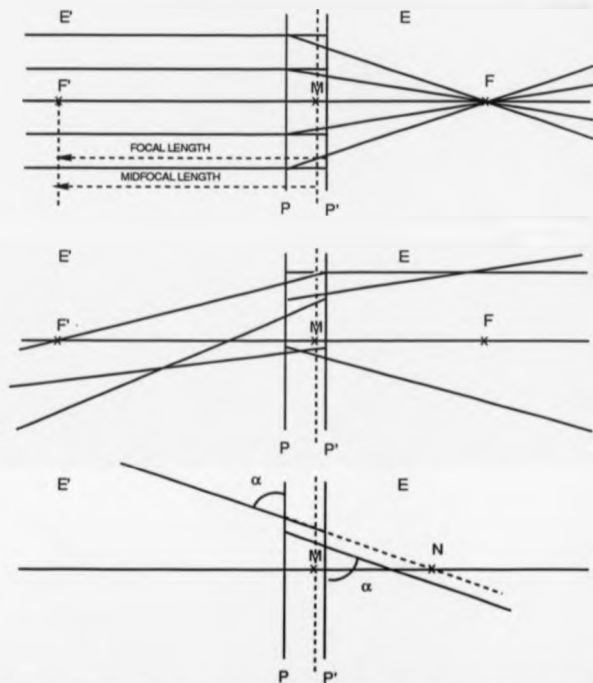


FIGURE 3.1: RAY DIAGRAMS TO ILLUSTRATE THE CARDINAL POINTS IN AN EQUIVALENT LENS.
 P, P' - PRINCIPAL POINTS, N, N' - NODAL POINTS AND F, F' - FOCAL POINTS.

Note the formal equivalence between v and ϕ . It is sometimes more convenient to express the electrostatic potential in terms of a Greek character, for example when differentiation occurs in the equation. This convention is used in this manuscript.

This approximate equation is obeyed by paraxial rays. In the derivation it is assumed that the only significant terms in the description of the electrostatic potential are the first order terms. Examination of the paraxial ray equation is instructive.

The first point to note is the absence of a term in (e/m) . The equation does not differentiate between the trajectories of ions of different mass, hence the trajectories are the same for all ions provided that the energy is constant. The equation is also dimensionless and only depends linearly on the electrostatic potential (ϕ). The position of the cardinal points are referenced to the size of the lens only, hence trajectories are conserved when the applied potential is raised and lowered proportionally for all the electrodes.

The potential field

The solution of a problem of ion optics can be greatly enhanced by the use of models. Trajectories can be run over a potential function in what are known as ray-tracing simulations. In any ray-tracing study, the form of the potential function must be known. Several methods of calculating the potential function are available. The potential function required is normally the Laplace equation, which assumes no space charge:

[45]

$$\nabla^2 \phi = 0$$

$$\nabla^2 = \frac{d^2}{dx^2} + \frac{d^2}{dy^2} + \frac{d^2}{dz^2} \text{ operator (the Laplacian operator), } \phi = \text{electrostatic potential.}$$

The most convenient method of trajectory study, since the advent of the powerful desk-top microcomputer, is the iterative relaxation method followed by the direct solution of the equations of motion of the particle.

Computer modelling of trajectories

The relaxation method is quite an old technique used to solve the Laplace equation and is used in the computer program SIMION ¹⁷⁶ and in an alternative program written by Davis ¹⁷⁷. The principal of the technique is to break up the active space between electrodes into small manageable portions. The potential function is approximated along the independent directions of the array by linear gradients over these sections.

For example, consider a 2D Cartesian electric field gradient varying in $\frac{x}{x}$ and $\frac{y}{y}$. Figure 3.2. A grid is created covering the active space. The voltage at a given point is related to connected neighbouring points as follows:

[46]

$$\frac{V_1 - V_0}{D} - \frac{V_0 - V_3}{D} = \frac{d\phi}{dx_{1,0}} - \frac{d\phi}{dx_{0,3}} = D \frac{d^2\phi}{dx^2} = 0$$

[47]

$$\frac{V_2 - V_0}{D} - \frac{V_0 - V_4}{D} = \frac{d\phi}{dy_{2,0}} - \frac{d\phi}{dy_{0,4}} = D \frac{d^2\phi}{dy^2} = 0$$

V_i = Voltages : the relationships of these is seen in figure 3.2.

D = Grid spacing, x, y = co-ordinates, ϕ = electrostatic potential

Setting the field gradients to zero as required by the Laplace equation, an expression for V_0 can be obtained:

[48]

$$V_0 = 0.25 (V_1 + V_2 + V_3 + V_4)$$

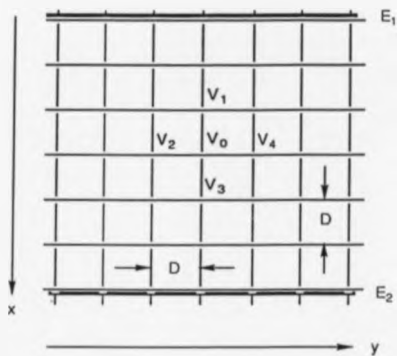


FIGURE 3.2: DIAGRAM TO SHOW THE NETWORK ESTABLISHED FOR A COMPUTER CALCULATION OF THE ELECTRIC FIELD GRADIENT.

There is a residual value after the calculation of V_0 which is an error term in the quantity V_0 . The accuracy of the potential distribution is controlled by the size of the array (reduction in D and increase in the number of points) and the acceptable residual. The speed of convergence is strongly dependent on efficient use of the computer time. Efficiency is enhanced by the grading of initial potentials, and the order in which the potentials are relaxed. A technique called *overrelaxation* of the potential also reduces the time taken to reach the asymptotic potential.

The equations of motion for the particle studied are solved directly to obtain, iteratively, the particle trajectories.

Aberrations: operation of a real lens

Extension of the significant terms considered in the expansion for the electric field generated by an electrostatic lens to third-order theory, leads to five new terms in the potential function called aberrations. They are the spherical aberration; coma; astigmatism; distortion; and curvature of field. These aberrations are the corrections of the inadequate first order electrostatic approximation.

The full theory extended to electro- and magnetostatics yields many more aberrations. Including the magnetic focussing, there are eight third-order geometric corrections. Several more geometric aberrations are obtained if the fifth order terms are considered. In combination with the geometric aberrations there are also four electronic aberrations. The errors that are relevant to this study are the five third order electrostatic aberrations and two electronic aberrations: the space charge error and the chromatic aberration. In the transport of ions as in the present crossed beam ion optics, the spherical aberration has the greatest effect upon the quality of the beam. A sharp image of a defined object is not required, in producing a collimated reactant beam. The principal effects of coma, astigmatism, distortion, and curvature of field are of blurring the image, beam spread is not seriously affected provided these are small.

The spherical aberration arises from the differential refraction of paraxial and marginal rays. This gives rise to different foci, which spreads the focus along an axial line. The chromatic aberration produces the same effect from a different cause. Different components of energy within the beam incident on the lens at a particular point, with a defined angle, are refracted by different amounts. The addition of space charge limits the maximum current density that can flow through a volume per unit time. The latter effect is caused by the mutual repulsion of the components of the beam and limits the size of a focus. This effect is pronounced at low energies. This section is summarised in figure 3.3.

Electrodynamic fields: operation of the quadrupole mass filter

A quadrupole mass filter consists of four electrodes arranged axially symmetrically 178-180. The opposite pole pairs are connected electrically and a sinusoidal potential is applied to each. The potential distribution generated inside the electrode space can be described by the equation:

[49]

$$\phi_1 = [U + V \cos(\omega t)] \cdot \frac{x^2 - y^2}{2r_0^2}$$

ϕ_1 = Electrostatic potential at a time instant, t ; t = Time, r_0 = axis to quadrupole rod minimum distance, U = DC applied potential, V = Peak maximum radio frequency applied potential, x, y = Coordinate variables in the direction of the rod pairs, ω = Frequency of the applied RF potential.

Strictly, this equation only applies to an ideal quadrupole set, consisting of four infinitely long, perfectly aligned rods, with hyperbolic cylindrical faces. Most quadrupoles by contrast have circular cylindrical electrodes. The central portion of

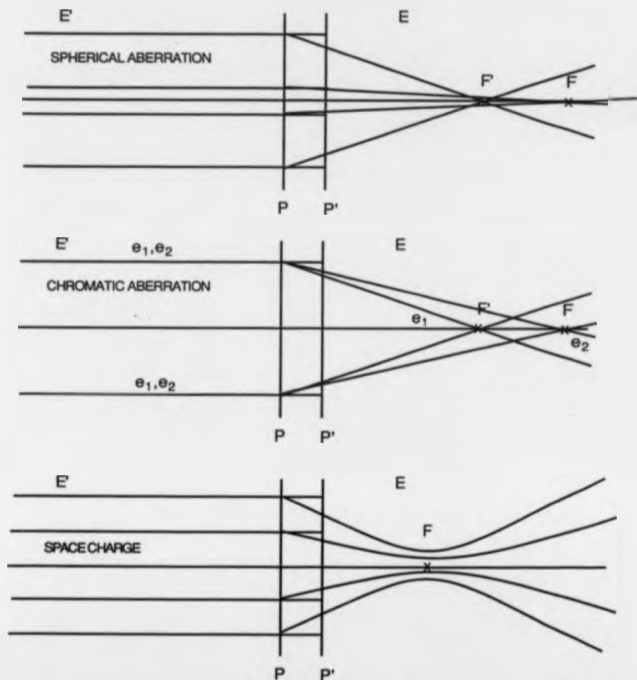


FIGURE 3.3: RAY DIAGRAMS TO ILLUSTRATE THE EXAGGERATED EFFECTS OF SPACE CHARGE, SPHERICAL ABERRATION AND CHROMATIC ABERRATION.

the potential distribution from cylindrical rods closely approximates that of the hyperbolic asymptote.

The electric field can be derived by differentiating the potential distribution with respect to the orthogonal cartesian set x, y, z :

[50]

$$E_x = - \frac{d\phi}{dx} = - [U + V \cos(\omega t)] \frac{x}{r_0^2}$$

[51]

$$E_y = - \frac{d\phi}{dy} = - [U + V \cos(\omega t)] \frac{y}{r_0^2}$$

[52]

$$E_z = - \frac{d\phi}{dz} = 0$$

The equations of motion for a charged particle in these fields can be obtained by considering the restoring force of a charged particle at a point.

[53]

$$F = eE$$

F = Restoring force, e = Electronic charge, E = Electric field gradient.

Now writing the force as $F = ma$ or in the standard differential form:

[54]

$$F = m \frac{d^2 s}{dt^2}$$

F = Restoring force, m = Mass of the particle, s = A distance along x or y .

t = Time.

Then three equations can be obtained, one for each independent axis:

[55]

$$\frac{d^2 x}{dt^2} + [U + V \cos(\omega t)] \frac{ex}{mr_0^2} = 0$$

[56]

$$\frac{d^2 y}{dt^2} - [U + V \cos(\omega t)] \frac{ey}{mr_0^2} = 0$$

[57]

$$\frac{d^2 z}{dt^2} = 0$$

Symbols as described above.

These are the first order equations of motion of a particle of mass to charge ratio m/e under the influence of the modulated field. The first order approximation is only accurate for paraxial trajectories. The form of these equations can be identified with that of the Mathieu canonical equations, by the substitution of U and V for dimensionless quantities a and q ; and t for ξ :

[58]

$$a = \frac{4eU}{m\omega^2 r_0^2}, \quad q = \frac{2eV}{m\omega^2 r_0^2}, \quad \xi = \frac{t}{2}$$

[59]

$$\frac{d^2 s}{d\xi^2} + [a_s + 2q_s \cos 2\xi] s = 0$$

a, q, ξ - reduced variables in the canonical Mathieu equation, $s = x$ or y ; $m, \omega,$

r_0, e, U and V have been described in the text previously. *NA: if s=y then the first "+" sign is "-" in [59]*

The Mathieu and Newtonian equations provide a useful insight into the operation of the quadrupole. A single plot in axq space shows the four stability

regions. Most mass filters use the first stability region. A plot of this region in $U:V$ space shows the effect of mass and the filter operation in detail. Figure 3.4.

In the first part of figure 3.4 the full u,q stability plot is shown with a portion of this plot (region one) expanded. Trajectories satisfying the condition for stability in both x and y directions are enclosed within the triangular section. Mass separation is shown in the second part of figure 3.4. A scan line of constant gradient is used to intersect the stability region close to the apex. The closer to the apex this line becomes, the lower the number of transmitted ions becomes. This is complemented by an increased resolution.

The negative rod of the quadrupole mass filter acts a high-mass band-pass filter. Ions which respond too slowly to the modulated restoring force of V will collide with the negative rod and become neutralised. Similarly, a simultaneous low-mass band-pass filter is operative in the other transverse plane. The light ions are neutralised on the positive rod because they respond too rapidly to the changing potential. The operation described is the effect on positive ions and is reversed for negative ions. The filter can be made to have variable resolution by changing the intercept of the scan line with the stability region close to the apex. The QMF is an *in line mass spectrometer* (provided that unit mass resolution can at least be obtained).

The trajectories of ions in the perfect quadrupole are either oscillatory and stable, or oscillatory and exponential. Typical applied potentials for a *region one* QMF operating at 2MHz are linear. In this study, scan lines are described between $V = 0-1000V$ peak-to-peak and $U = 0.53-74.1V$. These values are significantly different to those quoted from the manufacturer¹⁸¹.

Real quadrupoles

The three main differences between real and ideal QMF's are: the *fringing fields* at the entrance and at the exit of the filter; imperfections in the quadrupole geometry; and the potential distribution a long distance from the axis. These differences cause a number of deleterious effects on the performance of the

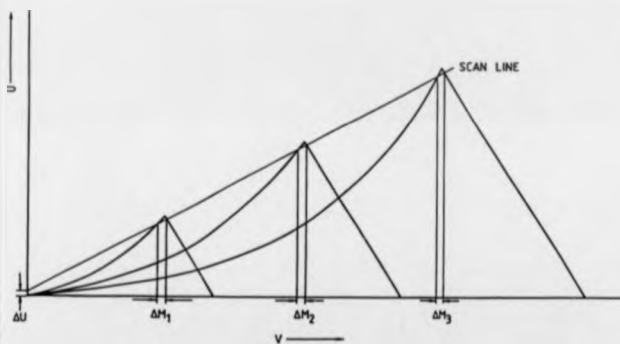
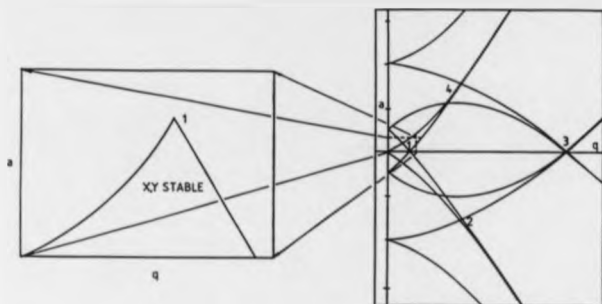


FIGURE 3.4: DIAGRAM TO SHOW THE STABILITY REGIONS IN AN OPERATING QUADRUPOLE MASS FILTER

quadrupole. The fringing field is a time dependent effect caused by the quadrupole having a finite length.

A quadrupole of a finite length has a maximum to the injection energy along the axis for effective mass separation. The resolution of the quadrupole depends on the number of cycles of the modulated field experienced. Some inherently unstable trajectories will be passed by the filter if the number of cycles of RF modulation is less than the half life of the trajectory concerned. The transmission of the quadrupole, toward stable trajectories, is not isotropic for ions of different masses at the same energy ¹⁸².

Much of the work done on the effects of these imperfections relates to the acceptance characteristics of the filter with a certain length of fringing field ^{179,183}. A plot of the acceptance of the quadrupole in *phase space* shows an ellipse of increasing eccentricity with increasing the applied voltage or the length of the fringing field. The effect of twisted, warped or misaligned rods has also been addressed ¹⁷⁹.

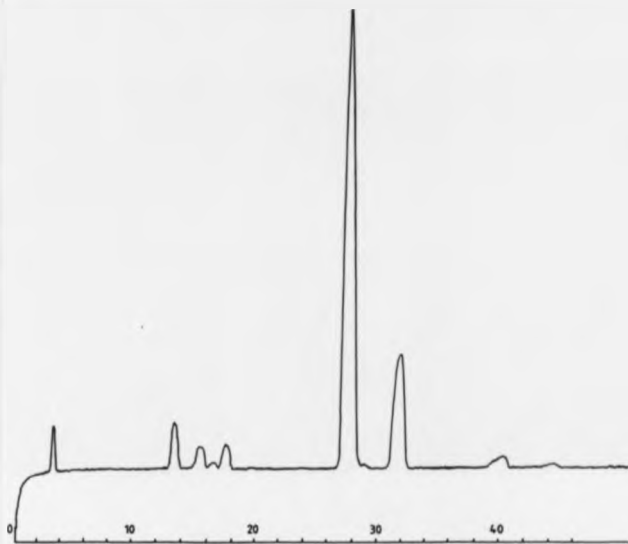
To combat the problems of fringing fields of the quadrupole, several methods have been applied. Brubaker proposed the application of a delayed AC or DC ramps ¹⁸⁴, by the use of a prequadrupole or Brubaker lens. A second device, which is a ceramic leaky dielectric, can be inserted into the quadrupole to filter out the RF potential in the region of the fringing field ¹⁸⁵.

The question of the effect of the QMF on the translational energy of mass filtered particles has not been recognised in chemical applications to the knowledge of the author, although the use of RF fields in particle accelerators is quite routine ¹⁸⁶. The performance of the crossed beam instrument in the present study is limited by this little considered effect.

Performance, observations, results and discussion

The performance of the ion optics, as indicated by the condition of the ion beam, is illustrated by figures 3.5-3.9. The remaining part of this chapter is concerned with specific ion optic problems. It is structured in sections, and an attempt has been made to find a natural, logical progression through these sections. Consider the mass spectra in figures 3.5-3.7. These spectra were recorded on several different precursor species. Unit mass resolution can be obtained for each QMF driver. The primary ion beam also gave low stability, moderate reproducibility, large angular divergence (eg. figure 3.8), small ion currents and broad energy spreads (eg. figure 3.9) using configuration A (see figure 2.6A). In addition to these five general effects there were three specific observations which would not occur if the ion optics were operating as intended. Firstly, electrons could be detected on the final collimating aperture of the ion beam source. This effect can be seen clearly in figures 3.5-3.7. Secondly, a large positive ion flux could be collected under certain conditions when the source was switched to a negative ion mode. Thirdly, the integral ion energy spectrum often showed a maximum in the spectrum, greater than zero volts. The latter result implies that for an ion beam of constant composition, more ions exist with energy greater than eV , than exist with energy greater than 0. These three additional effects seem paradoxical at first sight. These observations made it obvious that a detailed understanding of the ion optics was required.

During the first two years of this project, all the changes to the configuration of the apparatus were made on semi-empirical judgements. Some progress was made in eliminating some of the problems. A lack of proper data storage facilities in the early stages of the work, meant that judgements on the value of data were necessary at the instant of their collection. Due to the number of times that specific investigations had to be repeated, this method proved to be a false economy of time.



A spectrum of a mixture of air and helium. Note the unit resolution indicated by the presence of the 29 and 17 peaks of air. Note also the large negative-ion signal caused by electrons penetrating into the quadrupole. This occurs despite the presence of He^+ (mass 4). This spectrum was collected using an electrometer on the exit collimating aperture using configuration A (figure 2.8A).

FIGURE 3.5: MASS SPECTRUM OF AIR/He

These spectra used to check the satisfactory operation of the source quadrupole. The samples were H_2 , He, air, and air. These spectra were recorded using configuration A (figure 2.6A).

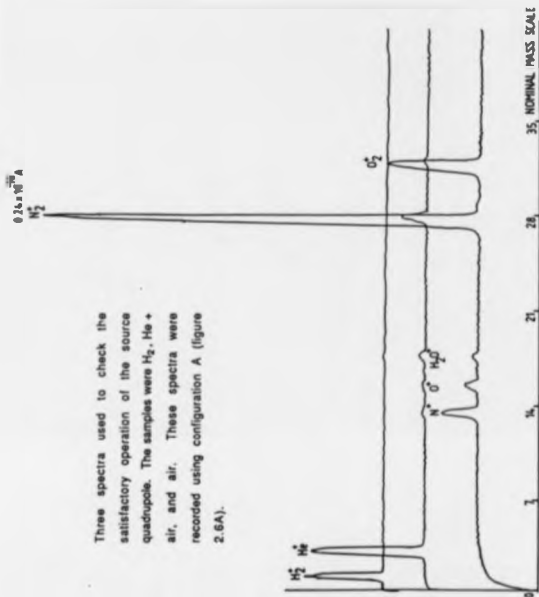
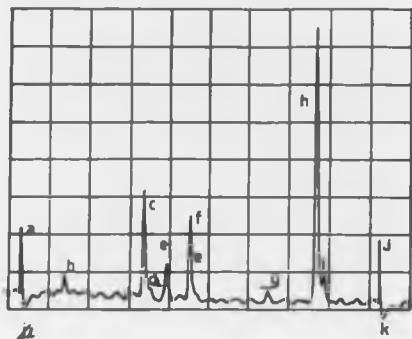


FIGURE 3.6: MASS SPECTRA RECORDED OF AIR/He AND H₂



A mass spectrum of CS_2^+ and fragment ions. This spectrum was recorded using the DSA 524A digital oscilloscope adapter in roll mode. The data was recorded in 4092 words. a, j - 8y-back pick up indicating the start and the end of the spectrum. b - C^+ , c - $^{32}\text{S}^+$, d - $^{33}\text{S}^+$, e - CS_2^{++} , f - C^{32}S^+ , g - $^{32}\text{S}_2^+$, h - $\text{C}^{32}\text{S}_2^+$, i - $\text{C}^{32}\text{S}_2^{34}\text{S}^+$, k, j - electron current.

FIGURE 3.7: MASS SPECTRUM OF CS_2

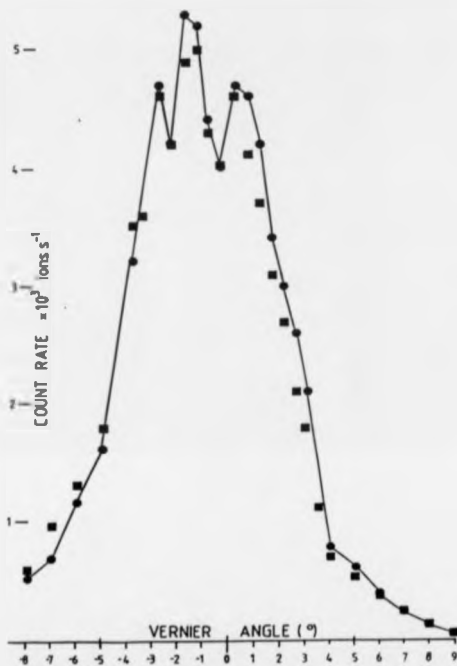
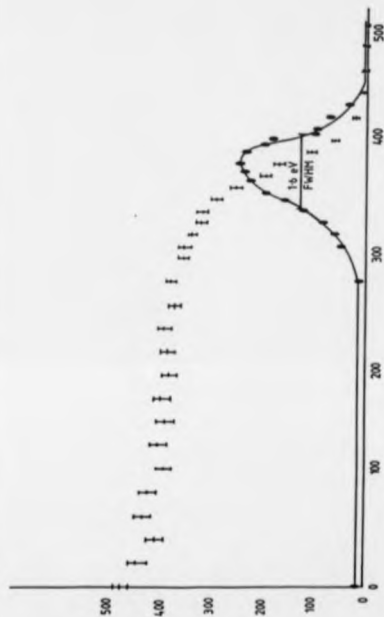


FIGURE 3.8: ANGULAR PROFILE SHOWING POOR COLLIMATION AND THE SPHERICAL ABERRATION



An energy profile of CS_2^* . This was the best energy resolution obtainable at the time that the spectrum was recorded.

FIGURE 3.9: CS_2^* ENERGY PROFILE

In addition it was not possible to interpret data retrospectively in the light of new insight or knowledge.

Discussion of the separate problems and effects is made in the following sections:

Stability and reproducibility

Ion source and modelling of the ion source

Ion energy

The retarding potential difference analyser

Evidence for scattering

Recommendations

Conclusion and summary

Stability and reproducibility

An experiment was made to check the stability of the mass filter and source. A mass selected ion beam was set up with the octopole and exit assembly removed and monitored over a period of 48 hours. The ion flux varied within the approximate expectation of $\pm\sqrt{x}$ (x = count rate). These results were compared with those obtained by replacing the octopole and exit assembly.

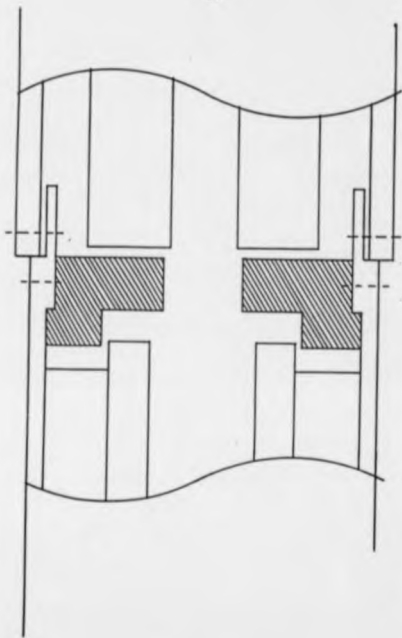
Rewiring the octopole was found to improve the stability. The octopole is a stigmator (a lens to correct for the 3rd order effect of astigmatism) for the highly astigmatic flux exiting the QMF. Figure 2.6a shows the connections used by Kelly. Variations in the supply voltages are not axisymmetric and lead to a wandering maximum in the ion beam. The connections drawn in figure 2.6a may have been used previously to correct for the physical misalignment of the source 100. By reconnecting as figure 2.6c, variations in the electric field lead to axisymmetric changes in focussing properties. Using the wiring drawn in figure 2.6b the ion beam can be maintained along its axis; small variations lead to less dramatic changes in the optical properties. The beam can also be directed at over a small vertical range, assisting beam intersection during a crossing experiment.

A temperature drift in the initialising stages of the source and mass filter supplies was observed. The equipment should be switched on for about thirty minutes to allow the electronics to reach optimum operating temperature. Some retuning was necessary after this period.

Two further effects contributing to poor reproducibility were noted. In implementing the new QMF no account had been taken to match the dimensions of the octopole support, as a result the lens is a very loose fit. The new quadrupole rods are shorter than the old rods leading to a gap of 7.90 mm between the octopole and the quadrupoles. The coupling of these two fields causes a time dependent potential distribution. The time of flight of a rectilinear trajectory of a 6 eV ion of mass 28 across that gap is 1.2 μ s. This time is equivalent to 2.4 periods of RF modulation. A top hat shaped electrode was placed in to the gap to decouple the fields (figure 3.10). Following the introduction of this decoupling collar an improvement in the operation of the octopole was noticed. A single, reliable optimum value of the focussing potentials applied to the octopole was observed for each ion energy, where previously there had been several.

To prevent surface charging, a single layer of colloidal graphite (Aquadag) was applied to the electrode in the source exposed to the ion beam. The exit plates assembly was constructed with the aid of dowels to ensure that the plates were concentrically aligned. Since these measures were introduced, the stability and reproducibility of the ion beam has not normally been a problem.

Once good stability was introduced, it was possible to assess the effects of the multitude of other instrumental conditions. Using a data sheet to record all the experimental conditions day to day reproducibility was dramatically improved. This can be demonstrated by reproducing the data to within experimental error simply by dialing up the recorded conditions.



SCALE: X5

FIGURE 3.10: A DIAGRAM SHOWING THE DECOUPLING COLLAR IN THE GAP BETWEEN THE QUADRUPOLE AND OCTOPOLE

Electrons in the quadrupole

The construction of the ion source ^{the pattern of} and ion burns caused by normal operation are drawn in figure 3.11. The ion beam precursor gas diffuses into a volume inside a photoetched grid anode. Ionisation occurs when electrons, formed by thermionic emission from a hot tungsten cathode, collide with the ion beam precursor. Ions are extracted by field penetration from the ion source.

Electrons were detected at the final collimating electrode of the beam source for focus voltages up to ca. 110% of the electron energy. This can be seen in the figures 3.5-3.7. The electron current collected was roughly proportional to the electron emission in the source ¹⁸⁹. The electron current maximised when the focus voltage was equal to the electron energy. It was also found empirically that the best ion energies were obtained for only small differences between the electron energy and the focus potential. In the cases of $EE = F$ and $EE = F$ the ion flux was diminished. For $F > EE$ the largest ion fluxes are observed. For example at -31 eV no ions are detected when the electron energy falls below -27 eV. If V is raised with EE fixed at 27 eV then the ion flux decreases. In all cases the measured distribution of energies was large, but minimised with maximum ion flux.

A model of the ion source was made in order to rationalise these observations. An electrode set was constructed from a array of 130×63 points using SIMION 3.0. The mirror image facility expands this array to double size. This program does not allow for 3D modelling and has the best accuracy for planar simple electrodes aligned parallel to the axis along which the ions are transported. The source is assumed to be a cylindrically symmetric potential array. In this way the electrons will only move in planes intersecting the axis of the potential array. Space charge is assumed not to be significant.

Six of the output trajectory profiles are shown in figures 3.12-3.14. Figures 3.12b and 3.14b are examples of simulations in which electrons start at the filament with zero energy. These results explain the ion burn patterns observed in the source (figure 3.11).

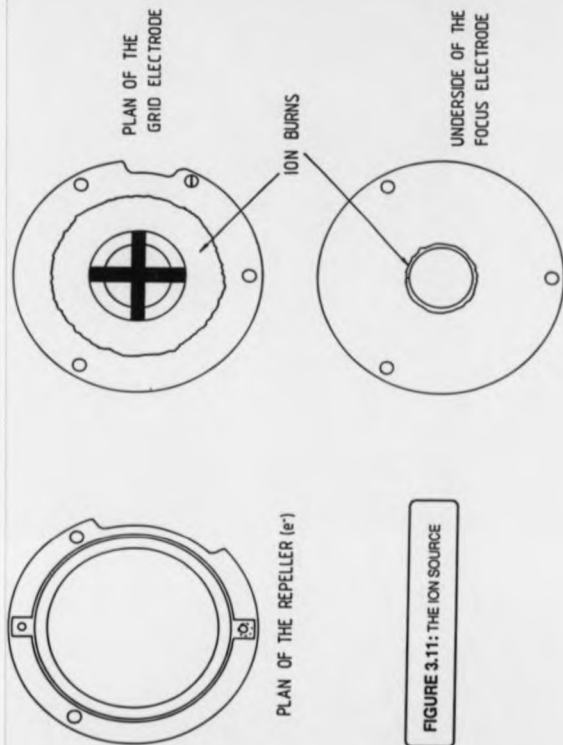
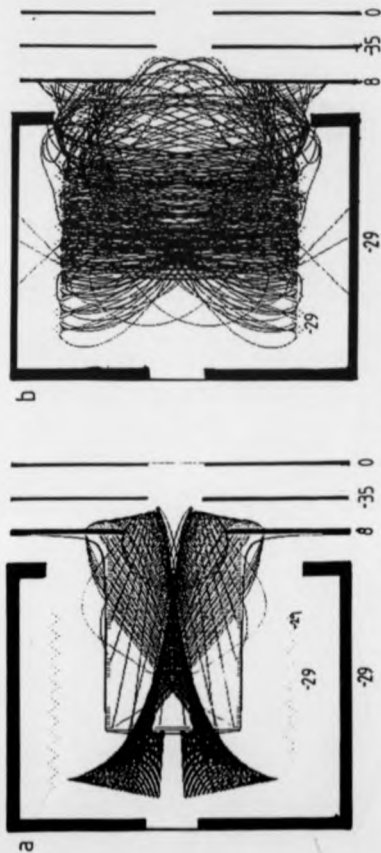
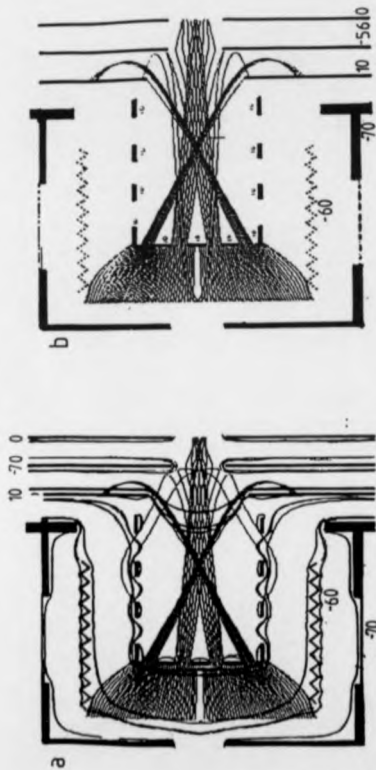


FIGURE 3.11: THE ION SOURCE



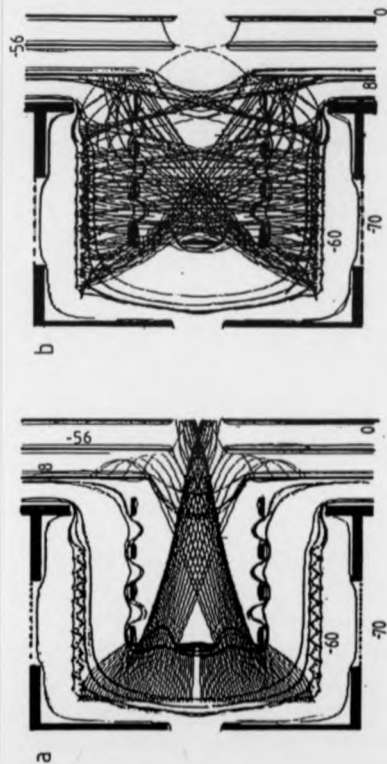
Simulated ion trajectories in the model ion source electrode structure. The electrodes were raised to the voltages that are shown in the diagram.

FIGURE 3.12: PLOTS OF ELECTRON TRAJECTORIES OVER A SIMULATED ELECTRODE ARRAY FOR MODELLING THE OPERATION OF THE ION SOURCE.



Simulated ion trajectories in the model ion source electrode structure. The electrodes were raised to the voltages that are shown on the electrodes. Note the number of electron trajectories focussed into the quadrupole entrance is not diminished by raising the focus plate to the electron energy (repeller voltage).

FIGURE 3.13: PLOTS OF ELECTRON TRAJECTORIES OVER A SIMULATED ELECTRODE ARRAY FOR MODELLING THE OPERATION OF THE ION SOURCE. SHOWING THE FOCUSING OF ELECTRONS INTO THE QMF ENTRANCE PLATE



Electron trajectories calculated over a modified version of the electrode structure in figures 3.12 and 3.14. The results are similar to those of figures 3.12 and 3.14. This indicates that the qualitative effects observed are not chance results associated with a particular rigid electrode structure.

FIGURE 3.14; PLOTS OF ELECTRON TRAJECTORIES OVER A SIMULATED ELECTRODE ARRAY FOR MODELLING THE OPERATION OF THE ION SOURCE.

Figure 3.13a, 3.13b and 3.14a show that trajectories can penetrate the entrance of the quadrupole from starting points away from the filament. These arrays have different grid structures, but the effect is little changed and this result is qualitatively significant. Note particularly that the number of trajectories entering the quadrupole is not changed by an increase in the focus voltage from -56 to -70 eV (the magnitude of the electron energy). A further increase in the ratio; focus : electron energy, causes the focus electrode to reflect all the incident electron trajectories (figure 3.12a).

The trajectories of the electrons penetrating the quadrupole are stable with respect to the number of iterations per grid point. The model fails to quantitatively simulate the ~~the~~ experimental result of electrons penetrating the quadrupole, when electrons are started at the filament with zero energy. Some important qualitative results are noted. The use of a grid with a coarse mesh allows significant field penetration and loss of ions formed close to the perimeter of the grid. The electrons started at arbitrary points in space can be seen to focus efficiently into the quadrupole. The number of trajectories passing into the quadrupole is not diminished by an increase in focus potential, instead they are focussed down to a more paraxial beam.

Note that the actual trajectories that are plotted in this study are of limited use. The actual potential is highly anisotropic and complication due to space charge from mA electron emission ~~are~~^{is} expected to be large. The stability of the various trajectories with respect to an increase in the number of iterations per grid point gives a qualitative indication of the error. Those simulated trajectories, which model the real trajectories well are highly stable with respect to an increase in number of iterations per grid point used. The trajectories which make many crossings of the source and are trapped for long times have poor stability with respect to an increase in the number of iterations.

At an energy of 70 eV, electrons travel the length of the quadrupole (100 mm) in 2×10^{-8} s. This value is only a fraction (1/100) of the period of modulated

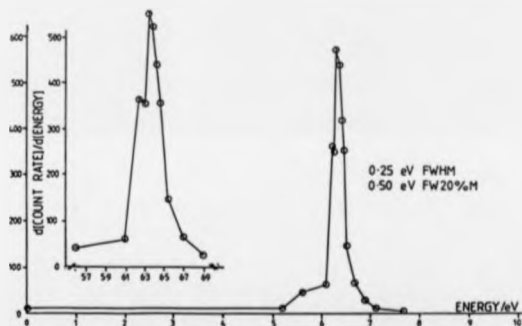
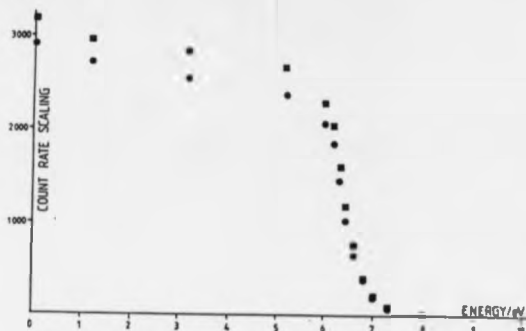
field of the quadrupole. In this frame of reference the quadrupole mass filter is apparently only an electrostatic lens to the electron. Thus, unstable electron trajectories can be transmitted even for large electric field gradients. An electron current is not detected on the final collimating electrode when a large ion current of low mass is simultaneously observed. This is illustrated by figure 3.8. In such a case the net beam current only is measured. Thus, no useful measurement is obtained on either charged particle. Electrons might cause unwanted reactions if they were present at the crossing region during an experiment. Ions could also be formed from neutral gases in the quadrupole. These ions would have the phase corrected energy of the field at the point of formation.

Modifications were proposed on the basis of these qualitative results. The top of the grid was blocked off to prevent electrons entering the quadrupole. To reduce the lateral field penetration the grid was covered in a fine wire mesh. This would be expected to increase ion flux and also reduce the tendency of ions to dive towards the grid mounting plate, which acts as the electron trap in this source.

Ion energy

The ion energy spread in the primary beam was unacceptably broad. Figure 3.9 is one such example. Figure 3.15 was recorded after routine maintenance. The differences in FWHM of the recorded ion energy is dramatic (1.8-0.25 eV), but the difference in the configurations used to record them is only minor.

There are several possible explanations for the apparent energy change. The RPD only analyses energy in a direction that is orthogonal to the plane containing the RPD, i.e. the direction of transport of the beam (z). The component of velocity of an ion in the z direction gives rise to an apparent vector energy quantity (E_z). This important parameter is related in energy (E), according to the relation $E_z = E \cos \theta$, where θ is the angle subtended between the particle trajectory and the z axis. A 6 eV ion, for example, would just be transmitted by a 5 V ramp if the angle of incidence was 33° . This explanation has been eliminated because θ for the required energy



Integral and differentiated-integral ion energy spectra for all components of air. Note the form of part A of this plot and compare the result with figure 3.21. This result indicates, over a small mass range at least, that the spread in ion energy is not caused by mass discrimination effects at the detector.

FIGURE 3.15: ION ENERGY PROFILES INDICATING THE IMPROVEMENT OF RESOLUTION OBTAINED WHEN THE OMF IS EARTHED.

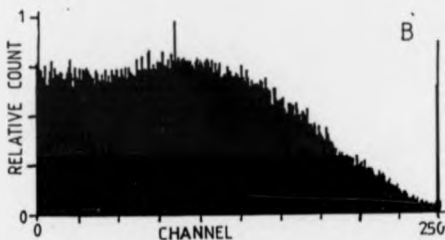
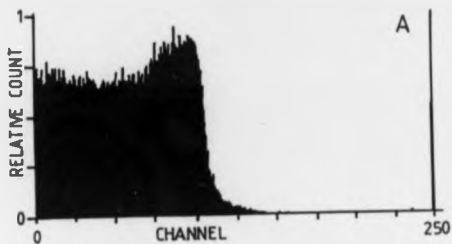
deficit and the angular acceptance of the quadrupole, estimated by trigonometry to be 3.5° , are different by an order of magnitude.

Further information is provided in figure 3.16. Including an RF only quadrupole can broaden the ion energy substantially. Figure 3.17 shows that the ion energy resolution can be improved by recessing the ion source from the quadrupole and mass selecting. It can be inferred from this data that the RF broadens the energy distribution directly.

One explanation is that the RF electric field penetrates into the ion source to the point of ion formation. When a mesh is placed across the quadrupole entrance plate, the effect persists. The quadrupole act as a transmitter, *broadcasting* RF electromagnetic radiation. This *airborne* RF, of 2 MHz frequency, should not pass through the source plate hole. If, however, the pick up of stray RF on the grid was large, then a time dependent spreading of ion energies would result.

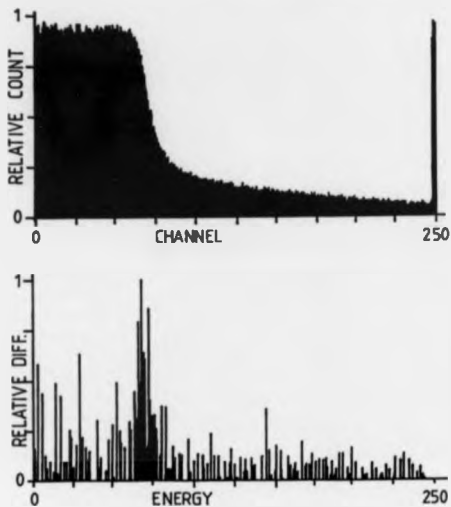
The 2 MHz noise on the source electrodes was measured in a test performed in atmospheric conditions. The maximum amplitude of the noise was 50 mV. The conditions of the plasma generation source would be different due to differences in the permittivity of air and a plasma. Repeating the measurement with the source operating, changes this value to ≤ 80 mV peak to peak. These changes are not of the correct order of magnitude to cause the experimental result alone.

To understand the effect, the basic considerations of ion formation must be restated. The potential energy of a particle with charge e in an electric field is independent of its mass. The difference, ΔV , between the electric potential at the point of formation and the point of interest gives the ion energy by the product $e\Delta V$ independent of the intermediate energies (cf Hess' law) ¹⁹⁰. This holds providing that the trajectory is smooth and continuous over a smooth, continuous potential. Exceptions to this or methods by which an ion can change its energy are discontinuous eg. by a collision with a third body or the spontaneous conversion of translational energy into another form of energy.



The integral ion energy spectra in this figure differ only in that the source quadrupole is earthed in case A and in case B is connected and running in the total ion or RF only mode.

FIGURE 3.16: ION ENERGY PROFILES FOR STANDARD CONDITIONS WITH AND WITHOUT A RF ONLY OMF.



The effect of recessing the ion source from the operating source quadrupole. The integral ion energy spectrum becomes more sharply pronounced. There is also a long tail off into the high energy channels.

FIGURE 3.17: ION ENERGY PROFILES FOR Cs^+ WITH THE SOURCE RECESSED FROM THE OMF.

The observations on the ion energy are consistent with the explanation that the quadrupole causes a discontinuity in the linear acceleration (see figure 3.18). The first order quadrupole equation:

[52]

$$E_z = - \frac{d\phi}{dz} = 0$$

Symbols defined previously.

implies that this does not happen. In the fringing field, however, the ion is ^(retarded) accelerated into the enclosed volume of the quadrupole where the approximation becomes good, then the ion is ^{accelerated or} retarded on exiting the quadrupole. The amount of energy imparted to an ensemble of particles is zero on average, and the energy of a particular ion depends on the phase and position of entry and exit of the field.

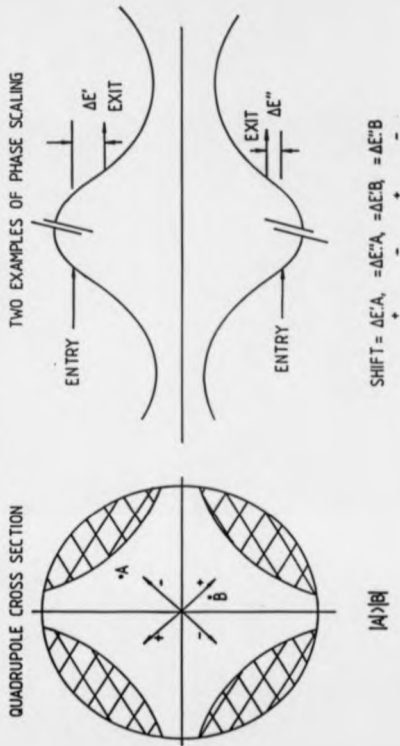
NB. The latter sentence may not be true if, for instance, discrimination between trajectories occurs.

The effect of the RPD

Once it was established that the ion source gave a near monochromatic ion beam, it was possible to investigate the effect of the RPD analyser. Figure 3.19 shows the measured integral ion energy profiles from a series of similar experiments which produced unexpected results. The form of the spectrum was the first surprise. All of these spectra should be identical and to within experimental error a step function of energy. The second surprise was the gross effects caused by some small changes in conditions. The cause of the changes in appearance of profiles E to F, and H to I are changes in applied potential of just -3V. The spectra show several features. A plateau from 0-1.5 eV rising to a peak at between 1.5-2.0 eV. The fall off to the base line is a gentle slope with a hint of a shoulder at 3-4 eV. At a first sight the ion energy appears to be of a broad spread.

The retarding potential difference analyser is constructed from three thin electrodes with wire mesh spot welded over the aperture. The operation of such a system is expected to introduce plane contours, perpendicular to the path of ^{the} ion.

FIGURE 3.18: DIAGRAM TO SHOW HOW THE A RF MODULATED FIELD CAN INDUCE CHANGES IN ION ENERGY



Ions entering the quadrupole at A or B become accelerated or retarded according to time spent in the fringing field and the phase of the alternating radio frequency voltage. Either case also occurs in the exit fringing field, leading to four scenarios, increasing the distribution of energies in the beam.

10 profiles recorded under the same basic conditions. In each case the slight change in conditions should not promote a change in the form of the profile. In each case the profile should be a near perfect step function, if the RPD energy analyser is working as specified.

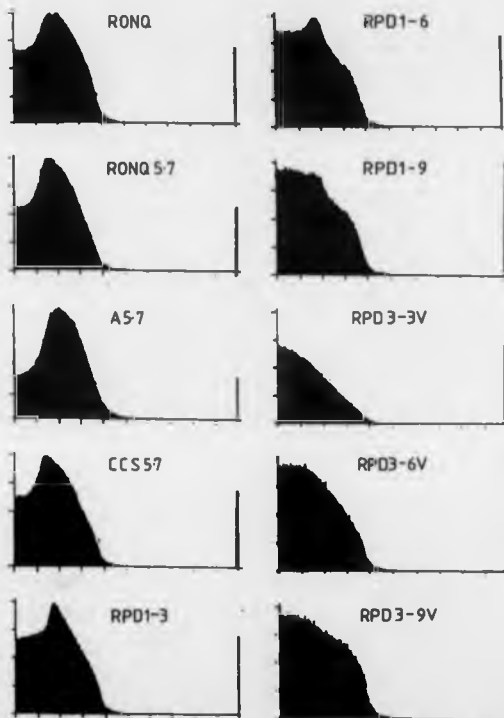


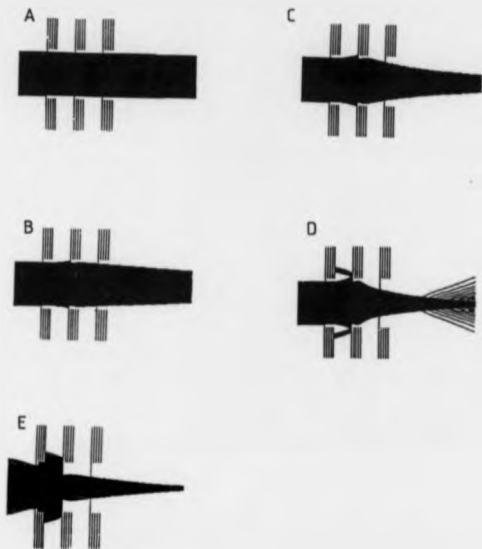
FIGURE 3.19: A SERIES OF EXPERIMENTAL RESULTS EXPOSING A SYSTEMATIC ERROR IN THE RPD ANALYSER

The transmission of such a system is independent of voltage, up to the voltage at which the energy resulting from the component of velocity in the direction of the analyser (E_z) becomes less than the barrier. A closer look at the construction of the RPD analyser shows that the electrodes have a slight top hat shape. A possible explanation for the results is some sort of focussing effect. This suggestion may appear at first sight oversimplified, due to the apparent structure in the spectra (possibly indicating multiple effects). This focussing effect proposed can be shown to be consistent with the data by modelling.

A model of the electrode structure was made in a 77×37 SIMION 3.0 array. The array was refined to 0.0005 V accuracy. The fast adjust option was used to alter the potentials on the array. Trajectories were calculated using fifty iterations per grid point. High stability of trajectories to a change in the number of iterations per grid point was obtained.

143 trajectories, initially parallel to the axis and of a single energy were run over a variable potential barrier. A total of fifteen runs were recorded. The SIMION program was not large or versatile enough to model the exact array. A functional computer program was written to extrapolate the final coordinates and angle of exit from output data produced in the system *dialog*. The *dialog* file is the computer record, in SIMION, which records all input from the keyboard and output to the VDU. The computer program allows independent variation of two probe parameters. The parameters are the distance (XA) to a field stop aperture and the diameter (YA) of that aperture. The distances are measured in grid units, which can be used to scale the array. In this study $3GU = 1 \text{ mm}$. Figure 3.20 shows the plotted trajectories of five of the fifteen runs made. Each one, in the absence of focussing, should look like profile A. As the voltage on the central electrode is increased a strong focussing effect does occur.

The model represents the ideal monochromatic experiment in the absence of space charge effects. To test the first-order operation of the model an orifice of 14.01 GU was placed at axial distances of $XA = 40$ and 750 GU . The results are



5 examples of the model electrode structure and ion trajectories. In each case the central electrode is raised to a positive potential whilst the remaining two electrodes are raised to earth potential. Under ideal operation, of the RPD analyser, each of these trajectory plots should resemble case A. Case D shows the spherical aberration clearly. Case E shows an extreme example of the iris effect.

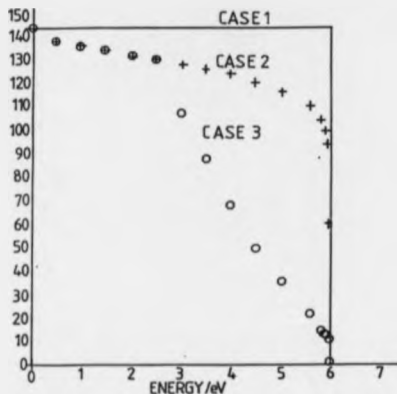
FIGURE 3.20: SIMION PLOTS OF 143 ION TRAJECTORIES OVER A SIMULATED RPD ELECTRODE ARRAY

plotted in figure (3.21). Curve 1 represents the ideal result expected, that is all of the 143 incident trajectories being transmitted. Curve 2 represents the case for $XA = 40$ GU, where all the ions passing through the analyser are collected. Curve 3 is the effect at 750 GU (25 cm).

The model indicates that the lens does not act ideally, even under ideal conditions, which would normally be expected to yield perfect behaviour. Ions are lost because the lens acts like the iris controlling the pupil in an eye: this can be seen in figure 3.20. As the voltage on the central electrode is increased the effective aperture of the lens is reduced: notice the similarity of curve 2 to figure 3.15. Curve 3 follows the same pattern of behaviour up to 2.5 eV, when there is a sharp deviation and more trajectories than expected are lost. The reason for this behaviour is the lensing action induced by the shape of the electrodes. The lens is highly spherically aberrated and the different shorter foci of the marginal trajectories gives rise to the deviation the curve 3 in the figure. Altering the value of XA varies the position of the knuckle in curve 3.

Varying the second parameter, the orifice size YA , leads to a maximum in the plot. Figure 3.22 shows curves for three values of YA (1.51, 3.01 and 6.01 GU) at an axial distance $XA = 150$ GU. The position of the maximum is moved forward as the aperture is reduced. The peak also becomes sharper and more pronounced as XA is reduced.

This model appears to be very flexible and can be used to fit actual data. Figure 3.23 has four simulated plots of the fifteen runs varying XA over a fixed YA . Figure 3.24 shows three plots. One of these is processed data from an archived plot (RONQ5.7-1/3/89), and the other two are simulations. YA is fixed to model the first point and XA is varied around realistic values to match the experimental results. The simulation results are scaled to the ion energy of the experimental results. In the absence of post acceleration this does not affect the actual foci, only the ratio of ion energy to barrier height changes the focus.



Testing the performance of the modelling results. The three plots indicate the different appearance of the same data.

Case 1 represents the expected form of the plot of an ideal ion beam over the RPD.

Case 2 represents the actual form of the plot of an ideal ion beam over the RPD.

Case 3 represents the same data with $XA = 750$ GU, $YA = 14.01$ GU.

FIGURE 3.21: PERFORMANCE PLOTS FOR THE RPD MODEL

Three plots simulating the extreme selectivity towards ions at different central electrode voltages (y axis).

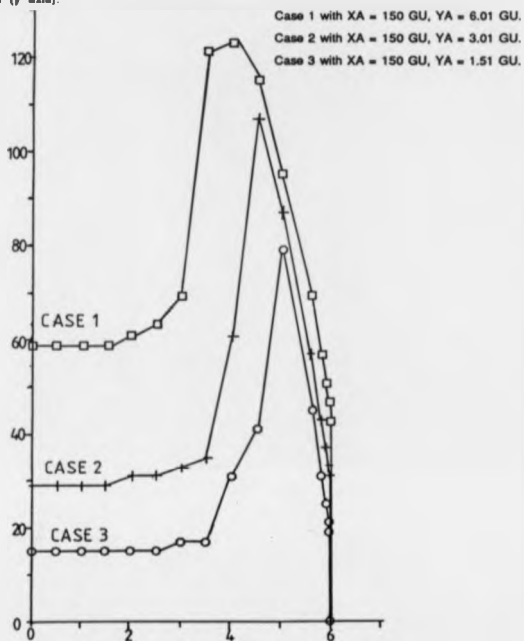
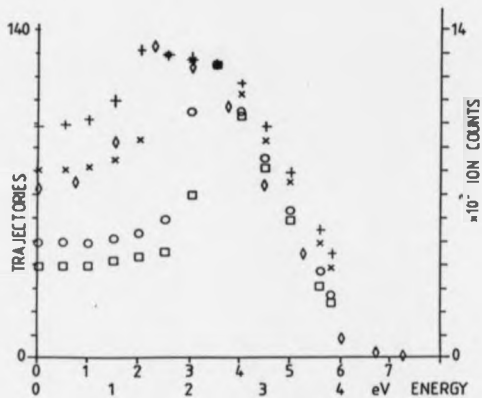


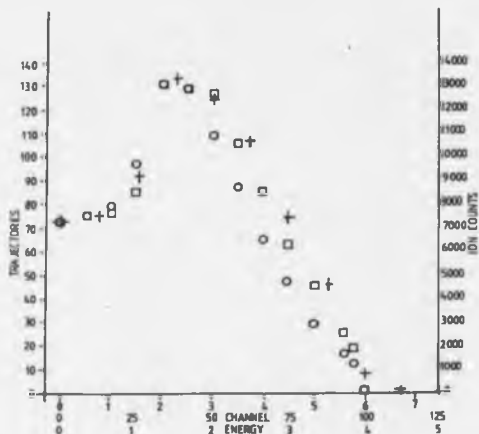
FIGURE 3.22: PERFORMANCE PLOTS FOR THE RPD MODEL



Preliminary modelling plots using the XA value

- ◇ Case A - actual data: from the archive RONGS.7 - 1/3/89
- + Case B - with XA = 242 GU, YA = 10.01 GU.
- × Case C - with XA = 242 GU, YA = 8.01 GU.
- Case D - with XA = 242 GU, YA = 4.01 GU.
- Case E - with XA = 242 GU, YA = 5.01 GU.

FIGURE 3.23: FITTING PLOTS USING THE RPD MODEL



Modelling plots which have been fit to the actual data by choosing YA to give the correct starting point.

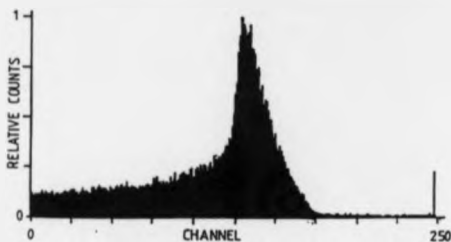
- ◆ Case A - actual data; from the archive RONOS.7 - 1/3/89
- Case B - with $XA = 533$ GU, $YA = 7.81$ GU.
- Case C - with $XA = 400$ GU, $YA = 7.81$ GU.

FIGURE 3.24: FITTING PLOTS USING THE RPD MODEL

The chromatic and spherical aberrations can be individually tested in the model. The spherical aberration is particularly large; this is caused by a deviation from ideally shaped parabolic contours.

Similar observations to those described here were noted by Jarrold and Kelly when operating the RPD analyser. The conditions in their experiments are unclear. Jarrold attributes the effect to trajectories which are offset by some angle with respect to the axis normal to the RPD analyser (this would occur if the centre around which the detector rotates was not the crossing region or reaction zone) and to space charge limiting behaviour. Following the derivation of the Langmuir-Child equation for the space charge limit of ions in a quasi 1 dimensional diode, however, it can be seen that Jarrold's values are overestimated by a factor of (M_e/M_i) . The source of this error is an incorrect substitution of a kinetic energy term for a potential energy term into the equation as quoted by Jones¹⁸⁷. The actual space charge limit for the RPD analyser is in the order of 10^{-8} A and not 10^{-9} A, for a charged particle of velocity 6.5 km s^{-1} (eg. a singly charged particle of mass 28 at 6 eV). It is possible that the bottle neck for the space charge limit is actually the quadrupole. Kelly and Jarrold both use the pole bias of the quadrupole to eliminate undesirable effects in the peak profiles. This empirical modification of the experimental conditions works (figure 3.25) and can be rationalised from the modelling of the detector. Negative pole bias extends the compound focus of the detector. This is equivalent to changing XA in the model. ~~When the RF QMF is on, XA is reduced. If the QMF is mass selecting, the profile takes on the effect of varying YA. The profile ends that of the variable pupil also result.~~ ~~Changing -- RF quadrupole maps~~ (normally) The effect of this modification on energies which are expected to be missing from an analysis of the primary ion beam is undetermined. These energies would be present in reactions leading to a partitioning of translational energy away from the prior kinetic energy of the ion. No beams composing of mixed ion energies have been modelled. The chromatic aberration ~~is not compensated by this modification of experimental parameters.~~ (s. changing pole bias)

When a RF only quadrupole is included in the line of sight arrangement at the detector some of the focussing effect of the RPD is removed. Trajectories are



The most extreme discrimination that was ever recorded for the archive of energy spectra. This is caused by the RPD analyser focussing the ions close to the ion energy on to a very small detector quadrupole entrance acceptance area. Note the similarity to plots contained in figure 3.22

FIGURE 3.25: DATA SHOWING THE POWER OF RESOLUTION AND POLE BIAS IN MASKING DETECTOR ABERRATIONS

randomised by the oscillations in the RF field. If the quadrupole is operated as a mass filter then the effect can persist, if there is strong focussing on to the acceptance plane of the quadrupole. This is equivalent to reducing both XA and YA in the model. Each section of the energy profile, up to the point of strong focussing on to the acceptance plane, is isotropic. Then a strong focussing leads to a sharp peak as the number of ions entering the quadrupole is increased. Compare figure 3.22 to 3.25 and figure 3.26b which is less dramatically affected.

Performance of the ion beam

The best ion energy profiles obtained have FWHM between 0.16 and 0.12 eV. Since the cause of unacceptable energy resolution was intrinsic in the quadrupole, an experiment was conceived to test if the beams intersect; the most basic experiment. Using a precursor gas of argon (purity > 99%) and ionising it under low pressure conditions below the threshold for Ar^{2+} formation must lead to a great excess of Ar^+ ions. Following such a procedure removes some of the need for mass selection in the primary beam.

Evidence of scattering in two body crossing experiments

Figure 3.27 shows the profiles of two beams with the neutral beam turned on and off. A beam of Ar^+ , without mass selection, was crossed with a beam of neutral Ar atoms effusing from a capillary array. This experiment offers some evidence that the beams intersect because the primary ion signal was attenuated. The horizontal angular profile shows a narrow maximum, which shifts slightly in position. The count rate at wide angles is increased relative to the experiment with the beam off. There is also a change in the appearance of the integral ion energy spectrum, for the beam on and beam off experiments. The shape of the plot can be rationalised on the basis of the previous discussion of the optical behaviour of the detector. There does not, however, appear to be a broad CT peak in line with the capillary array. The

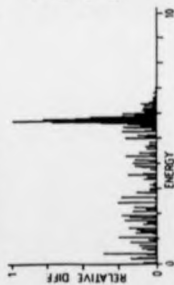
SMOOTHED Q1-7/3/89



EARTHED Q1-7/3/89

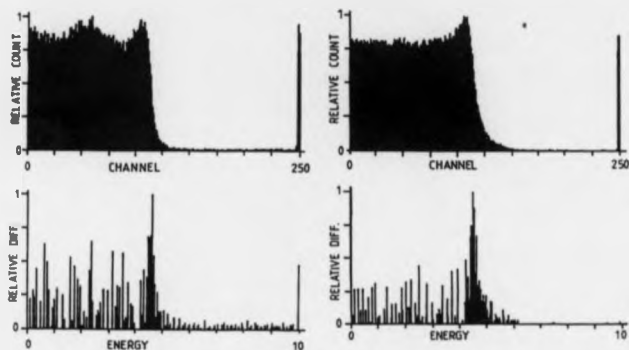


C



The figure shows integral ion energy profiles. A and B are identical in all respects except that the detector quadrupole is mass selecting with a small pole bias (<3.5 V) in case A. In case B the detector quadrupole is earthed. These results were recorded with Ar as test gas.

FIGURE 3.26: INTEGRAL ION ENERGY PROFILE SHOWING THE EXTREME SELECTIVITY TOWARDS MASS SELECTED IONS POSSIBLE



Data supporting the interaction of the beams ? See text for a further discussion.

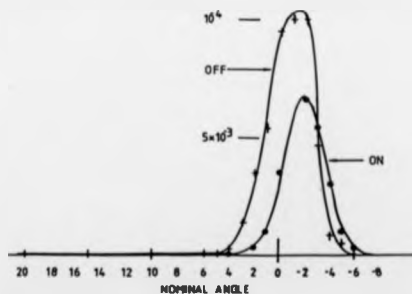


FIGURE 3.27: ANGULAR AND ENERGETIC DATA: EVIDENCE FOR A LOW NUMBER OF ION-MOLECULE COLLISIONS?

mechanical movement used in angular measurements is impaired by the physical length of the RF leads connected to the detector QMF, which makes the latter determination difficult to perform. These leads cannot be lengthened, because the RF generator units must be balanced, that is that the stray capacitance of the leads must be charged in a time less than a quarter of the period of the RF modulation.

Recommendations

Detector modifications

The effect of the chromatic and spherical aberrations can be reduced by the inclusion of aperture stops on the exit of the RPD analyser. This would reduce the transmission, but keep the trajectories paraxial and improve angular resolution. A Brubaker lens could be mounted as close to the exit of the RPD analyser as possible, and in front of the QMF. The addition of this RF-only short quadrupole would have two positive effects. These effects are a reduction in XA and an increase in the area of the entrance plane of the whole system. The ions arriving at the QMF are already *phase locked* and the acceptance efficiency of the quadrupole is also improved.

The only other long term solution is to redesign the RPD analyser. The curvature of the field at the edge of the lens can be reduced by beveling the rear of the electrodes. To delay the effect of iris formation, the voltages applied to the electrodes in the analyser can be ganged. That is they can be scanned in constant voltage difference to keep the principal focus of the lens constant or in constant ratio reducing some of the chromatic effects.

Ion beam source modifications

Modifications are suggested to improve the operation of the ion beam source. The first modification should be replacement of the ion source. A conventional ion source has several advantages over the Bayard-Alpert type used in this study. The use of magnets and an electron trap reduces the volume of the ion formation element.

Hence, larger field gradients can be used to extract the ions, without increasing the intrinsic source energy spread above an acceptable level. The use of an electron trapping plate would eliminate the possibility of electrons entering the quadrupole. This modification would free the focus voltage and electron energy from their mutual interdependence. An ionisation efficiency investigation could be carried out with confidence of reproducibility. One disadvantage of changing the source over is a certain reduction in the number of ions formed by the source per torr of reagent gas. This does not necessarily mean that the primary ion signal would be reduced. If the ionisation is more selective or the injection more efficient and increased signal could be obtained.

A number of low quality experiments are possible using a quadrupole in the ion beam source. Modifications which would improve the behaviour of the ion optics are inclusion of a Brubaker lens and the use of aperture stops. The transmission of ions into the mass filter would be improved by the inclusion of a Brubaker lens as before. The aperture stops are placed before the Brubaker lens and after the quadrupole. The ions injected into the quadrupole are then made paraxial and the change in ion energy in the fringing fields are minimised. Stopping down the exit also reduces the transmission of electrons or unstable trajectories far off axis. Thus, the observed ion energy would have a narrower distribution about the true energy of formation. As a lens, the quadrupole mass filter is severely spherically aberrated. Stopping the exit and the entrance down reduces this aberration.

Following an improvement in ion energy and collimation, the beam should be easier to bring to a single focus. The final collimating electrode in the ion beam generator can be used as an angle defining aperture and should be earthed. The divergence can be improved at the expense of ion flux. Care should be taken to avoid the effects of residual spherical and chromatic aberrations when using an angle defining stop. Under some conditions wings on the angular plot can be detected as a direct result of these aberrations (see figure 3.8).

This apparatus is only capable of producing moderate quality results, if it works at its best, after these modifications are carried out. An ion beam generator including a quadrupole and no further energy selection cannot be used to perform experiments at the resolution required. More intense beams with more controllable ion optic characteristics can be formed using electrostatic and magnetostatic sectors. This instrument could be modified to incorporate a Wien filter. Any other possibilities are prohibited by the physical size and configuration of the instrument. A more versatile vacuum reaction chamber would have demountable sources so that new innovations could be included as modifications without the problems of space or size constraints.

Conclusions

In order to make any experiment possible for which data can be collected and interpreted with any confidence, the ion optic problems of an instrument must be understood. Although this appears to be standard practice in the leading laboratories, when building or modifying apparatus, no such study has been made for this crossed beam instrument. A systematic study of some of the ion optic properties of this apparatus was seen to be necessary, following the collection of some empirically unreasonable data and the observation poor day-to-day reproducibility. Some subtle changes in experimental conditions caused gross changes in observed data where a slight effect was expected. Difficulty was also experienced in reproducing the results of previous researchers to within experimental error, especially given the limited data on experimental conditions recorded in their note books.

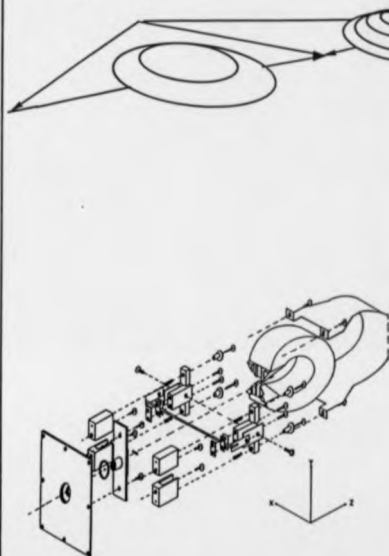
The investigation has produced a better understanding of the ion optic character of the apparatus and explains the experimental results. This formal study has taken up much of the time of this project, but has provided a firm base of understanding for the evaluation of experimental data and modification required before experiments can be performed.

A large body of data has been collected in order to perform this investigation. This collection would have taken a prohibitively long time without considerable streamlining of experimental practice. Several functional computer programs have been written to expedite the transfer and processing of data.

The principal conclusion of this chapter are:

1. The detector is severely affected by aberrations. These have been successfully modeled and the experimental results have been interpreted in terms of these. The space charge error has been ruled out as a cause of the experimental results.
2. The ion source gives rise to stray electrons which can be detected along the ion flight path.
3. The quadrupole mass filter changes the energies of ions entering into it. The suitability of the quadrupole mass filter in a source for crossed beam experiments has been discussed in light of this effect.
4. Several major modifications must be made to the ion optics before this instrument can work.

4



NEUTRAL BEAM

Introduction gas dynamics

Kantrowitz and Gray¹⁹¹ drew attention to many of the benefits of supersonic expansion molecular beam sources, over effusive and oven beam sources, in a seminal theory paper in 1951. They predicted an increase in intensity and a decrease in the velocity spread. These enhancements are of significant advantage to the study of reaction dynamics. The predictions of Kantrowitz and Gray were partially verified in experimental investigations¹⁹²; the enhancements observed were not as marked as the expectation, due to the unforeseen counter productive effects of skimmer interactions. Thus, the most significant tool, until the advent of the laser, for the study of the dynamics of elementary chemical reactions was created. A large volume of publications on the subject of supersonic beams has appeared in the literature, concerning both theoretical detail and experimental data. The transport and gas dynamics of the supersonic expansion are considered to be well understood, but many of the formulae are approximations to analytical solutions which do not exist. Several books are available which describe background and the important equations from that work 193-195.

A continuous supersonic expansion requires an enormous pumping speed (as much as $100,000 \text{ l s}^{-1}$), to remove molecules from the under expanded portion of the beam. Hagena¹⁹⁷ proposed in 1964 that the pumping speed requirements could be reduced, whilst retaining the advantages of the supersonic expansion, by pulsing the aperture of the nozzle. The modulated or pulsed beam has further popularised the use of supersonic expansion beam sources in chemical dynamics. A wide variety of design of pulsed valves have been published¹⁹⁷⁻²⁰⁴. These beam sources are complicated significantly by the mechanisms of the shutter. Considerable effort has been made in making reliable valves with long working lives and with a wide range of applications. There are many engineering problems associated with the manufacture of a pulsed beam source. Thus, a greater demand is made on the skills of the experimenter in constructing a pulsed beam than a continuous beam source. The types of materials

which give rise to stability at elevated temperatures are hard and refractory. Those which are able to give good vacuum seals do not have high temperature stability. These examples indicate the compromises that are required in the construction of a pulsed molecular beam. ^{Source} This increase in complexity affects the performance and the appeal of pulsed beam sources.

The compromises that are made in constructing a modulated beam source, and the changes that have to be made to incorporate an effective aperture and shutter, affect the flow characteristics of the valve. The pulse of gas is only equivalent to a small portion of a continuous supersonic beam in principle. In practice, even the ideal limit of its operation does not fulfil this notion. The limit to the minimum pulse time for formation of a supersonic jet has been analysed ^{207,208} in the model an ideal shutter function was assumed for the valve, and the sudden-freeze approximation was applied to characterise the expanding jet. It was concluded that for some of the beam to reach supersonic flow, a lower limit to the minimum pulse width of ca. 10 μ s should be imposed in the design criteria for new sources. The fastest reported pulse to date is 7 μ s FWHM ²⁰⁸. Gentry notes that measured pulse widths less than this are clearly possible, but that the calculation of minimum pulse width is correct probably to within half an order of magnitude. Apart from experimental performance data, the minimum time studies outlined above, and a suggestion that the beam source acts like a biased harmonic oscillator ^{198,209}, no attempt has been made to rationalise the real time evolution of the pulse beam envelope.

In this chapter details of the design, development, evaluation and performance data for a pulsed valve are given with the specific aim of installing it in a crossed ion-neutral beam apparatus. The harmonic oscillator model of Gentry and Glese is extended to provide a simple framework for the evaluation of the beam evolution.

Overview of pulsed beam sources

There is a wide variety of design for pulsed molecular beam sources 198-205

These work on three underlying principles: the piezoelectric effect, magnetic attraction and the electromotive effect. The first valves were based on fuel injectors modified from the commercial valves available from the automobile industry. The modified fuel injector type and some other types of reliable valves have been constructed around solenoid mechanisms. These valves typically contain a sprung ferritic plunger, which forms the valve shutter and is disturbed from the valve seat by a transient magnetic field. The magnetic field is formed by pulsing the solenoid coil, into which the plunger is attracted, with an energising current pulse. The coil of the solenoid has a high inductance which precludes ultrafast ($<100\mu\text{s}$) operation. In the piezoelectric type valves, motion is induced when a voltage is applied to a piezoelectric crystal. Both the piezoelectric and solenoid type valves can be latched open without power dissipation problems. Thus, these valves have continuously variable duty factors.

The fastest reported gas pulse was recorded using the Gentry and Gliese design of electromotive valve 198. In this valve, the driving force to open the valve's sprung shutter is generated between two parallel, closely spaced conductors carrying counterflowing currents. This valve requires an enormous power (2.3 kA, 1.2 kV-current pulse) and dissipation of heat generated during the operation is a problem: the valve must be supplied with cooling water. An alternative use of the electromotive effect is in the simple *Flemming's motor*. Motion is induced, according to the Fleming left hand motor rule, into a conductor carrying a current in the presence of a perpendicular magnetic field. This design differs from that of Gentry and Gliese in that the transient magnetic field of one of the conductors is replaced by a permanent magnetic field. In this way the power requirement of the valve is reduced (now directly proportional to current (I) not I^2 as previously). The performance of the valve is maintained, and the problem of cooling water supply is replaced by problems

arising from a residual magnetic field. The valve types, discussed above, are compared in table 4.1.

An interesting method for reducing the effective pulse length of valves with slow acting shutters, has been demonstrated by Bassi *et al*²⁰³. The expansion is quenched in the first chamber of differential pumping, by the scattering induced by molecules reflected from the collimating aperture. The attenuation of the molecules in the background in this chamber is so severe, that a sharp pulse much shorter than the open time of the valve is observed, followed by a long tail off. This clever modification of the pulse time does not, however, reduce the pumping requirements of the system since the quantity of discharged gas is the same. Thus, the pump-out time constant is not reduced.

Elements of Gas dynamics

The elements described below are applicable to steady state gas dynamics. The introduction given here is quite terse. A more lengthy discussion can be found in Miller²¹⁷ if this is required.

Continuum Fluid

In gas dynamics it is most convenient to consider that matter is uniformly dispersed throughout the space it occupies in a continuum, and the expanding jet as a steady-state flow system. The large number of molecules, in even small quantities of gas at moderate pressure, ensures that the mean-free path is short and the expected number of collisions in unit time is large, justifying the continuum approximation. Treatment of the beam as a continuum has a number of advantages. Many of the properties of the beam, for example, can be obtained from a thermodynamic treatment^{195,196} greatly simplifying the analysis. The thermodynamic description of the expansion offers a potential for confusion in that the internal energy of the ensemble provides the energy for the expansion and not the energy contained within the internal

TABLE 4.1: Comparison of four valve types

VALVE TYPE	PIEZOELECTRIC	SOLINOID	COUNTERFLOWING CURRENT	FUSING MOTOR
DRIVING FORCE	THE CHANGE OF SHAPE OF A CRYSTAL WITH APPLIED VOLTAGE	MAGNETIC ATTRACTION OF A FERRITIC PLUNGER	ELECTROMAGNETIC REPULSION INDUCED INTO CONDUCTORS CARRYING OPPOSING CURRENTS	ELECTROMAGNETIC INDUCTION BY A CONDUCTOR CARRYING A CURRENT IN A MAGNETIC FIELD
PULSE LENGTH	78 μ s - CONTINUOUS	100 μ s - CONTINUOUS	7 - 40 μ s	17 - 48 μ s
NOZZLE SIZE	0.1 - 1 mm	VARIABLE	VARIABLE	VARIABLE
DUTY FACTOR	CONTINUOUSLY VARIABLE	CONTINUOUSLY VARIABLE	< 1%	< 1%
MAXIMUM OPERATING FREQUENCY	780 Hz	250 Hz	10 Hz	120 Hz
MAXIMUM OPERATING TEMPERATURE	ARALDITE LIMIT = 100 °C		COOLANT LIMIT 100 °C FOR WATER	VITON LIMIT = 200 °C
REQUIRED CONNECTIONS	1 x 75 Ω - GAS	2 x 50 Ω - GAS	2 x 50 Ω - GAS + COOLING WATER	2 x 50 Ω - GAS
TERMINAL MACH NUMBER	10 - 11			8 - 9
PULSE SHAPE	FLAT TOPPED TRIANGULAR	FLAT TOPPED	TRIANGULAR	TRIANGULAR
SET UP	PRESSURISED H ₂ OR TEST RIG	PRESSURISED H ₂ OR TEST RIG	TEST RIG	TEST RIG (CRITICAL)
STAGNATION PRESSURE RANGE	400 torr - 10 atm	\leq 100 atm	2 atm	200 torr - 1 atm
REPRODUCIBILITY	\pm 10 %		\pm 10 %	\pm 8 %
SOME ADVANTAGES	NO STRAY FIELDS COMMERCIAL VALVE	COMMERCIAL VALVE, RELIABLE	COMMERCIAL VALVE, SMALL CONSTRUCTION FAST PULSES	FAST PULSES
SOME DISADVANTAGES	NON CORROSIVE GASES ONLY NEGATIVE TEMPERATURE DEPENDENCE OF μ INCOMPLETE OPENING OF THE SHUTTER SOUNDING	STRAY MAGNETIC FIELD SOLINOID HIGH INDUCTANCE OF THE SOLINOID	SOUNDING HIGH POWER REPAIRS FREQUENT 2-3 MYA max REPAIRS FREQUENT COOLING STRAY RF	STRAY RF AND MAGNETIC FIELDS DIFFICULTY IN CONSTRUCTING THEM NON CORROSIVE GASES

modes of individual particles. The actual mechanism of the expansion is molecular in nature. The velocities of particles in the beam become aligned following thousands of two-body collisions. The translational-translational energy transfer and rotational-translational energy transfer are efficient and the populations of energy states contained in these modes change significantly during the expansion. The rotational temperature, as measured in the microwave spectra of supersonic beams, can reach temperatures lower than 1K. This can be shown by comparing the recorded spectra and the calculated spectra for the test substance at the relevant temperature. The translational temperature also relaxes, but is relatively hot. The equivalent measure of temperature in this case is that of a Maxwell distribution function giving rise to an equivalent energy spread. The translational temperature, therefore, reflects the alignment of velocities. Electronic and vibrational modes are normally inefficiently relaxed in collision and can survive for many thousands of collisions, as a result the energy content in these modes is usually unchanged.

Continuum steady flow mass rate

The mass flow rate of a first converging and then diverging nozzle (Laval nozzle) can be calculated for the assumptions of a continuum fluid. The minimum area of the nozzle can be used in the equation:

[60]

$$\dot{m} = P_0 A^* \left[\frac{\gamma W}{RT_0} \left\{ \frac{2}{\gamma+1} \right\}^{\frac{\gamma+1}{\gamma-1}} \right]^{\frac{1}{2}}$$

\dot{m} = mass flow rate, P_0 = stagnation pressure, A^* = minimum area of the throat,
 γ = ratio of heat capacities, R = gas constant, T_0 = stagnation temperature,
 W = molecular mass of the substance.

This equation strictly applies to a Laval type nozzle of the geometry described above. The mass flow rate is preferable to the molar flow rate because it is constant even if

clustering occurs. The expansion is assumed to occur adiabatically and that the value of γ for any particular case holds constant throughout the temperature range considered. In the cases of O_2 , N_2 and air the vibrational mode is inactive at room temperature. Expansion from a gas with a stagnation temperature much higher requires that this mode be taken into account.

Terminal velocity of the beam

The terminal velocity of the beam can be calculated from the continuum flow equation 217:

[61]

$$v_{\infty} = \left[\frac{2RT_0 \gamma}{W(\gamma-1)} \right]^{\frac{1}{2}}$$

v_{∞} = terminal velocity of the gas, R = gas constant, T_0 = stagnation temperature, γ = ratio of heat capacities, W = molecular weight.

For example, oxygen expanding from an ambient stagnation temperature: $v_{\infty} = 730$ m s⁻¹. The terminal properties of the beam are reached quite rapidly within a few nozzle diameters of the exit of the source. Using a second equation based on the Mach number (the local speed of sound), the velocity at different points in the expansion can be calculated from a back fit to the equation 217:

[62]

$$v = M \left\{ \frac{RT_0 \gamma}{W(\gamma-1)} \right\}^{\frac{1}{2}} \left\{ 1 + \frac{\gamma-1}{2} M^2 \right\}^{-\frac{1}{2}}$$


v = velocity at some defined point, M = Mach number, R = gas constant, T_0 = stagnation temperature (the temperature of the gas if it is brought to rest adiabatically), γ = ratio of specific heats.

Putting $M = 10$ the velocity of oxygen is $v = 712.4 \text{ m s}^{-1}$. This value is $\approx 97\%$ of the terminal velocity (730 m s^{-1} , see above) of the expansion.

Molecular properties must be considered in the analysis of continuous flow gas expansions where the continuum approximation breaks down. The thermodynamic description assumes the expansion is both adiabatic and isentropic. The heat capacities, which control the state functions S and H of the beam, may not be constant for large changes in temperature ($\approx 300 \text{ K}$). There are other problems too. The beam diverges and the density of the quasi-continuum is reduced. Thus, the mean-free path increases until the molecules of the beam effectively cease to collide. In addition, three or more body collisions can give rise to nucleation: this is not accounted for in the continuum model. Condensation produces side effects which further reduce the applicability of the continuum model eg. latent heat is released into the beam, the molecular number density is reduced, a disparate mass mixture is produced etc.

Heavy molecules in gas mixtures, such as clusters in a bath of the monomer units are known to undergo a velocity slip ²¹⁸, presumably due to the greater inertia (cf. Brownian motion). The velocity slip has been used to separate isotopic uranium in flow systems ²¹⁹. This system has advantages, ie. the technology is simpler and the separation is more efficient than the gas centrifuge technique ²¹⁵.

Hagena derived a scaling law for the rates of formation of clusters within beams. He obtained a dependence on stagnation pressure, orifice diameter and the stagnation temperature ²¹¹. The result is useful in the choice of experimental configuration to promote or reduce the population of clusters in experiments. A whole area of study of clustered species in the gas phase has been made possible using jets. The formation of clusters is, however, disadvantageous in experiments requiring fast pulses of monomer units.

Figure 4.1 shows a  section of a sonic nozzle-beam expanding as a free jet. There is a complex shock structure formed by a rotated intercepting shock wave called the barrel shock. Inside this volume the gas becomes supersonic, then it becomes over expanded and is shocked back to subsonic velocities on passing through the Mach disc.

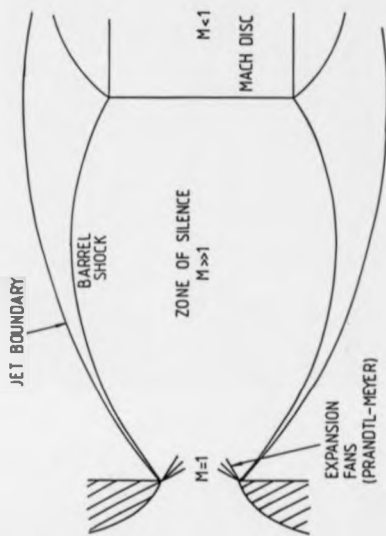


FIGURE 4.1: A CROSS SECTION FROM A SONIC NOZZLE GIVING RISE TO A FREE JET EXPANSION

These shock waves form the mechanism by which information is propagated within the beam. By this mechanism, molecules can adjust to meet the down stream conditions even though they are travelling at their own (sonic) *event horizon* i.e. faster than information, in the form of sound waves, can be transmitted to them. The position of the Mach disc can be calculated in the dimensionless parameter x_d/d as a function of P_0 (the stagnation pressure) and the background pressure, P_b :

[63]

$$\frac{x_m}{d} = \frac{2}{3} \left\{ \frac{P_0}{P_b} \right\}^{\frac{1}{2}}$$

x_m = the position of the Mach disc, d = the nozzle throat diameter, P_0 = stagnation pressure (the pressure of the static gas in the gas reservoir), P_b = background pressure in the chamber into which the gas expands.

This continuum result is very sensitive to the background pressure. For example, for a continuous valve operating at $P_0 = 1$ atm and $P_b = 10^{-4}$ atm, the theoretical position of the Mach disc is $x_d/d = 2120$. The background pressure in the first chamber of differential pumping is quite high in a *Campagne type source*²¹³. In this type of source, a weak shock structure has been observed and the position of the Mach disc is of the order of $x_d/d = 30$. The optimum position for the skimmer in this type of source is ^{located} observed in front of the Mach disc and several nozzle diameters from the source exit. In free jet sources pumped by diffusion pumps, the background pressure is maintained at a much lower pressure. The beam is skimmed a long distance from the theoretical position of the Mach disc, in the *zone of silence*. In this region the beam is dense and travelling supersonically. These properties are maintained if the skimmer does not seriously disrupt the gas flow.

Skimmers

The effect of skimmers on the gas flow has been discussed in detail ²¹⁰. A skimmer can cause a reduction in intensity, a reduction in average velocity and an increase in the velocity spread. Shock waves formed on the bow of an obstacle, such as a skimmer, disrupts the flow more if the obstacle is blunt. The gas is forced to expand around the object in the manner of an aerofoil. The angle (θ) around which the gas moves is given by the Prandtl-Meyer equation ¹⁹⁸:

[64]

$$\theta = \left\{ \frac{\gamma+1}{\gamma-1} \right\}^{\frac{1}{2}} \tan^{-1} \left[\left\{ \frac{\gamma-1}{\gamma+1} M^2 - 1 \right\} \right]^{\frac{1}{2}} - \sec^{-1} M$$

γ = ratio of heat capacities, M = Mach number, θ = expansion angle.

There are approximate methods for solving for the so called flow properties (eg. the velocity at an instant) which account for the molecular properties of the beam. The method of characteristics and sudden freeze methods are two. In the former case the properties are calculated along orderly, Laminar flow lines or streamlines, by an iterative method. In the sudden freeze model the expansion is considered to be interrupted at a hemispherical locus called the quiting surface at some specified distance from the orifice. The non-isentropic character is approximated as happening suddenly at this surface. The surface represents a singular disruption between two regions of continuous calculable flows and is said to be the boundary between the continuum and molecular fluids. For the purpose of calculations, the skimmer can be taken to be the maximum distance at which the quiting surface can occur. The skimmer has the effect of selecting a part of the beam. Thus, the thermodynamic *universe* is divided and the continuum theory does not hold. The expansion is then quenched by the skimmer. This is exactly the function of the notional quiting surface described above.

The pulsed beam

The pulsed beam construction is given in appendix 2, in sufficient detail for a replica to be made. A photograph of the assembled valve is shown in plate 2. This photograph is accompanied by figure 4.2, which shows the valve in an exploded form.

The valve base was constructed on a flange so that it could be loaded into the front of a pressure box. The pressure box is shown in plate 3, and the relevant construction drawings are included in appendix 2.

The following section describes the development of this design from the point at which a prototype valve had been chosen. The reasons for changing the design of various components is discussed briefly. The logic for the progression of the chapter is:

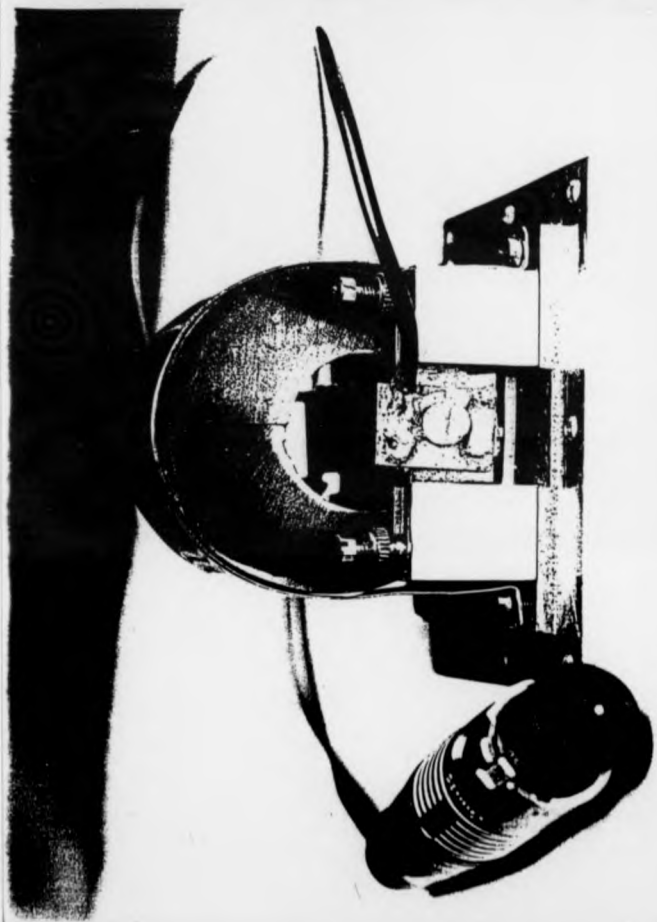
1. to set out the design criteria
2. to explain why these ^{criteria} were not met by the prototype
3. to discuss the performance of the design (included in appendix 2).

Considerations on incorporating the beam into the main apparatus

Mechanical considerations

In fitting the pulsed beam into the main apparatus several mechanical constraints and specifications had to be met:

- 1 The pulsed valve had to be supported rigidly.
- 2 There had to be a wide range of adjustment, sufficient to ensure that the beam could be aligned with the crossing centre.
- 3 The adjustment had to be easy to make *in situ*.
- 4 The dimensions of the pressurised stagnation chamber had to be minimised to maximise the size of the ducts through which the background gas is expelled.



JRTRAINOR 1/11/87
PULSED MOLECULAR BEAM SOURCE

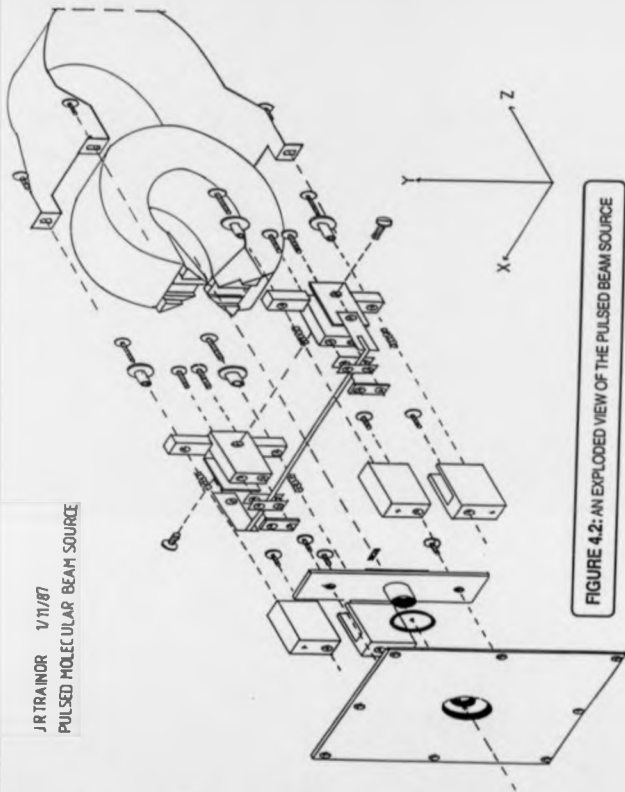


FIGURE 4.2: AN EXPLODED VIEW OF THE PULSED BEAM SOURCE

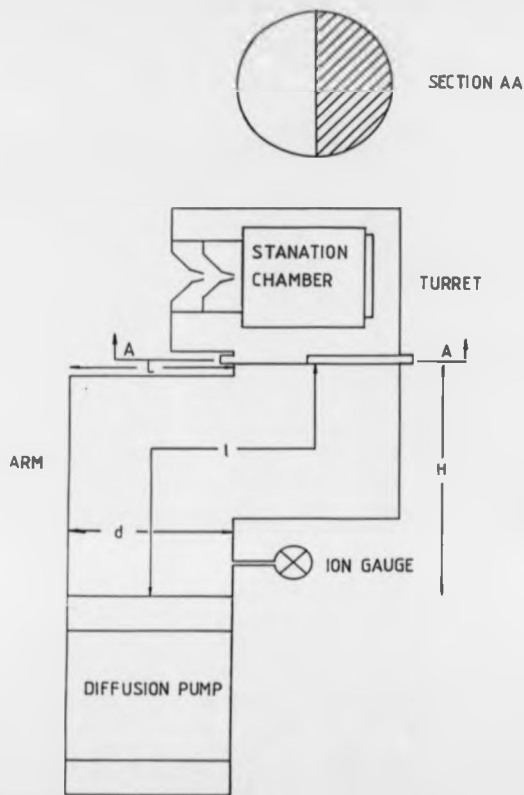
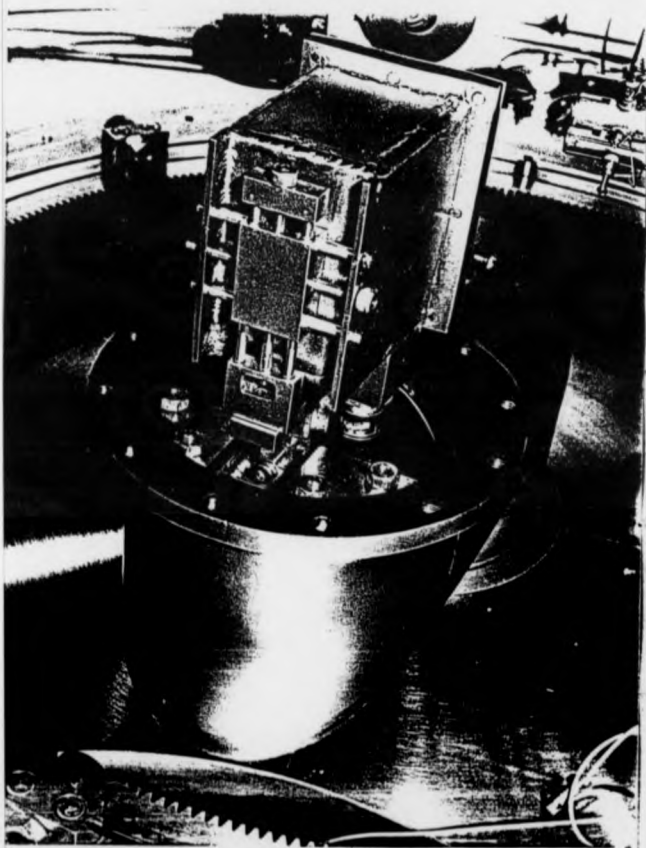


FIGURE 4.3: A DIAGRAM TO REPRESENT THE NEUTRAL-BEAM DIFFERENTIALLY PUMPED VACUUM CHAMBER



- 5 The valve had to be easy to load into the stagnation pressure chamber, without affecting the critical set up made on the remote vacuum test cell.

The mount for the adjustment was built on a flat base bolted on to a support at the top of the neutral beam chamber arm. Slackening the four securing bolts allows a yaw adjustment in the meridional plane of $\pm 15^\circ$. The pressure box is demountable from a worm and pinion gear which provides a pitch adjustment of $\pm 5^\circ$ (azimuthal plane). This adjuster is shown in plate 3 with the stagnation chamber. (plate-B, a diagram is also included in appendix 2. The pressure can be suspended from a rear mounting translator allowing displacement along X,Y coordinates of ± 5 mm and ± 10 mm respectively. Adjustments can be made *in situ* using an Allen key. The turret was constructed from three portions (the design sheets are included in appendix 2). The front piece is used to mount the skimmers assembly. The bottom section is loaded first and the valve is manipulated until the skimmers locate into the valve base. The front section is then bolted on and final adjustments made before the top of the turret is added isolating the chamber.

Calculation of the pumping speed availability

A consideration of the available pumping speed will assist in the evaluation of the pulsed beam source.

Consider figure 4.3 which depicts, schematically, the neutral beam chamber and its diffusion pump. For the beam to work efficiently, and in order that the diffusion pump does not stall and has constant pumping speed, molecular flow conditions must be maintained. Thus, for the following calculation, molecular flow conditions are assumed. A guide to the maximum pressure, where molecular flow conditions hold, is when the free path of the molecules = the tube diameter. For a pipe of $\phi 11$ mm the pressure (P) must satisfy the inequality: $P < 5 \times 10^{-4}$ torr.

The dimensions of the neutral beam source are shown in figure 4.3. The bend in the pipe can be ignored and the length of the pipe along the centre line (l) of the pipe is used in equations for a straight pipe (of equivalent dimensions).

Comparison of the pumping speed of the naked diffusion pump (DP_{S_m}) and the pumping speed of the diffusion pump and the arm ($^{arm}S_m$) indicates a significant reduction. The total speed $^{arm}S_m$ is just 110 l.s^{-1} compared to $DP_{S_m} = 300 \text{ l.s}^{-1}$ for air. This value holds provided that the orifice at the top of the arm is completely unobstructed. In practice this molecular pumping speed for air for the stack is not the quantity available, because the conductance of the turret is not infinite. The orifice is ~ 50% obstructed at the throat, when the mounting support is loaded in the absence of the stagnation chamber. Thus, combined pumping speed is estimated to be 55 l.s^{-1} . When the valve, stagnation chamber and skimmers are all mounted in the turret then the pumping speed is significantly ~~reduced to~~ ^{reduced to} ~~less than~~ ^{less than} ~~below~~ 55 l.s^{-1} . The turret is approximately 1/3 filled by irregular shaped equipment. A final complication is that the initial pulse is fired in a direction perpendicular to the pumping orifice. If these problems are considered in the analysis, then it must be conceded that the actual pumping speed of the full system is much less than 55 l.s^{-1} and that it is also incalculable.

The throughput of a system in the steady state can be equated at each of the end of the pipe. The throughput (Q) is given by:

[69]

$$Q = S_i P_i$$

S_i = the pumping speed at the point i, P_i = the pressure at the point i.

Hence, the actual pumping speed of the system could be determined experimentally using a calibrated leak, but this has not been done to date.

The pump-out time constant is of interest when using a pulsed beam source, because the system is not in a steady state. The high transient gas load deposited into the turret must be pumped away before the next pulse is fired. Gentry writes the background pressure as a sum of exponential decays ¹⁸⁴. In his method, the time-dependence of the background signal is recognised. This limits the repetition rate of the valve, and in combination with the duty factor limits the rate of data collection for

valves delivering short pulses. Such a determination is important if the system is run at a gas load close to stalling the diffusion pump, otherwise the concept of pump out time constant can be used to select a suitable repetition rate experimentally.

Development of a simple motor valve

A design of pulsed neutral beam valve had already been chosen at the outset of this project. A prototype valve, from the design of Gorry and coworkers¹⁹⁹, was completed within the first three months of this project. The performance of the prototype valve was poor compared with the performance data quoted in the literature (see column 5 of table 4.1). The following section describes briefly some specific problems encountered and their solutions. Some of the data described here were recorded during a visit to the University of Manchester. Dr P. Gorry's cooperation in a visit to his laboratory is gratefully acknowledged.

Preamplification

The pulse from the valve was detected using a fast response Bayard-Alpert type ion gauge. The ionised portion of the pulse was collected on the central electrode of the gauge and was pre-amplified for display on an oscilloscope. Initially the detected signal from the ionised gas pulse was preamplified using a circuit based on the design of Gentry and Glese¹⁹⁸. That circuit gave poor electronic stability: the circuit easily broke into oscillation. No good signals were measured using this preamplifier and so it was replaced with a design based on that of Keyser *et al.* See figure 2.13 for the circuit diagram.

Magnetic flux

The measured flux of the original, naked magnet was 0.23 T. This value was found to be almost $\frac{1}{3}$ reduced from the batch average of 0.32 T quoted by the manufacturer. This magnet was remagnetised and soft iron pole pieces added to

concentrate the flux in the region of the ribbon. The magnetic field strength was remeasured after these modifications to be 0.8 T. Gorry quotes a magnetic field strength of 1 T in his original paper. This value was based on geometric considerations and overestimated the flux by some 25-33 %. The most concentrated magnetic field measured 0.9 T between pole pieces was designed to give a rise to a field much larger than 1 T. Subsequent magnets have been developed, with pole pieces, to generate a measured field of 1.2 T in this work.

Pulsed source control unit

Consider the pulses shown in figure 4.4. This figure shows the current pulse output from the PSCU. These pulses are the electronic drive signals from the different pulsed source control units. The relative maximum current pulse measured was ≈ 10 as large for the Manchester PSCU. In addition the pulse shapes were different. The fast switch off thyristor was changed, and the charge recovering diode and the inductor were removed from the circuit in the Warwick PSCU. Gorry's unit also incorporated paper oil capacitors obtained from an old television. The half life for discharge of the fastest modern polypropylene capacitors used in the Warwick PSCU is less the speed of the paper oil capacitors. Such capacitors are no longer commercially available.

Nozzle

A deposit underneath the hole was observed consisting of a white/pale green compound. This deposit was asymmetric indicating that the beam expansion was not axisymmetric. A subsequent, more detailed inspection of the nozzle, indicated a second small deposit on the edge of the nozzle. In the absence of further evidence this may be consistent with an emission of Cu particles from the ribbon during transient heating. Old ribbons become much brittle and lose their cupric lustre. These observations are also consistent with the proposed copper atom emission, however, direct evidence, as might be gained from a surface analysis of the ribbon, has not been collected.

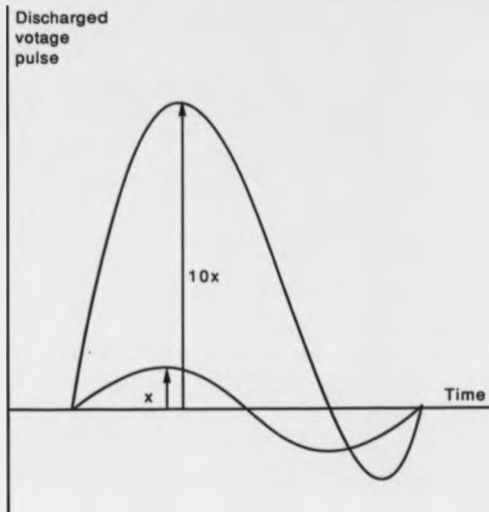


FIGURE 4.4: A SCHEMATIC REPRESENTATION OF THE RELATIVE PULSE SHAPES AND PULSE HEIGHTS, BETWEEN THE PSCU OF GORRY AND THE ORIGINAL PSCU OF WARWICK, AT THE TIME OF A VISIT TO GORRY'S LABORATORY IN MANCHESTER.

The jet test was designed to quantify the deviation of the effluent jet from the axis desired. The deviation of the water jet correlated strongly with the lobe of the deposit. By constructing the valve in its pressure box and repeating the experiment it was shown that the reverse jet was diametrically opposite the lobe of the deposit. Repeating the measurement with a forward jet produced a deviation in the same direction as the deposit lobe and of the secondary deposit. Example results are drawn in figure 4.5.

This jet test was used as the preliminary test to examine the quality of new nozzles. In all, eight further nozzles were constructed. Two of these provided a satisfactory jet test. One of these was fabricated using a spark erosion method. The addition of the silastic silicone sealant to this nozzle, however, altered the water jet performance. The silicone sealant ^{contains aluminum silicate which liberates acetic acid during chemical curing.} is supplied in a suspension of glacial acetic acid. The silicone does not seem to be dissolved by any solvent, including glacial acetic acid, after it has set. Silicone which adheres to the textured sides of the nozzle orifice, formed in the spark erosion process, cannot easily be removed by mechanical methods. Another acceptable nozzle was formed by drilling with high speed cobalt drills. The dominant problem after successful manufacture has been keeping the orifice clear of obstruction. Acceptable performance was maintained by safeguarding the nozzle when applying the silicone and by using painstaking cleaning procedures.

The performance of the valve improved following these modifications, pulses were obtained of $\sim 60 \mu s$ FWHM. Although the performance did not match even that of the Gorry's ^{maximum} pulse ^{width}, the results were encouraging.

A New Valve Body

The prototype valve designed by Kelly, was not suitable for installation into the main apparatus for these reasons:

- 1 It was not possible to fit the valve into the stagnation volume without dismantling it (~~the valve~~).



FIGURE 4.5: A SKETCH OF THE SORT OF RESULT OBTAINED, USING THE WATER JET TEST,
IF THE NOZZLE IS NOT IN ALIGNMENT

- 2 The base plate and stagnation box had several holes in sealed only with screw threads.
- 3 There was insufficient adjustment for the pulsed beam, because the stagnation volume was too large.
- 4 The skimmers could not be aligned reliably.

A new valve was designed to remove or minimise these problems. Particular care was taken to ensure that the nozzle and skimmers would be coaxial and easy to construct. The valve is shown in plate 2, and an exploded view of the valve is shown in figure 4.2; the design sheets are in appendix 2.

Some of the dimensions of the prototype valve were retained in the new design, so that some of the original parts could be used: thus reducing the construction time. The parts which were used again were the jaws and jaw supports. It was thought that these had little effect on the pulse performance, but later in the development the slack fit of the jaws was made tighter by silver soldering on to the metal and back machining. It was also found that the grip of the jaws on the ribbon had a small effect on the pulse. Superior performance was obtained using ribbons trapped between the jaws when using a PEEK lower mandible and a 1 mm glass fibre impregnated viton upper mandible. The length of the electrical connections in the main equipment was minimised and the leads on the test cell inductance matched, to make the conditions of the test cell set up transferrable *to the main apparatus*.

The new valve, turret and skimmers alignment took = 1 year to construct. The modifications to the original design were made on empirical grounds. The ribbon carrier was made to fit rigidly into the base plate fixing the hole concentrically. The length of the aperture was reduced to improve the speed of the expansion. Both of the modifications increased the complexity of the ribbon carrier adding to the cost and construction time. The design is considered below.

Geometric considerations of the design specifications

In the following sections the new valve body is evaluated.

Nozzle

A cross section of the nozzle is drawn in figure 4.6. Using the shock structure of a free jet, it is possible to assess the contribution of the walls to background molecules in the source. It was assumed that the gas jet was unaffected by the walls of the nozzle down stream, if they were recessed by a large enough distance. This empirical reasoning, used in the design of the new nozzle is valid, but is not ^{necessarily} strictly valid for the actual construction. From the Prandtl-Meyer equation (equation (64)), valid for a continuum flow, a free jet accelerating from $v = 0 \rightarrow \infty$ sweeps out an angle of 130.4° from the beam axis. Thus, for true vortex formation the nozzle must be acutely angled with a total included angle at the tip of no more than 98° .

Using a cosine ²¹⁰ angular distribution estimated from the peaking factors of Beijerinck and Verster ²¹⁰, 6% of the total mass flow could be reflected from the down stream walls of the nozzle. This estimate is given for the configuration and dimensions shown in figure 4.6. That is, 6% of the molecules leaving the source have initial angles, which in the absence of further molecular collisions, would lead to a collision with the down stream nozzle walls.

If a transient shock structure is assumed to be established during the expansion then several angles can be calculated. The position of the Mach disc is given by the equation:

[70]

$$\frac{X_m}{d} = \frac{2}{3} \left\{ \frac{P_o}{P_b} \right\}^{\frac{1}{2}}$$



FIGURE 4.6: A CROSS SECTION OF THE PULSED BEAM NOZZLE WITH A SUPPOSED SHOCK STRUCTURE DRAWN ON

The barrel shock wave has a maximum diameter of $\approx 0.75 \lambda_m$ between 0.5 and 0.75 of the distance to the Mach disc¹⁹⁵. The results are independent of the stagnation pressure, because the position and size of the Mach disc scale identically with pressure. Table 4.2 illustrates this point with sample calculations of the angles α, β, γ using a value of $0.67 \lambda_m$ for d_0 .

The barrel shock wave is a dense region of gas and can be formed completely within the confines of the down-stream nozzle wall. The barrel shock wave may serve to shield the overexpanded portion of the beam from the molecules reflected from the nozzle walls out of the under expanded portion of the gas pulse. The presence of solid objects down stream of the nozzle may cause a deterioration of the nozzle performance. Most pulsed valves have a downstream portion which blocks rectilinear trajectories in part of the forward hemisphere (2π solid angle). The effect of this portion may only be to limit the terminal Mach number of the nozzle as in a Laval nozzle.

Skimmers and turret

The terminal velocity of a beam expanded from a stagnation temperature of 298 K, may be as large as 730 m.s^{-1} for O_2 . At this velocity a beam of $100 \mu\text{s}$ duration (full width at base) would be $\approx 73 \text{ mm}$ in length. The number density of the background molecules, through which the beam passes, is constant over the duration of the pulse provided that the shortest path of a molecule deflected out of the beam, and then back into it, requires less than $100 \mu\text{s}$ to complete. For any number of elastic reflections this must be 73 mm per surface encountered. ^(total path) The volume of the turret has been maximised with this effect in mind. The mounting plates for the skimmers, however, offer a shorter path than the minimum suggested in the previous argument and allow almost direct scattering back into the beam. These plates are necessary for the dynamic differential pumping of the source and so they can not be removed. It is not currently possible to cryopump the skimmer plates.

In a low density region the effect of the skimmer orifice can be assessed by a simple consideration alone. Molecules from the beam incident on the annular orifice of

TABLE 4.2: Sample calculations of the α, β, γ angles as a function of P

	P_0	P_b	$\frac{x_m}{d}$	x_m ($d = 0.5$ mm)	x_m ($d = 0.4$ mm)
A	1000	2.13×10^{-5}	450	220.5 mm	183.8 mm
B	1000	4.26×10^{-5}	1028	513 mm	140.4 mm
C	1000	71	25	12.5 mm	10 mm

	d_{eff}/mm	x_m/mm	d_y/mm	x_y/mm	α	β	γ
A	114.8	220.5	172.1	153.8	43.5°	28.2°	14.0°
B	258.5	513	384.7	343.7	43.5°	28.2°	14.0°
C	8.25	12.5	9.4	8.4	43.5°	28.2°	14.0°

the skimmer are reflected according to the cosine distribution around the angle of specular reflection. In such a case = 48% of the scattered beam would be expected to be reflected directly into the path of the on coming beam. If the the magnitude of the solid angle occupied by the skimmer orifice edge is known the number of beam molecules reflected into the beam can be determined from the intensity, usually quoted in units of $\text{sr}^{-1}.\text{s}^{-1}$. Even from this simple analysis the minimisation of the skimmer wall thickness at the intercepting orifice can be seen. In the presence of a high density of gas the role of the skimmer is even more critical. An oblique shock wave from the edge of the intercepting orifice is obtained. The cause of the shock is the change of direction in the gas which must occur causing further expansion. The expanding gas is again subject to the Prandtl-Meyer equation. This shock wave will detach from the end of the skimmer if the orifice is blunt. This minimises the angle through which the gas must turn reducing the work done. The high density region of the shock is made thicker and is brought forward into the path of the oncoming beam. This effect can cause severe attenuation of the beam.

An estimate of the full width of the beam at the crossing region can be made using geometric considerations. This estimate is made by considering two skimmers of 1 and 2 mm orifices placed at 15 and 30 mm from the nozzle aperture respectively. Laminar flow along rectilinear streamlines is assumed. The beam spread projected on to a distant plane is then given by:

[71]

$$d_x = d_N + 2x_{Cr} \cos \theta$$

$$\theta = \tan^{-1} \left[\frac{d_s - d_N}{2x_s} \right]$$

d_s = diameter of the beam at the crossing region, x_{Cr} = distance to the crossing region, d_N = nozzle diameter, d_s = skimmer orifice diameter, x_s = distance to the skimmer orifice.

The flow is not straight, however, and the beam expands after the final aperture due to the contribution of the perpendicular velocity of the beam. In a normal expansion the so called perpendicular temperature, characterised by an energy distribution perpendicular to the axis, continues to cool throughout the expansion. In practice the first skimmer provides efficient quenching of the expansion, decreasing the ratio of velocity to the local speed of sound, perpendicular to the axis of the expansion.

Loss calculations

Attenuation of the neutral beam is caused by scattering by molecules in the background gas, and by direct interference from the skimmers. The contribution to the attenuation from the background gas can be calculated from the Lambert-Beer equation. This can be written in terms of the pressure in the background of the expansion chamber as:

[72]

$$\frac{I}{I_0} = \exp - \left\{ \frac{P \sigma l}{kT} \right\}$$

I = beam flux at pressure p , I_0 = beam flux if the pressure p were zero, p = chamber pressure, σ = soft sphere cross section for collision, l = path length, k = Boltzmann constant, T = temperature of the background gas (where applicable).

For a turret pressures of 5×10^{-4} mbar (5×10^{-2} Pa) and 1×10^{-3} mbar (10^{-1} Pa), at $T = 293$, $\sigma = 2 \times 10^{-19}$ m², and $l = 6 \times 10^{-2}$ m the beam is reduced from I_0 to 86% and 74% respectively.

Performance

During much of the development of the valve no method was available to store the satisfactory or interesting pulse wave forms. The quantitative work in this chapter has been performed using a limited amount of data.

Consider figure 4.7, it shows a Polaroid photograph of ≈ 4500 pulses. The pulse measures $60 \mu s$ at FWHM, and indicates the reproducibility of the pulses. Some of the contribution to the line width is caused by electrical interference. The reproducibility of the peak height is estimated to be better than 8.5%, based on the variation in peak height from a fixed point on the base line.

Figure 4.8a shows a similar pulse, recorded using the DSA 524 A and oscilloscope. The wave form is an average of 256 pulses. Note the similarity in form between this pulse and the photographed pulse, indicating equivalent operation. A different type of pulse is shown in figure 4.8b. There is a second discreet maximum in this wave form, which is from the *first bounce* of the pulse. This behaviour is typical in the valve if the ribbon is not set up correctly. There are precedents where four or more bounces are observed, and it is possible, under some conditions, to generate a single pulse in the position of the first bounce. These conditions are normally unstable leading to a reduction in performance and reproducibility with time. Once some proficiency in constructing the valve was gained, it was possible to avoid the formation of more than three pulses.

The figure 4.9 depicts a plot of background pressure versus pulse width (driving voltage). This plot is referred to as "*the opening function of the valve*". The salient features of the plot are:

- 1 The decrease in background pressure for an increase in *pulse width*, below the threshold for opening the valve.
- 2 The plateau region between 60 and 80 % of the maximum pulse width.
- 3 The linear increase of the background pressure with pulse width, beyond the bursting point.

There are several other observations regarding the performance of the valve. There is quite a strong variation in performance associated with the repetition rate. At low rep. rates a larger *pulse width* is required to open the valve. At high rep. rates there appear to be favourable frequencies for the desired operation. A prominent bounce can be minimised by picking out these natural frequencies. In the case of

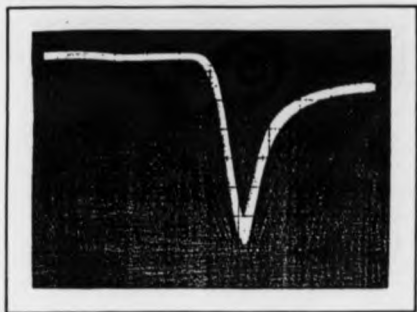
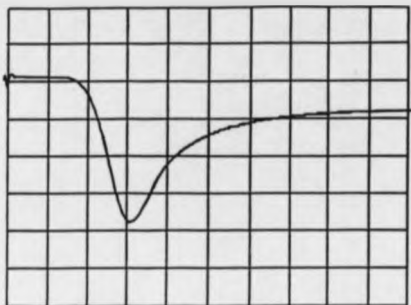
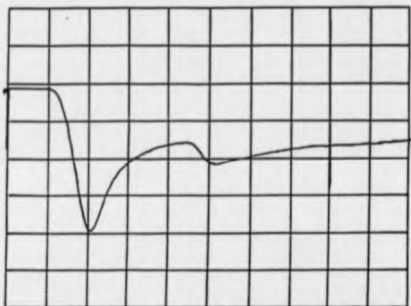


FIGURE 4.7: A REPRODUCTION OF A POLAROID PHOTOGRAPH
OF > 4500 PULSES

A



B



**FIGURE 4.8: TWO PULSES, A AND B, RECORDED AND ARCHIVED
USING THE DSA 524A IN DIGITAL AVERAGING MODE**

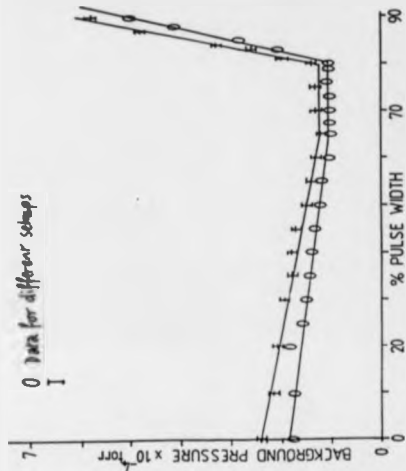


FIGURE A.9: A PLOT OF THE BACKGROUND PRESSURE IN THE PULSED BEAM VACUUM TEST CELL VERSUS A FUNCTION OF ENERGY PULSE WIDTH

operating the valve at high gas loads then strange peak shapes can be observed. This happens when the sum of the AC and the DC components of the pulse exceed the line voltages of the operational amplifier and the signal output on the oscilloscope clips.

The pulsed valve has also been tested *in situ*. A pulse has been observed to expand across the vacuum chamber. As expected, this pulse is spread out by the time of flight of components in the beam of different velocities. When the skimmers assembly was added, the pulse appeared to be quenched. An attempt was made to measure the Δ half width of the pulse. The results seem to indicate a homogeneous central portion of the pulse: ≈ 30 cm broad at ≈ 40 cm from the source.

Model for the pulsed beam shutter envelope

These sections include a full development of the biased harmonic oscillator model. In an attempt to produce a formula for the calculation of the non-steady flow developing from any pulsed beam source. This model is discussed and compared using data from the pulsed beam design.

Preliminary considerations

An analytical expression can be derived to model the shutter function of the valve. Consider figure 4.10. We assume, firstly, that the valve orifice has portions Δ_1 and Δ_2 , which, for the purpose of the model, can be treated separately. The gas flow from the valve is moderated by the bottle neck of the conductances of the two portions. Consideration of the relative conductances in the viscous flow regime will provide the basis of the model.

We assume that the flow is streamlined and laminar throughout the, so called, *control volume* shown in figure 4.10. Under the conditions of fully developed viscous flow (Poiseuille flow), it is possible to produce analytical expressions for the conductances. The velocity in a Poiseuille flow is related by 198;

TABLE 4.3: MEASURED AND CALCULATED QUANTITIES IN THE DETERMINATION OF THE RIBBON LIFTING FORCE

Quantity	Measure	Error
d_B	$7.0 \times 10^{-3} \text{ m}$	$\pm 5 \times 10^{-4} \text{ m}$
d_A	$5.0 \times 10^{-3} \text{ m}$	$\pm 3 \times 10^{-4} \text{ m}$
B_B	0.98 Wbm^{-2}	$\pm 5 \times 10^{-3} \text{ Wbm}^{-2}$
B_A	0.33 Wbm^{-2}	$\pm 3 \times 10^{-3} \text{ Wbm}^{-2}$
t	$6.6 \times 10^{-6} \text{ s}$	$\pm 0.2 \times 10^{-6} \text{ s}$

d_B Length of section b

d_A Length of section A

B_B Magnetic flux across B

B_A Magnetic flux across A

t Time to cross the ribbon

3.76 $\mu\text{F} \pm 10\%$ discharged into the ribbon and cables.
This is set at the pulse width or driving voltage.

*This table should be placed
after page 114.*

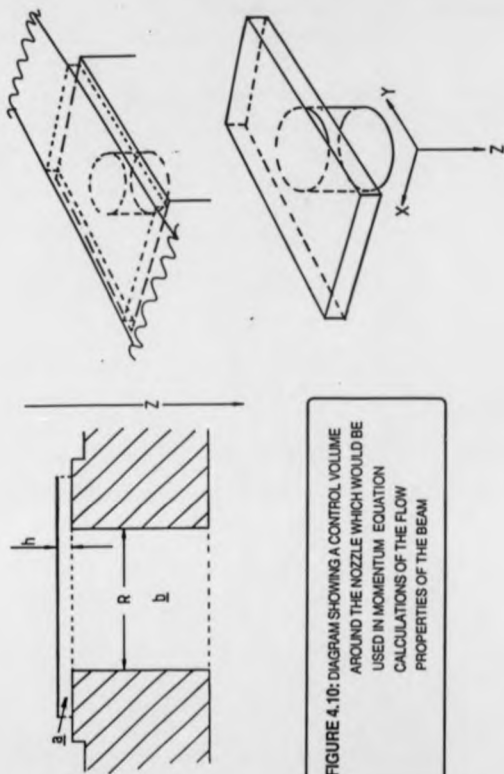


FIGURE 4.10: DIAGRAM SHOWING A CONTROL VOLUME AROUND THE NOZZLE WHICH WOULD BE USED IN MOMENTUM EQUATION CALCULATIONS OF THE FLOW PROPERTIES OF THE BEAM

[73]

$$U \propto X_{\max}^2 - X_i^2$$

U = velocity of Poiseuille flow, X_{\max} = maximum distance from a reference point,

X_i = distance to the point at which the flow is calculated.

From this relation, the flow through a circular tube of radius R and length l can be obtained:

[74]

$$C_0 = \frac{\pi R^4 \cdot (P_1 - P_2)}{8l\eta}$$

C_0 = conductance of a pipe of circular cross-section, R = pipe radius, P = pressure, l = pipe length, η = viscosity of the fluid.

The flow is driven by the pressure difference between the ends of the pipe, $(P_1 - P_2)$.

Similarly the flow between two flat, parallel plates, (in the absence of perturbations at the edges), is given by:

[75]

$$C_0 = \frac{\pi w h^3 \cdot (P_1 - P_2)}{12l\eta}$$

C_0 = conductance of a flat plate section, w = width of the plate, h = separation of the plates, l = length in the direction of the flow, η and P as before.

These two functions are plotted in figure 4.11. In a pulse beam experiment, we can state that h , the separation of the shutter and valve seat, varies as a function $H(t)$ of time:

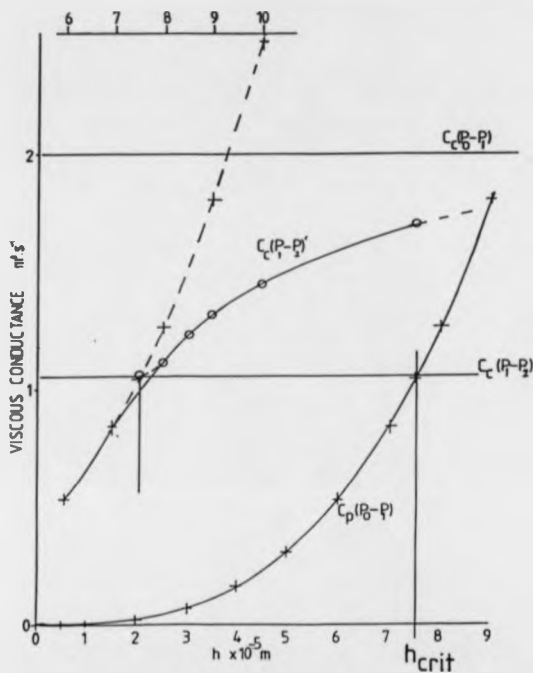


FIGURE 4.11: A PLOT OF THE BOTTLE NECK IN THE CONDUCTANCE OF THE PULSED VALVE VERSUS THE HEIGHT ABOVE THE VALVE SEAT

[76]

$$h = H(t)$$

The value of the pressure drop over the portion h may also vary in time. In this case, under conditions of viscous flow, the time dependent mass flow is related also to the pressure. This must be taken into account when calculating the bottle neck i.e. the smallest conductance. The functional form of $H(t)$ will be discussed later. There is a turning point (h_{max}) in the value of h , depending on the function, $H(t)$. For any value of h the relative conductances can be obtained from this graph.

Referring to figure 4.11, following a rupture of the valve seal, the conductance of the valve follows a second function, this time depending on $H(t)$. The ambient gas expands into the vacant space at the nearly ^{at} background pressure P_0 until the ratio P_0/P_b exceeds a critical value G ¹⁹⁵:

[77]

$$G = \left\{ \frac{\gamma+1}{2} \right\}^{\frac{\gamma}{\gamma-1}}$$

A further change in the pressure ratio, P_0/P_b , does not affect the effective pressure (P_{eff}) between portions a and b . The stagnation gas is under expanded and cannot move into the control volume at a higher pressure. The effective pressure P_{eff} under the valve shutter is given by ¹⁹⁵:

[78]

$$P_{eff} = \frac{P_0}{G}$$

This is the minimum effective stagnation pressure of portion b , i.e. the valve. The conductance of h is shown in figure 4.11, plotted for this minimum pressure, P_{eff} , and for the maximum pressure, P_0 . The maximum value is set by withdrawing the shutter to infinity when $P_{eff} = P_0$. The point of intersection between the lower conductance of

the portion b and the portion a at the relevant value of h is termed h_{crit} . The point, h_{crit} , is the first point at which the conductances are equal. The imposed pressure differences are $\frac{P_0}{G}$ and $\frac{P_{atm}}{G}$ for a and b respectively.

We make the further assumption that, everything that flows in through a also flows out through b up to the point at which the lift of the ribbon becomes h_{crit} . Beyond this point, the pressure in the stagnation-volume of b must increase asymptotically to the pressure P_0 , also causing an increase in the conductance of b . The functional dependence of the pressure in this volume on h above h_{crit} can be derived. The conductance of the system increases linearly with excess pressure P_1 .

We define C_c' and C_p' to be the conductances described in equations [74] and [75] with the pressure dependence removed. It can be shown that:

[79]

$$P_1 = \frac{C_c' P_0}{C_p' + C_c' (1 - \frac{1}{2})}$$

The behaviour is slightly different when the valve shutter closes. As the shutter moves from *infinity* to the valve seat in a finite time, a small pressure wave is propagated. Excess pressure over P_0 is lost from the sides of the shutter almost isobarically. Thus, $P_{atm} = P_0$ for $h > h_{crit}$. ^(shutter closing) A method for the calculation of $H(t)$ is required. For this we develop the ideas of Gentry and Glese 208,198

An impulsively driven harmonic oscillator

To a first approximation the valve is considered to be a harmonic oscillator driven by an impulsive force. We define two energy terms E_k and E_p for the kinetic and potential energies of the shutter respectively:

[80]

$$E_k = \frac{m_s v_s^2}{2}$$

[81]

$$E_p = \frac{\kappa x^2}{2}$$

m_s = the inertial mass of the shutter, V_s = shutter velocity, κ = force constant,

x_s = displacement.

Under simple harmonic motion these terms interchange freely. The total energy (E_T) of the valve is then given by the relation:

[82]

$$E_T = E_k + E_p$$

Following the initial impulse, the valve shutter is opened by accelerating it instantaneously to a velocity, v_{max} . For undamped oscillation a sinusoidal wave form is induced. The time taken to convert E_k to E_p is:

[83]

$$\frac{x_{max}}{v_{max}} = \left\{ \frac{m}{\kappa} \right\}^{\frac{1}{2}}$$

The natural period of oscillation (ω) is, therefore,:

[84]

$$\omega = 2\pi \left\{ \frac{m}{\kappa} \right\}^{\frac{1}{2}}$$

and the displacement of the shutter in free oscillation is:

[85]

$$x = x_{max} \sin \frac{t}{\omega}$$

[86]

$$x = x_{\max} \sin \left[2\pi \left\{ \frac{m}{k} \right\}^{\frac{1}{2}} \right]$$

The biased SHO model

A barrier is present in the valve forming the mechanical seal of the shutter. This barrier is denoted E_b , and can be represented in terms of a biasing function. This function can be expressed using an equivalent energy obtained from an apparent seal of x_{seal} as follows:

[87]

$$E_b = \frac{\kappa(x_{\text{seal}})^2}{2}$$

The plot of natural period versus displacement is shown in figure 4.12 for the unbiased oscillator. The effect of the biasing function on the actual period is shown in figure 4.12. The open time of the valve can be treated as a phase angle ϕ_1 of the total natural period in the unbiased case by:

[88]

$$\phi_1 = \frac{2\pi\Delta t}{T}$$

ϕ_1 = phase angle of ω , the natural period, Δt = pulse duration deviation

Writing $a = \sin\theta = x_s/x_{\max}$ then ϕ_1 can be shown to be:

[89]

$$\phi_1 = \tan^{-1} \left\{ \frac{2a(1-a^2)^{\frac{1}{2}}}{(1-2a^2)} \right\}$$

Now rearranging the barrier equation [87], x_{seal} can be expressed as:

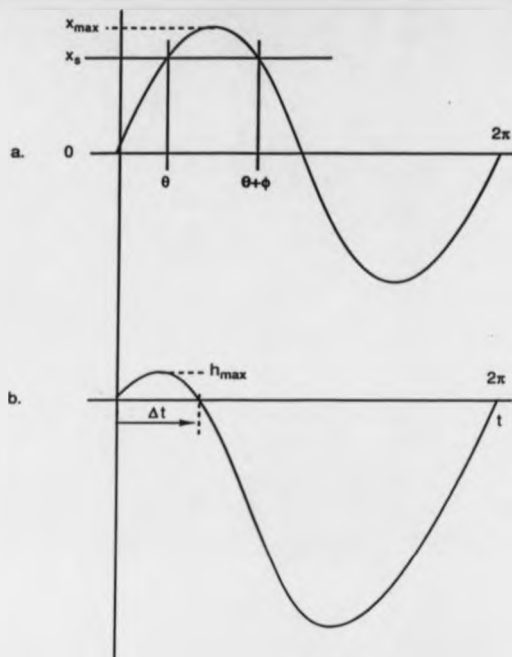


FIGURE 4.12: DIAGRAM TO SHOW THE SIMPLE HARMONIC OSCILLATOR MODEL AND THE EFFECT OF APPLYING A BARRIER OR BIAS.

[90]

$$x_{\text{SEAL}} = \left\{ \frac{2E_b}{\kappa} \right\}^{\frac{1}{2}}$$

We can also write that:

[91]

$$E_{k\text{max}} = \frac{\kappa(x_{\text{max}})^2}{2} = \frac{\kappa(x_{\text{seal}} + h_{\text{max}})^2}{2} = E_{p\text{max}}$$

substituting for x_{seal} , $E_{p\text{max}}$ and $F = \kappa x_{\text{seal}}$, and rearranging we obtain:

[92]

$$h_{\text{max}} = \left[\frac{E_{p\text{max}} + E_b - 2Fx_{\text{max}}}{\kappa} \right]^{\frac{1}{2}}$$

This equation is potentially useful, depending on how many of the variables can be calculated or measured. Now, assuming that h_{max} can be varied sinusoidally over the half period of the open phase angle, we obtain the time dependent variation of $H(t)$:

[93]

$$H_t = h_{\text{max}} \cdot \sin \left[\frac{\pi t}{\tan^{-1} \left\{ \frac{2a(1-a^2)^{\frac{1}{2}}}{(1-2a^2)} \right\}} \right]$$

This equation can be used in determining the time dependence of the shutter function by plotting the conductances, read from figure 4.11, along a time axis.

Real biased oscillator

There are two force constants associated with the different parts of the real valve. These parts are the small force constant air part and the high force constant silicone part. Under conditions where the motion is harmonic, then the energy is

conserved between these two parts. In this case the two parts can be equated at the maximum displacement:

[94]

$$\frac{\kappa_1(x_1)^2}{2} = \frac{\kappa_2(x_2)^2}{2}$$

κ_1 = small force constant, κ_2 = large force constant.

The shutter has its natural frequency modified in the same way that the phase velocity of light changes in media of different refractive indices. The total natural period then becomes:

[95]

$$\omega = \pi \left[\frac{m_1}{\kappa_1} \right] + \pi \left[\frac{m_2}{\kappa_2} \right]$$

The motion of the valve, however, is not harmonic. The collision with the valve seat is inelastic and hence the equation cannot be applied. There is a discontinuity in the wave leading to a residual force. It is likely that this is the most prominent and important mechanism for dissipating energy. The valve, therefore, has two fundamental frequencies associated with it, they are the harmonic frequencies of the biased oscillator and the real biased oscillator. The longer of these frequencies may be excited by the application of a resonant drive pulse.

There are several possible mechanisms for the dissipation of energy other than the collision with the valve seat. A back EMF is induced by eddy currents opposing the motion of the shutter in the permanent magnetic field. This effect probably accounts for the difference in the ultimate speed between the Gentry and Glese valve and that of Gorry. A modification of the forces in the shutter function can be expected from this phenomenon. Energy is also dissipated in the valve as heat and sound, caused by the resistive work done.

Bursting force on the ribbon

In order to find the impulsive driving force used to open the shutter, we define the following variables:

F = force; v = average drift velocity; V = charging voltage; B_i = local magnetic flux; Q = total charge; C = discharged capacitance; d_i = length of the conductor over which B_i acts; t = time taken for the charge to cross d ; e = electronic charge; n = total number of electrons, I = current.

Consider figure 4.13a. The force experienced by moving charge (e) perpendicular to a flux B_i is given by:

[96]

$$F = B_i e v$$

For n electrons this becomes:

[97]

$$F = n B_i e v.$$

Alternatively, we can write, $ne = Q$ (the total charge), giving:

[98]

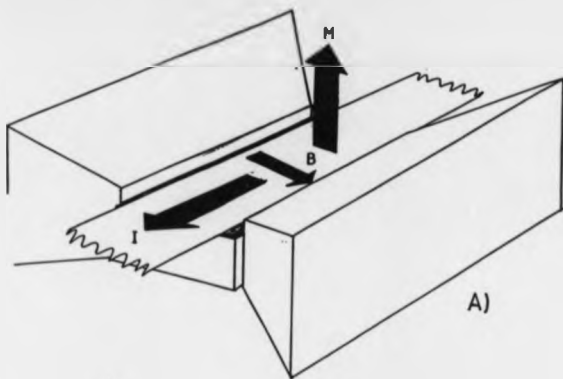
$$F = B_i Q v$$

v can be expressed as the d/t , and the equation becomes

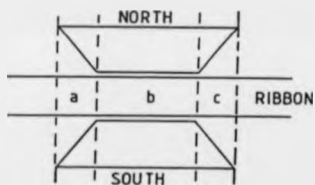
[99]

$$F = B_i Q d_i \frac{1}{t_i}$$

Now, $CV = It = Q$, and we can substitute to give either



A)



B)

FIGURE 4.13: DIAGRAM SHOWING A) THE RELATIONSHIP OF FORCES ACTING ON THE RIBBON, B) THE SECTIONS DRAWN FOR THE MAGNETIC FIELD IN A CALCULATION (SEE TEXT)

[100]

$$F = B_i C V d_i / t_i$$

[101]

$$\text{or } F = B_i |d_i|$$

Consider Figure 4.13a. We use $F = CVB_i d_i / t_i$, assuming that the magnetic flux outside s.b.c is negligible. We obtain a sum of three components, but since $d_a = d_c$, this can be written as:

[102]

$$F = CV \left\{ \frac{B_b d_b}{t_b} + \frac{2B_a d_a}{t_a} \right\}$$

or alternatively:

[103]

$$F = I(B_b d_b + 2B_a d_a)$$

If it is simple and convenient to measure the current,

In order to make a first approximate determination for the magnitude of F , we can calculate the upper bound using equation [102] and neglecting the apparent overshoot or *negative capacitance*. The total capacitance of the discharge is obtained from the bank of capacitors in the PSCU (8×470 nF). Assuming that:

- 1 All the $3.76 \mu\text{F} \pm 10\%$ capacitance is discharged
- 2 Fringing magnetic field effects are zero outside the regions specified in figure 4.13b.
- 3 The pulse time to cross d_a , d_b , d_c is the same, and that it is short compared with the valve open time, then the pulse is impulsive. Then we can state that $t = t_a$, t_b , t_c the full width of the pulse at base.

Now we can calculate a value for the lifting force (F) from the equation:

[104]

$$F = CV \left\{ \frac{B_b d_b + 2B_a d_a}{t} \right\}$$

Results are presented in table 4.3. ^(Page 104)
 $F_{Te1} = 5.8 \times 10^{-3} \text{ NV}^{-1} \pm 14\%$. The error is calculated from:

[105]

$$\text{Error}^2 = \sum \left(\frac{dF_{\text{TOT}}}{dx} \right)^2 E_x^2$$

The second method of determining the lifting force was made by a measurement of the transient current pulse. A standard test resistance of $0.05 \Omega \pm 10\%$ was wired, in series, to the live side of the valve. The voltage developed across the resistor was recorded on Polaroid film using an oscilloscope camera. The voltage was integrated and used to calculate the total transient current.

The resistance was minimised so that the current drawn by the test resistor would be negligible. However, the time taken for the pulse to cross the resistor may be longer than that to cross the ribbon. This affects the value of t used in the calculation. Figure 4.14 shows a reproduction of the Polaroid recorded. The pulse area was determined by the mass of a cut out section of film assuming constant film density. The force was $0.4 \text{ N} \pm 10\%$ for a pulse of $100 \text{ V} \pm 5\%$ at a reading of 2.1 on the PSCU vernier scale. Note the two calculated values are in the same order of magnitude: the value the calculation at 100 V is 0.58 N , this is very encouraging.

Due to the loss mechanisms such as reflection and dissipation of the test resistor, we may suggest the 0.4 N value is an upper bound. If instead we consider that the value of t may be too large then this value is a lower bound. These two effects are probably in part self cancelling. The former capacitance discharge value is a more



FIGURE 4.14: AN OSCILLOSCOPE POLAROID PHOTOGRAPH OF THE ELECTRONIC DRIVE PULSE. COMPARE TO FIGURE 4.4

rigorous upper bound, but is more useful since the functional dependence on pulse width has been derived. This function could be calibrated and then scaled for accuracy.

Forces acting on the ribbon to oppose opening.

Qualitatively we can write all of the forces contributing to the inertia of the valve. They are friction, pressure, mechanical force, weight and tension. The friction arises from the physical sticking of the ribbon on the silastic. This is expected to be small for a relatively cool valve and is neglected. The force exerted by the pressure difference across the ribbon gives rise to the pressure term. The mechanical sealing force is in part unquantifiable. The ribbon in a well set up valve is usually flat in which case ^{the force arising from mechanical sealing} this can be assumed to be zero. The weight of the ribbon is slight and is neglected. Finally the tension of the ribbon is normally neglected for the same reason as the mechanical force is neglected. This last assumption may not be good when the valve opens, as the ribbon must flex. A component of the force proportional to $\sin \theta$, where θ vanishes when $\theta = 0$, will try to restore the seal.

From these assumptions we can state that the barrier to be overcome is entirely due to the pressure difference across the ribbon.

The barrier energy

The activation barrier arises from the force exerted by 1 atmosphere of pressure (approximately 101000 Pa) over the area of contact between the ribbon and ribbon carrier ($5 \times 10^{-6} \text{ m}^2$). The barrier, by this argument, is a fixed value for each pressure and area. In this case, 1 atm and $5 \times 10^{-6} \text{ m}^2$, this value is 0.505 N.

^{0.5 -}
This value may be reduced to 0.5/G, if the valve does not reseal fully after the first time of opening. This is a quantitative estimate of the ease with which the valve may reopen giving rise to secondary pulses.

Discussion

Mechanisms of loss

We can speculate that there are other vibrational modes in the valve, into which energy can flow by dispersive coupling, but which are not actively coupled to the opening function. There is also electrical loss caused by changes in the impedance at the connections and solder joints. The reflection of the initial drive pulse reduces the impulsive drive force, but the electronic reflections are over in a time much too short to cause secondary pulses. Matching the impedance of the cables and valve at the junctions may offer some reduction in the power requirements.

Frequency dependence of the pulse

Residual energy left in the valve may exceed the energy required to open the valve a second time. For this to occur the energy dissipated by the valve must be less than the difference between the initial energy and that of the barrier. Bounces are observed with many valves. These are mostly due to the mechanical reflection of the shutter when the barrier has not been fully re-established. That is, the barrier is reduced, meaning that more energy must be dissipated if the valve is not to re-open. Observation of bounces is more prevalent in valves where the shutter and valve seat do not collide normally.

The model can be used to explain qualitatively some of the observed features of the operation of the valve. Statements concerning the operation under changing experimental parameters have already been made. The frequency of the operation (rep. rate) is expected to be coupled to the *pulse width* control and affects the performance of the valve, this can be interpreted as the resonant excitation of the underlying biased oscillator fundamental frequency.

Reconsider figure 4.9 showing the opening function. The biased oscillator model has the fundamental period is split into unequal, open and closed portions. At a current pulse energy less than the threshold required to surmount the barrier, the net

seal of the valve improves when a pulse is applied. This explains the initial observation of a decrease in the background pressure of the expansion chamber. Increasing the pulse width would lead to a predicted low positive gradient in the background pressure as the shutter barely opens. In the plot this region is flat to within the experimental error. A final true gas burst leads to the rapid increase in the ~~average background~~ background-average pressure.

The speed of operation of the valve can be predicted to be altered by the increasing x_{seal} at a constant force constant. This reduction in pulse width is associated with a reduction in the maximum throughput of gas possible. Reducing the natural frequency of the oscillation, by increasing the force constant of the valve, at a constant $x_{\text{seal}}/x_{\text{max}}$, reduces the full width half maximum of the gas pulse measured. The cost of this increase is large in the extra power then required to open the valve.

The damping function of the valve appears to be the important criterion in the appearance or non-appearance of shutter bounces causing the secondary gas pulses. The critical operation of the valve is accounted for by this. The thresholds of many of the effects, such as reestablishing the full seal, appear through discontinuous functions. Thus, the setting up procedure can not be made into a sort of iterative convergence toward the optimum settings.

The deposited substance underneath the nozzle

Considering the beam as a continuum we can examine the Prandtl-Meyer equation in more detail. We can write that for an adiabatic, isentropic, perfect gas the angle through which beam molecules are deflected during expansion is given by:

[84]

$$\theta = \left[\frac{\gamma+1}{\gamma-1} \right]^{\frac{1}{2}} \tan^{-1} \left[\left[\frac{\gamma-1}{\gamma+1} M^2 - 1 \right] \right]^{\frac{1}{2}} - \sec^{-1} M$$

The Prandtl-Meyer angle for an expansion to $M = 8$ is $\theta = 95.62^\circ$. The increase in Mach number upon expansion, from zero at the nozzle throat, therefore, must exceed $M = 8$ for the deposit to turn through $>90^\circ$ and thus, to be deposited around the orifice exit. This is consistent with the data of Gorry, which was back fitted to an equation of Anderson and Fenn ¹⁹⁰.

Secondary pulses

A mechanical reflection of the valve shutter provides a secondary impulse for the valve to open. The valve will not open, if the energy dissipated during the first half cycle is sufficient to reduce the force below the threshold for opening the shutter. Normally the valve dissipates energy at a constant rate, and if bouncing is observed there must be another mechanism causing the secondary pulse. A bounce is possible if the energy of the barrier is reduced, or if the reflected impulse is coherent with the phase of the shutter. The reflected parts of the electronic pulse, formed where the impedance is ~~mismatched~~ ^{incorrectly matched} are over far too quickly for them to be a realistic possibility. A twist in the ribbon provides a plausible mechanism for reducing the barrier threshold. The whole of the pressure barrier cannot be established suddenly as is desired, instead, the different parts of the shutter are reflected separately, and the full seal is not quite established. An inelastic collision with the valve seat is probably the most effective mechanism for dissipation of energy. The efficiency of this process may be reduced when the collision of the valve seat and the shutter is not normal and sudden. If this were so then twists in the ribbon would be even more critical in providing a channel for secondary bounces.

Performance of the model

Figure 4.15 and figure 4.16 show the leading edge of the pulses in figure 4.8 a and b plotted against a normalised $(\sin \theta)^3$ function ($\sin \theta$ is directly proportional to h). The agreement between the plots is impressive and supports the analytical form of the expression derived in the model. Figure 4.16 b supports the theory since the x-y plot

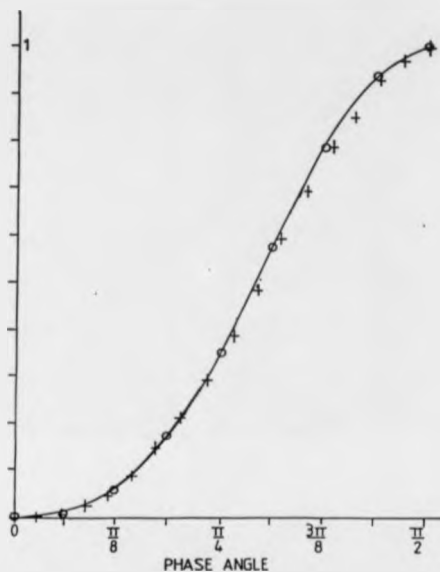


FIGURE 4.15: PLOT OF THE LEADING EDGE OF THE PULSE SHOWN
IN FIGURE 4.8B. THE DATA IS REDUCED AND SUPERIMPOSED
ON TO A PLOT OF $(\sin \theta)^3$

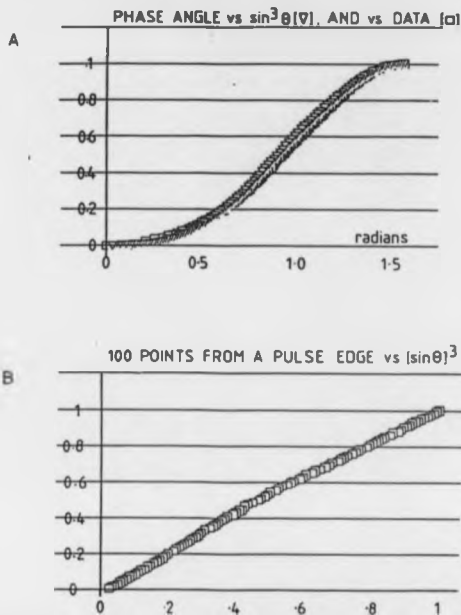


FIGURE 4.16: A) PLOT OF THE LEADING EDGE OF THE PULSE SHOWN IN FIGURE 4.8A. THE DATA IS REDUCED AND SUPERIMPOSED ON TO A PLOT OF $\sin^3 \theta$. B) PLOT OF $\sin^3 \theta$ VERSUS THE LEADING EDGE OF 4.8A. θ IS DERIVED FROM THE POINTS FOR WHICH DATA IS AVAILABLE, AND THE DATA IN REDUCED UNITS.

of the two curves is a convincing straight line. Disappointingly, it appears that P_{crit} is not reached in this valve; this would be indicated by a deviation from this line. The shutter does not fully open to provide the terminal gas flow. The pulses shown in reference 204 show the expected dependence in the leading edge. That is the pulse does not reach a plateau region suddenly, but goes into a region of slower increase, reaching the plateau asymptotically.

Prognosis

It is not possible to calculate the force constant in this valve empirically as with a solenoid valve or the Gentry and Gleason valve. In these designs the shutter is sprung and equations are available to calculate the residual force forming the mechanical seal. There must be some measurement made, however, if the force constant of the supposed oscillator cannot be calculated. This can be obtained from a measurement of the maximum displacement during free oscillation and in biased oscillation, and the maximum speed of the valve. A laser reflection experiment timed on a fast oscilloscope may give both of these in a single measurement. At least one report has appeared in the literature of the measurement of the displacement of a shutter using a laser technique.

Pulse trailing edge

The tail of the pulse has not been discussed in this chapter. Contributions to this may be expected from clustered particles in the beam, and from diffusive loss of the component of the beam down stream of the shutter when the expansion is terminated. The latter can be developed from the method of Saenger and Fenn, and the former must be analysed experimentally. The experiment to assess the contribution to the pulse from slower moving clusters can be investigated by heating the valve for expansions of the same stagnation gas. The gases used may be seeded beams and beams of pure particles. Helium, for instance, has a very shallow well for formation of a dimer and would be expected to produce the sharpest pulses, even disregarding its

lower molecular mass. Argon or krypton expansions may show significant longer tails due to their higher dimer scaling rates, however, these may not be significant. The use of noble gases has the advantage that the specific heat constant must remain constant throughout the expansion, eliminating the possibility of unwanted complicating effects such as diatomicity.

Calculation of flow field properties

There is a prospect of calculating the time dependent flow field properties using the model shutter function. The calculation can be made in principle, by following a procedure of:

- 1 Calculating the subsonic flow velocities and mean free paths as a function of time at the nozzle exit.
- 2 Scaling the expected number of collisions to the shutter function.
- 3 A quitting surface position is chosen and the collision number expectancy calculated for each section of the expansion.
- 4 A minimum threshold is chosen for the number of collisions required for a continuum analysis of beam properties. For these sections the properties can be calculated allowing a function of two independent variables to be described $F(N_V, P_V)$. This function is all that is required to predict the time of flight envelope.
- 5 Remaining velocities not described by the continuum can be predicted from a thermal spread of velocities around the subsonic velocities, because these have not reached fully developed flow.

Measurement of the distribution of velocities function

A measurement of the velocities at various points in the pulse can also be made. If the beam contains a suitable chromophore then the LIF doppler profiles of the beam measured in the direction of the flow, with perpendicular excitation, can be measured. The laser beam pulse duration must be kept short and then the sections of the beam can

be investigated by scanning the excitation pulse through the gas pulse by varying the delay.

Quitting surface and sudden freeze

The sudden freeze model may be applied in considering non-steady flow in the pulsed beam expansions. Each section of the shutter function will have a characteristic quitting surface at specific, but different distance from the source. The quitting surface position is determined from the index parameters: the number density ($N_{(t)}$) of the shutter function, the local mean free path and the exit velocity of the aperture. The average number of collisions required to change the speed ratio by a certain amount can be applied for each portion of the beam between the orifice of the valve and the skimmer. Ultimately there are either insufficient collisions for a continuum description to be valid or the skimmer is reached before the quitting surface, or the quitting surface is reached freezing the flow field properties upstream (molecular flow).

We note that the position of the quitting surface varies with $1/n_0$ and approaches infinity as n_0 is reduced to zero. The speed ratio should minimise at the maximum position of n_0 . If a quasi-1-dimensional momentum equation is applied to the ^{Control} jet volume (figure 4.10) then we would predict, for a continuum gas, that the exit velocity is minimised for the nozzle when the mass flow rate is greatest. This effect would partially offset the ~~the~~ movement of the quitting surface.

Conclusion

A valve has been developed and incorporated into a crossed beam apparatus. There are some problems which remain outstanding. A pulse has not been observed in the main apparatus with the skimmers in place. This suggests that the skimmers need remaking, since much effort has been directed towards ensuring that the expansion is axisymmetric. The minimum pulse width of the valve has been measured at ca. 60 μ s

FWHM. This is significantly longer than pulses quoted as: no longer ^{in duration} than 45 μ s. (FWHM) recorded on a similar valve ¹⁰⁰. The difference can be attributed to differences in the force constants of the valves, operating as harmonic oscillators.

A model has been derived which explains qualitatively, all the observations and effects of the valve. The form of the critical dependence on the position of the shutter above the valve seat has been tested and the results are encouraging. The salient features of the operation of the valve can be summarised:

- 1 The valve seal improves below the opening threshold, because the biased oscillator spends longer during a period directing the impulse at the valve seat.
- 2 There is a complicated dependence of the valve parameters on pulse repetition frequency, caused by the excitation of resonant frequencies in the valve.
- 3 The secondary pulses are caused by bouncing the shutter. The condition for this to occur is that the residual energy of the valve is larger than the energy required to open the shutter. This condition is met when the full seal of the valve is not suddenly reestablished. Examples of conditions under which this may occur are if the ribbon is twisted or the forces on the ribbon are not centralised.
- 4 Independent evidence is provided that some of the particles in the beam reach Mach 8 or better.
- 5 The nascent number density forming the gas pulse at TOF = 0, depends on the ratio of two conductances in the viscous regime. This function is expected to follow $\sin^2 \theta$ dependence up to a critical opening point. This point represents the point at which the portion of the aperture, limiting the gas flow, changes from a to b.
- 6 The trailing edge of the valve has the same dependence as the leading edge, reflected through the peak maximum. There is an overlapping function causing the longer tail which has not been quantified. This function may be due to both clustered molecules undergoing velocity slip and the collapse of the expansion.

Methods have been described in which specific further investigations for the model can be made. These investigations are anticipated to make the model more useful quantitatively. A plausible methodology has also been suggested for the development of these ideas to the calculation of the time dependence of non-steady flows.

5



CONCLUSIONS

Summary of positive aspects of this work

This thesis sets out a more rigorous and fundamental approach to the understanding of an instruments systematic errors. The contents of this thesis make the study of chemical reactions using this apparatus a possibility. A great deal of painstaking ground work has been made and written down such that a student, with suitable technical support, could begin at the point where this thesis stops. The separate parts of the instrument have been shown to work individually under carefully controlled conditions.

Prognosis for the neutral beam model

It is hoped that the model for the neutral beam shutter function will be of significant use to those requiring the calculated properties of neutral beams. The shutter function can be used in the deconvolution of time of flight spectra from pulsed beam sources and may have application to the calculation of the time dependent flow field properties.

The model requires some further development and testing, but the initial results are very promising. In order to make full use of these ideas, in the absence of a continuation student, collaboration with an established molecular beam group is desirable.

Prognosis on chemistry

A programme for the study of several chemical reactions was outlined at the beginning of this project. These reactions are mentioned in the aims section of chapter 1 of this thesis. It has not been possible to study any of these systems due to the periods of instrumental development. This development was necessary and has provided some interesting and useful knowledge. There are still, however, several reactions still left open to investigation. The crossed beam reactions of four centre two body systems have been shown, in this laboratory, to have interesting features. $CS^+ + O_2$, NO and SO would be interesting to compare to the work on $CO^+ + O_2$ and NO .

The performance of this instrument will always be limited by the choice of a CMF in the ion beam source. The fundamental flaw in using such a design has been exposed in this study. The problems encountered in producing a monoenergetic beam of reactant ions, caused by the fringing field of the CMF, does not necessarily mean that the instrument is useless. The technology required to make high resolution kinetic energy experiments possible cannot be installed into this apparatus. The instrument is dated by its design, and the choice of the geometry of the instrument even limits the choice of alternative sources. It is possible that a significant contribution to modern research could be made using the instrument in pioneering new areas of research interest. Atom exchange reactions of double charged ions would be interesting for example, and might be studied using a modified version of the present instrument. The use of a thermionic metal ion source would also allow a new range of simple reactions to be studied.

A study of the chemical reactions of double charged cations would need to be conducted in parallel to complementary theoretical studies. These reactions tend to have a large SET cross sections, which might be expected to dominate the reactivity. Thus, the theoretical studies would be useful to indicate favourable cases. In any usable case, it can be specified that the substrate must be small enough for the dynamics to be tractable, and that the reaction of interest must have a measurably large cross section. In a parallel investigation, the choice of reactant is also constrained by the complexity of the calculations required to produce accurate ab initio surfaces. Systems containing just four or five centres require considerable computer time. Small species of moderate complexity, therefore, may offer the best prospect of novel reactions. CS_2^{++} and NO_2^{++} are relatively stable and easy to obtain, and may fulfil the criteria.

Summary of conclusions (further work)

Modifications were suggested in chapter 3, based on experimental and simulation studies, to limit the effects of the RF on the primary ions' energy. These modifications remain as further work and have been summarised below for completeness.

- 1 The electron impact ion source does not give satisfactory operation. The Bayard-Alpert type source should be exchanged eg. for a more conventional crossed electron beam EI ion source. A replacement source, of whatever type, should include the following specifications. Electrons are collected away from the ion flight path. The electric field gradient over the ionisation region is small. The source parameters are decoupled giving independent operation in altering the ion energy etc.
- 2 The ions formed by the ion source should be injected parallelly into a Brubaker lens. The Brubaker lens will improve the transmission of higher mass ions and reduce the quadrupole fringing field.
- 3 The exit of the quadrupole should be field and angle stopped to reduce the transmitted beam to more first order type trajectories.
- 4 The octopole should have a new spacer built designed so that it is a push fit into the quadrupole support. It should also hold the angle and field stop apertures for the quadrupole exit.
- 5 The detector should also contain a Brubaker lens. The entrance for this lens should be flush with the exit of the RPD energy analyser.
- 6 The three lens RPD energy analyser could be remachined to reduce the curvature of field towards the margins. To avoid mechanical fabrication work the voltages can be ganged to maintain the focussing point of the threshold energy. This modification reduces the spherical aberration.

The instrument can be used with either a multicapillary array or with a pulsed valve, after a consistent and satisfactory ion beam has been achieved. There are some outstanding modifications required in either case. For use with a

multicapillary array, provision should be made to modulate the beam. This modulation should be done inside the neutral beam turret. For use with the current pulsed valve three problems must be overcome. They are:

- 1 The stray magnetic field at the crossing region should be reduced eg. by magnetic shielding.
- 2 Blunt skimmers. The new design should incorporate a sharp edged orifice and have highly polished surfaces. Electroformed skimmers of this specification are commercially available in a range of orifice sizes, and they have the optimum, curved conical-section geometry.
- 3 The problem of ensuring that the expansion is axisymmetric.

I recommend that the simple motor valve be discarded. The commercial piezoelectric valve (beam dynamics) based on the design of Cross and Valentini offers several significant advantages.

- 1 The valve is less difficult to set up and can be adjusted *in situ* using pressurised helium.
- 2 The valve does not contain a magnet, thus stray magnetic fields are unimportant.
- 3 Nozzles are relatively cheaper and are available in a range of laser drilled orifices of different sizes.
- 4 The piezoelectric valve is voltage, not current driven and so inductance effects are less important.
- 5 Use of smaller nozzles at a given stagnation pressure reduces the gas load on the system. The repetition rate, which is important because it will be the limiting factor in data acquisition in pulsed experiments, could then be increased.

Final comments

In order to answer the questions that current chemical physics research and that of the next decade will supply, a new instrument must be built. Good design would make this instrument versatile. A modular approach to design allows the replacement of parts when they become obsolete. For instance, external beam

sources, allow more flexibility in the pumping plant. The ion beam optics should be constructed from sectors. A reverse geometry commercial mass spectrometer could be used as the ion beam source. Incorporation of a fast pumping plant would enable the use of a supersonic neutral beam source. Many laboratories using high gas load sources, use an additional *dump pump* to collect the waste neutral beam from the reaction chamber. This extension of the normal pumping plant allows the use of pulses significantly longer than the dimension of the instrument to be used without an undesirable rise in the background partial pressure.

Appendix 1

References

Chapter 1 References:

- 1 "Three phases of Matter", 2nd, A.J. Walton, Clarendon Press, Oxford, (1983).
- 2 *Une formule fondamentale de théorie cinétique*, M.P. Langevin, *Ann. Chim. Phys. Ser. 8.*, 2, 245-288, (1905). A kinetic theory for dielectrics, formulated before the first ion-molecule reactions were studied, written in French.
- 3 *Collision theory and reaction dynamics*, R.B. Shirts, Ch.2 from ref. 39 pages 44-46
- 4 *Reactions of gaseous molecule ions with gaseous molecules V. Theory*, G. Giomousis and D.P. Stevenson, *J.Chem.Phys.*, 29(2), 294-299, (1958)
- 5 *Theory of ion-polar molecule collisions. Comparison with experimental charge transfer reactions of rare gas ions to geometric isomers of difluorobenzene and dichloroethylene*, T. Su and M.T. Bowers, *J.Chem.Phys.*, 58(7), 3027-3037, (1973).
- 6 *Time dependent quantum mechanical methods for molecular dynamics*, R. Kosloff, *J.Phys.Chem.*, 92, 2087-2100, (1988).
- 7 *Basic RRKM theory*, A.B.Callear, Chapter 4 in "Chemical kinetics", Ed. C.H. Bamford and C.F.H. Tippler, 2, 333-356, Elsevier, Amsterdam, (1983).
- 8 *Potential energy surfaces: Molecular structure and reaction dynamics*, D.M. Hirst, Taylor and Francis, London (1985).
- 9 *Potential energy surfaces*, Discussions of the Faraday Society 62, (1977).
- 10 *Ab initio methods in quantum Chemistry*, Ed. K.P. Lawley, Adv. Chem. Phys. 67(1,2), (1987) (Wiley-Interscience, Chichester).
- 11 *Variational transition state theory*, D.G. Truhlar and B.C. Garrett, *Annu. Rev. Phys. Chem.*, 35, 159-189, (1984).
- 12 *Statistical methods in scattering*, M. Quack and J. Troe in "Theoretical chemistry: The theory of scattering", Ed. D. Henderson, Academic Press, New York, (1981).
- 13 *Molecular reaction dynamics and chemical reactivity*, R.D. Levine and R.B. Bernstein, Oxford University Press, New York/Oxford, (1987).
- 14 *Chemical reactions dominated by long range intermolecular forces*, D.C. Clary and J.P. Henshaw, *Faraday Discuss. Chem. Soc.*, 84, 333-349, (1987).
- 15 *(L²) calculation of accurate quantal dynamical reactive scattering transition probabilities and their use to test semiclassical applications*, J.Z.H. Zhang, Y. Zhang, D.J. Kouri, B.C. Garrett, K. Haug, D.W. Schwenke and D.G. Truhlar, *Faraday Discuss. Chem. Soc.*, 84, 371-386, (1987).

- 16 *Dynamics of heavy + light-heavy atom transfer reactions: the reaction of $Cl + HCl \rightarrow ClH + Cl$* , B. Ames, J.N.L. Connor, J.C. Whitehead, W. Jakubetz and G.C. Schatz, *Faraday Discuss. Chem. Soc.*, **83**, 387-403, (1987).
- 17 *A new collision theory for bimolecular reactions*, I.W.M. Smith, *J.Chem.Ed.* **59**(1), 9-14, (1982).
- 18 *Large gas-phase cluster ions*, Faraday Symposium, **25**, University of Warwick, (December 1989), *J. Chem. Soc. Faraday Trans.*, **88**, 1990 in press.
- 19 *Dynamics of dissociation and reactions of cluster ions*, A.W. Castleman and R.G. Keesee, *Nato ASI Ser. Ser.C*, **193**, 185-217, (1986).
- 20 *Angular momentum disposal in atom exchange reactions*, S.K. Kim and D.R. Herschbach, *Faraday Discuss. Chem. Soc.*, **84**, 159-169, (1987).
- 21 *"Molecular quantum mechanics"* 2nd, P.W. Atkins, Oxford University Press, Oxford (1983).
- 22 *Molecular orbital correlations and ion-molecule reaction dynamics*, B.H. Mahan, *J.Chem.Phys.*, **55**(3), 1436-1446, (1971).
- 23 *Adiabatic correlation rules for reactions involving polyatomic intermediate complexes and their application to the formation of OH ($^2\Sigma^+$) in the H_2-O_2 flame* K.E. Shuler, *J.Chem.Phys.*, **21**(1), 624-632, (1953).
- 24 *The orbital angular momentum quantum number controls the magnitude of the angular momentum as $(l(l+1))^{0.5} h/2\pi$. The range of l becomes larger with n , the period in which an element is situated.*
- 25 *Exchange reactions of alkali metal atoms with alkali halides: a collision complex mechanism*, W.B. Miller, S.A. Saffron and D.R. Herschbach, *Faraday Discuss. Chem. Soc.*, **46**, 108-122, (1967).
- 26 *Avoided scattering along the relative velocity vector: Importance for crossed molecular beam experiments involving long-lived collision complexes*, K. Rynatow, L. Holmild and P.A. Eliotson, *J.Phys.Chem.*, **90**(21), 5101-5105, (1986).
- 27 *Iterative unfolding of intensity data, with application to molecular beam scattering*, P.E. Sluka, *J.Chem.Phys.*, **58**(11), 6052-6060, (1973).
- 28 *Consider a pair of diatomic molecules approaching a highly symmetrical (eg. tetrahedral) intermediate. A transition state close to this with just a 10° tilt in one bond in both the azimuthal and meridional polar angles and the symmetry has become C_1 . Some weak correlations may still exist for example in the case of Jahn-Teller distortion, but the larger the distortion the weaker these will become.*
- 29 ~~Similarly (to 28 above) consider a C_{2v} planar diatomic A~~
~~— stretching one axis of the triangle. —~~

~~compressing the distance from the centre of mass to the third atom, changes the symmetry to O_{2v} .~~

- 30 Pages 476-483 of ref 13.
- 31 *Bond selectivity in search of the chemists dream*, J.E. Baggott, *Chem.Br.* **24**(8), 908-912, (1988).
- 32 *Laser predissociation spectrum of $SiH^+ A^3\Pi-X^3\Sigma^-$ analysis of proton hyperfine structure*, C.P. Edwards, C.S. Maclean, and P.J. Sarrs, *Mol.Phys.*, **52**(8), 1453-1466, (1984).
- 33 *Energetics and reaction mechanisms of $SiH^+ + D_2$ and $SiD^+ + H_2$ and collision-induced dissociation of SiD_3^+* B.H. Boo and P.B. Armentrout *J.Phys.Chem.*, **91**, 5777-5781, (1987).
- 34 *"Atomic Energy Levels: $^1H, ^{23}V$ " vol.1*, US Nat.bureau of Standards, circular 467, (1949).
- 35 Reference 8 pages 199-201.
- 36 *Molecular dynamics of elementary chemical reactions* (Nobel lecture) D.R. Herschbach, *Angew.Chem.Int.Ed.Engl.*, **26**(12), 1221-1243, (1987).
- 37 *Some concepts in reaction dynamics* (Nobel lecture), J.C. Polanyi, *Angew. Chem. Int. Ed. Engl.*, **26**(10), 952-971, (1987).
- 38 *Molecular beam studies of Elementary chemical processes* (Nobel lecture), Y.T. Lee, *Angew. Chem. Int. Ed. Engl.*, **26**(10), 939-951, (1987).
- 39 *"Gaseous ion chemistry and mass spectrometry"* Ed. J.H. Futrell, Wiley-Interscience, (1986).
- 40 *"Techniques for the study of ion-molecule reactions"*, Techniques of Chemistry, **20**, Ed. J.M. Farrar and W.H. Saunders Jr. Wiley, New York, (1988).
- 41 G. Doinikowski and K.R. Jennings in press.
- 42 *Laser probing of product-state distributions in thermal-energy ion-molecule reactions*, S.R. Leone and V.M. Bierbaum, *Faraday Discuss. Chem. Soc.*, **84**, 235-263, (1987).
- 43 *Flowing afterglow and SIFT*, N.G. Adams and D. Smith, Ch.4 of ref.40, 165-220.
- 44 *The selected ion flow tube (SIFT): studies of ion-neutral reactions*, D. Smith and N.G. Adams, *Adv.At. and Mol.Phys.*, **24**, 1-49, (1988).
- 45 *Ion focussing, mass analysis and detection*, J.D. Morrison, Ch.3 of ref.39, 116-117.

- 46 Nucleophilic displacement with a selectively solvated nucleophile: The system $\text{OH}^- \cdot \text{H}_2\text{O} + \text{CH}_3\text{Br}$ at 300K, M. Hanchman, J.F. Paulson, and P.M. Hleri, *J. Am. Chem. Soc.*, **105**, 5509-5510, (1983).
- 47 "Advanced organic chemistry", 3rd, J. March, 256-259, Wiley-Interscience, New York, (1985).
- 48 The differential cross section for this reaction would be interesting and would reveal the microscopic mechanism directly. The biggest limitation of an ordinary crossed beam instrument is that only charged species are detected. The formation of two neutral species, in the exit channel, in addition to the ion precludes such a study. This is because one of the other products must be analysed in addition to Br^+ , in order to recover the differential cross sections. A modification to include LIF doppler measurements would enable the study to be made, under the favourable conditions of an accessible states, and sufficient product flux.
- 49 Kinetics and equilibria of ion molecule reactions studied using temperature variable high pressure sources, R.T. Gallagher PhD thesis, University of Warwick, (1988).
- 50 The use of triple quadrupoles for sequential mass spectrometry, P.H. Dawson, J.B. French, J.A. Buckley, D.J. Douglas, and D. Simmons
 #1, The instrumental parameters, *J.Org.Mass Spectrom.*, **17(5)**, 205-211, (1982).
 #2, A detailed case study, *J.Org.Mass Spectrom.*, **17(5)**, 212-219, (1982).
- 51 The same argument applies here as in the section on crossed beam experiments page 24-25 of this work.
- 52 Ion beam methods, J.M. Farrar, from ref.40, chapter 7, 325-416.
- 53 Collision induced dissociation of aluminium cluster ions with chemisorbed oxygen, $\text{Al}_n\text{O}_m^+(n=3-26, m=1,2)$: Influence of electronic structure on stability. M.F. Jarrold and J.E. Bower, *J.Chem.Phys.*, **87(3)**, 1610-1619, (1987).
- 54 keV collisions of $[\text{H}_3]^+$ and isotopomer ions. J. Bordes-Nagy, and J.L. Holmes, *Chem. Phys.*, **127**, 419-434, (1988).
- 55 Field ionisation of high velocity neutral species. Rydberg states in noble gas atoms; the measurement of translational energy loss in neutralisation-reionisation mass spectra. J. Bordes-Nagy, J.L. Holmes and A.A. Momms, *J.Org.Mass Spectrom.*, **21**, 629-636, (1986).
- 56 Kinetic energy spectroscopy of High Rydberg fragments from keV collisions of H_3^+ , D_3^+ , N_3^+ , and C_3^+ ions with rare gas atoms. J. Bordes-Nagy, and J.L. Holmes, *Chem. Phys. letters*, **132(2)**, 200-204, (1986).
- 57 Field desorption mass spectrometry. A technique for the study of thermally unstable substances of low volatility, H.D. Beckey, *Int. J. Mass Spectrom. Ion Phys.*, **2**, 500-503, (1969).

- 58 *Resonance-enhanced multiphoton ionisation of atomic hydrogen*, L.R. Brewer, F. Buchinger, M. Ligare, and D.E. Kelleher, *Phys. Rev. A*, **39**(12): 3923, (1989).
- 59 *Ion cyclotron resonance spectrometry*, P.R. Kemper and M.T. Bowers in ref. 40 pages 1-59, chapter 1.
- 60 ~~$^{35}\text{Cl}^+$ and $^{35}\text{Cl}^-$ can be resolved, with a resolving power of $\sim 10^5$.~~
- 61 *Energy disposal in charge transfer reactions producing NH_3^+ : Dependence of the $\text{NH}_3^+ + \text{H}_2\text{O}$ reaction on NH_3^+ internal energy*, P.R. Kemper, M.T. Bowers, D.C. Parant, G. Mauclair, R. Deral and R. Marx, *J. Chem. Phys.*, **79**(1), 160-169, (1983).
- 62 *Tunable laser fluorescence method for product state analysis*, R.N. Zare and P.J. Dagdigan, *Science*, **188**, 739-747, (1974).
- 63 Reference 13, pages 359-367.
- 64 *State selected ion-molecule reactions by a TESICO technique. XII. Internal energy dependence of the relative cross section and mechanism branching of the reaction $\text{CH}_4^+(v) + \text{CH}_4 \rightarrow \text{CH}_5^+ + \text{CH}_3$ and its isotopic variants*, Z. Herman, K. Tanaka, T. Kato, and I. Koyano, *J. Chem. Phys.*, **85**(10), 5705-5710, (1986).
- 65 *Dynamics of chemical reactions of ions from beam scattering and state selected studies*, Z. Herman and I. Koyano, *J. Chem. Soc. Faraday Trans. 2*, **83**, 127-137, (1987).
- 66 *Real-time picosecond clocking of the collision complex in a bimolecular reaction: the birth of OH from $\text{H} + \text{CO}_2$* , N.F. Scherer, L.R. Khundkar, R.B. Bernstein and A.H. Zewail, *J. Chem. Phys.*, **87**(2), 1451-1453, (1987).
- 67 *Femtosecond real-time dynamics of photofragment trapping resonances on dissociative potential energy surfaces*, M.J. Rosker, T.S. Rose and A.H. Zewail, *Chem. Phys. Letters*, **146**(3,4), 175-179, (1988).
- 68 *Femtosecond photofragment spectroscopy: The reaction $\text{ICN} \rightarrow \text{CN} + \text{I}$* , N.F. Scherer, J.L. Knes, D.D. Smith, and A.H. Zewail, *J. Phys. Chem.*, **89**(24), 5141-5143, (1985).
- 69 *Femtosecond real-time observation of wave packet oscillations (resonance) in dissociation reactions*, T.S. Rose, M.J. Rosker, and A.H. Zewail, *J. Chem. Phys.*, **88**(10), 6672-6673, (1988).
- 70 *Real-time femtosecond probing of "transition states" in chemical reactions*, M. Dantus, M.J. Rosker, and A.H. Zewail, *J. Chem. Phys.*, **87**(4), 2395-2397, (1987).
- 71 *Progress in the application of molecular beam techniques to the studies of ion-molecule collisions*, W.R. Gentry in "Ion-molecule reactions", Ed M.T. Bowers Academic Press, (1979).
- 72 This study would be very difficult and tedious to perform for several reasons. For example, there are a number of reactant ions (eg. $^{29}\text{Si}^+$, $^{28}\text{SiH}^+$ etc) which have roughly equivalent masses. These ions have

significant natural abundances, and have different reactivity towards a given neutral in forming identical products (or different products of equivalent mass) via different channels. The cross section for reaction of SiH^+ with H_2 is smaller than for Si^+ with H_2 , hence if the reaction was not performed at high resolution, extensive deconvolution would be required to recover the correct differential cross sections. Another problem is the formation of SiH^+ , in electron impact ionisation this ion constitutes less than 10% of the total product ion current.

- 73 The dynamics of the reaction $\text{D}_2^+ + \text{O}(\text{P}) \longrightarrow \text{OD}^+ + \text{D}$, and the influence of the atomic quadrupole moment on the cross section at very low energies, D.J. McClure, C.H. Douglass, and W.R. Gentry, *J.Chem.Phys.*, 67(4), 2382-2370, (1977).
- 74 The dynamics of the reaction $\text{D}_2^+ + \text{F}(\text{P}) \longrightarrow \text{FD}^+ + \text{D}$, at kinetic energies between 0.002 and 30 eV, G.F. Schuetle, and W.R. Gentry, *J.Chem.Phys.*, 78(4), 1786-1794, (1983).
- 75 The dynamics of the reaction $\text{D}_2^+ + \text{C} \longrightarrow \text{CD}^+ + \text{D}$, at kinetic energies between 0.002 and 14 eV, G.F. Schuetle, and W.R. Gentry, *J.Chem.Phys.*, 78(4), 1777-1785, (1983).
- 76 The dynamics of the reaction $\text{D}_2^+ + \text{N} \longrightarrow \text{ND}^+ + \text{D}$, D.J. McClure, C.H. Douglass and W.R. Gentry, *J.Chem.Phys.*, 88(5), 2079-2093, (1977).
- 77 Reactive scattering of ions, Z. Herman and K.R. Birkinshaw, *Ber. Bunsenges.*, 77(8), 566-575, (1973).
- 78 Transformation relationships from centre of mass cross section and excitation functions to observable angular and velocity distributions of scattered flux, T.T. Warnock and R.B. Bernstein, *J.Chem.Phys.*, 49(4), 1878-1886, (1968).
- 79 Crossed Beam Studies of the proton transfer reaction of water molecules P.W. Ryan PhD thesis, University of Utah, chapter 3, (1975).
- 80 Processing of ion-molecule beam scattering data: Framework of scattering diagrams and derived quantities, B. Friedrich and Z. Herman, *Collect. Czech. Chem. Commun.*, 49, 570-585, (1984).
- 81 Adapted from ref 6 ch.7 page 187.
and Reactive collisions in crossed molecular beams, D.R. Herschbach, *Faraday Discuss. Chem. Soc.*, 34, 149-161, (1962).
- 82 Energy and chemical reaction 1: Dynamics of simple ionic and atomic processes, R. Wolfgang, *Acc.Chem.Res.*, 2, 248-256, (1969).
- 83 "Kinetic theory of gases", E. H. Kennard, McGraw-Hill, 98-114, (1938).
- 84 $P = kT/(\sqrt{2} \pi d^2 \lambda)$
Using $\lambda = 1\text{m}$, and a molecular area of $1 \times 10^{-19} \text{ m}^2$ for N_2 the calculation = $5 \times 10^{-3} \text{ Nm}^{-2}$ or $5 \times 10^{-6} \text{ mbar}$.

- 85 Crossed beam investigation of N_2D^+ production in $N_2^+ - D_2$ collisions, B.R. Turner, M.A. Fineman and R.F. Stebbings, *J.Chem.Phys.*, **42**(12), 4088-4098, (1965).
- 86 A crossed beam apparatus for investigation of ion-molecule reactions, Z. Herman, J.D. Kerstetter, T.L. Rose and R. Wolfgang, *Rev.Sci.Instrum.*, **40**(4), 538-544, (1969).
- 87 A hybrid tandem supersonic beam mass spectrometer for the study of collision induced dissociation of ions in the energy range <1 to 3000eV, A.K. Shukla, S.G. Anderson, S.L. Howard, K.W. Schilberg, and J.H. Futrell, *Int. J. Mass. Spec. Ion Proc.*, **88**, 81-82, (1988).
- 88 New crossed beam apparatus for the study of ion-molecule collision processes, M.L. Vestal, C.R. Blakley, P.W. Ryan, and J.H. Futrell, *Rev.Sci.Instrum.*, **47**(1), 15-26, (1976).
- 89 A crossed beam apparatus for ion molecule reactions with negative ions, D. Vogt, J. Mischke, and W. Dreves, *J.Phys.E.*, **9**, 38-40, (1976).
- 90 Vibrationally resolved inelastic and charge transfer scattering of H^+ by H_2O , B. Friedrich, G. Niedner, M. Noll and J.P. Toennies, *J.Chem.Phys.*, **87**(8), 5256-5265, (1987).
- 91 The present instrument was commissioned between 1965 and 1968 by Shell (Thornton).
- 92 Kinematics of charge transfer: $Ar^+ \leftarrow H_2$, P.M. Hierl, V. Pacak and Z. Herman, *J.Chem.Phys.*, **67**(8), 2678-2686, (1977).
- 93 Crossed beam study of the reaction of H_2^+ (CO,H) HCO from 0.74 to 9.25 eV, R.M. Billotta, F.N. Preuninger, and J.M. Farrar, *J.Chem.Phys.*, **72**(2), 1583-1592, (1980).
- 94 Scattering of positive ions by molecules, W.S. Koski, *Adv. Chem. Phys.*, **30**, 185-247, (1978).
- 95 Beam studies of ion-molecule reactions, Z. Herman and R. Wolfgang ch12 in *Ion-molecule reactions*, Ed J.L. Franklin **2**, 533-599, Butterworths London, (1972).
- 96 *Interaction between ions and molecules*, Ed P. Ausloos, Plenum, New York, (1975).
- 97 International review of science, Ch. 2, B.H. Mahan, *Physical Chem. series 2*, **9**, 25-66, Butterworths London. (1976).
- 98 The calculation and measurement of cross sections for rotational and vibrational excitation, J.P. Toennies, *Ann. Rev. Phys. Chem.*, **27**, 225-280, (1976).
- 99 Energy and chemical reaction 2: Intermediate complexes vs direct mechanisms, R.Wolfgang, *Acc.Chem.Res.*, **3**, 48-54, (1970).

- 100 Crossed beam studies of low energy proton transfer reactions: $H_2^+(Ar,H)HAr^+$ from 0.4 to 7.8 eV (CM). R.M. Billotta, F.N. Preuninger, and J.M. Farrar, *J.Chem.Phys.*, **73**(4), 1637-1648, (1980).
- 101 On the competitive roles of reagent vibration and translation in exothermic proton transfer reactions: $H_2^+ + Ar \rightarrow HAr^+ + H$, R.M. Billotta and J.M. Farrar, *J.Chem.Phys.*, **74**(3), 1699-1706, (1981).
- 102 Energetic and angular studies of ArD^+ and N_2D^+ formation, L.D. Doverspike, R.L. Champion and T.L. Bailey, *J.Chem.Phys.*, **45**(12), 4385-4392, (1966).
- 103 Low energy crossed beam study of the endothermic charge transfer reaction $H_2^+(Ar,H_2)Ar^+$, R.M. Billotta, F.N. Preuninger, and J.M. Farrar, *Chem. Phys. Letters*, **74**(1), 95-100, (1980).
- 104 Dynamics of the reaction $H_2^+(He,H)HeH^+$: endoergic channels with H_2^+ in $v=0,1$ vibrational states: Beam experiment and trajectory calculations, V. Pacak, U. Havemann, Z. Herman, F. Schneider and L. Zullcke, *Chem. Phys. Letters*, **48**(2), 273-276, (1977).
- 105 Dynamics of the reaction $H_2^+(He,H)HeH^+$: Total cross sections: comparison of quasiclassical trajectory results with molecular beam data, F. Schneider, U. Havemann, L. Zullcke, and Z. Herman, *Chem. Phys. Letters*, **48**(3), 439-442, (1977).
- 106 State selected ion-molecule reactions: $N_2^+(v) + H_2 \rightarrow N_2 + H_2^+$ and $Ar^+(2P_j) + H_2 \rightarrow Ar + H_2^+$, G. Henri, M. Lavollee, O. Dufuit, J.B. Ozenne, P.M. Guyon and E.A. Glasson, *J.Chem.Phys.*, **88**(10), 6361-6369, (1988).
- 107 Chemische reaktionskinematik XV. Winkel und geschwindigkeitsverteilung des produkt ions der reaction $Kr^+ + D_2 \rightarrow KrD^+ + D$, G. Bosse, A. Ding and A. Henglein, *Z. Naturforsch.*, **26a**, 932-933, (1971).
- 108 Isotope effects upon the kinetics of ion-molecule reactions $Kr^+ + HD$, S. Chivatsak and P.M. Hienl, *Chem. Phys. Letters*, **45**(1), 99-102, (1977).
- 109 Low energy crossed beam study of the reaction $H_2^+ + Ne \rightarrow NeH^+ + H$, R.M. Billotta and J.M. Farrar, *J.Chem.Phys.*, **78**(4), 1776-1783, (1981).
- 110 Molecular beam studies of internal excitation of reaction products, D.R. Herschbach, *Appl. Opt. Suppl.*, **2**, 128-144, (1965).
- 111 Production of a Hg^+ beam in selected vibrational states, Z. Herman and V. Pacak, *Int. J. Mass Spectrom Ion Phys.*, **24**, 355-358, (1977).
- 112 A crossed beam study of the reaction of CO^+ with O_2 , M.F. Jarrold, K.R. Birkinshaw and D.M. Hirst, *Mol. Phys.*, **39**(4), 767-788, (1980).

- 113 A crossed beam study of the reaction of $\text{CO}^+ + \text{NO} \longrightarrow \text{CO}_2^+ + \text{N}$, M.F. Jarrold and D.M. Hirst, *Mol. Phys.*, **40**(5), 1197-1207, (1980).
- 114 A crossed beam study of the reaction of $\text{CO}^+ + \text{NO} \longrightarrow (\text{NCO})^+ + \text{O}$, M.F. Jarrold and D.M. Hirst, *Mol. Phys.*, **42**(1), 97-107, (1981).
- 115 Low Energy ion-neutral reactions $\text{VO}_2^+ + \text{NO}$, $\text{N}_2^+ + \text{NO}$, $\text{CO}^+ + \text{NO}$, $\text{N}_2^+ + \text{O}_2$, $\text{CO}_2^+ + \text{O}_2$, $\text{CO}^+ + \text{O}_2$, and $\text{N}_2^+ + \text{CO}$, N. Kobayashi and Y. Kaneko, *J. Phys. Soc. Japan*, **37**(4), 1082-1088, (1974).
- 116a Gas-phase nucleophilic displacement reactions, W.N. Olmstead, J.I. Brauman, *J. Am. Chem. Soc.*, **99**, 4219-4228, (1977).
- 116b Intrinsic barriers in nucleophilic displacements, M.J. Pelierite and J.I. Brauman, *102*, 5993-5999, (1980).
- 117 Vibrational and translational energy effects in the abstraction and exchange reactions of NH_3^+ with D_2 , J.W. Winniczek, A.L. Braveman, M.H. Shen, S.G. Kelley and J.M. Farrar, *J. Chem. Phys.*, **86**(5), 2818-2826, (1987).
- 118 Chemical reaction kinematics XVIII: Reactions of NH_3^+ , NH_2^+ and NH^+ with hydrogen and of N^+ with HD , G. Eisele, A. Hanglein, P. Botschwina and W. Meyer, *Ber. Bunsenges.*, **78**(10), 1090-1097, (1974).
- 119 Reactive scattering from double minimum potentials, W.R. Creasy and J.M. Farrar, *Faraday Discuss. Chem. Soc.*, **84**, 261-282, (1987).
- 120 Reactive scattering from double minimum potentials: Li^+ catalysed elimination reactions of alkyl halides, W.R. Creasy and J.M. Farrar, *J. Chem. Phys.*, **87**(8), 5280-5293, (1987).
- 121 Reactive scattering from double minimum potentials: Energetics and mechanism of the gas phase dehydration reaction of lithium ion with tert-butylalcohol, W.R. Creasy and J.M. Farrar, *J. Chem. Phys.*, **85**(1), 162-178, (1986).
- 122 Intrinsic barriers in gas-phase dehydration reactions an experimental probe, W.R. Creasy and J.M. Farrar, *J. Phys. Chem.*, **89**(19), 3952-3955, (1985).
- 123 P.J. Derrick, J.N. Murrell, M.R. Levy, K.A. Holbrook, M.T. Bowers, D.C. Clary and J.M. Farrar, *Faraday Discuss. Chem. Soc.*, **84**, 298-302, (1987).
- 124 Crossed-molecular beam studies of the state-to-state reaction dynamics of charge transfer reactions at low and intermediate energy, J.H. Futrell, *Int. J. Quantum Chem.*, **31**, 133-159, (1987).
- 125 Crossed molecular beam studies of charge transfer reactions at low and intermediate energies, J.H. Futrell, *Nato ASI Ser. Ser. C*, **183**, 67-80, (1986).
- 126 A crossed beam study of the reactive scattering and unreactive scattering of $\text{Ar}^+(\text{}^2\text{P}_{3/2})$ and $\text{Ar}^+(\text{}^2\text{P}_{1/2})$ by N_2 at low energies, K.R. Birkinshaw,

- A.K. Shukla, S. Howard and J.H. Futrell, *Chem. Phys.*, **112**, 149-158, (1987).
- 127 Quenching of $\text{Ar}^+(\text{2P}_{1/2})$ at high pressures in an electron-impact ion source. K.R. Birkinshaw, A.K. Shukla, S. Howard, J. Biggerstaff and J.H. Futrell, *Int. J. Mass. Spec. Ion Proc.*, **84**, 283-292, (1988).
- 128 General features of the reaction dynamics of charge-transfer reactions as revealed by the crossed-molecular beam method, S. Howard, Y.T. Long, K.R. Birkinshaw, A.K. Shukla, A. Rockwood and J.H. Futrell, *J. Mol. Sci.*, **4(3)**, 307-309, (1986).
- 129 Molecular dynamic studies of the charge-transfer reaction $\text{Ar}^+(\text{2P}_{3/2}) + \text{N}_2(\text{1}\Sigma_g) \rightleftharpoons \text{N}_2^+(\text{2}\Sigma_g) + \text{Ar}(\text{1S}_0)$ at low and intermediate energies, S. Howard, Y.T. Long, K.R. Birkinshaw, A.K. Shukla, A. Rockwood and J.H. Futrell, *J. Mol. Sci.*, **4(3)**, 307-309, (1986).
- 130 Crossed-beam study of the charge-transfer reaction of helium ions with xenon, S. Howard, A. Rockwood, S. Anderson, F. Howorka and J.H. Futrell, *Phys. Rev. A*, **37(8)**, 3211-3217, (1988).
- 131 Differential cross sections for the competing charge-transfer reactions $\text{Kr}^+(\text{2P}_{3/2}) + \text{Kr}(\text{1S}_0) \rightarrow \text{Kr}(\text{1S}_0) + \text{Kr}^+(\text{2P}_{3/2})$ and $\text{Kr}^+(\text{2P}_{3/2}) + \text{Kr}(\text{1S}_0) \rightarrow \text{Kr}(\text{1S}_0) + \text{Kr}^+(\text{2P}_{1/2})$, S.L. Howard, A.L. Rockwood, W. Trafton, B. Friedrich, S.G. Anderson, and J.H. Futrell, *Can. J. Phys.*, **65**, 1077-1081, (1987).
- 132 Observation of fine-structure transitions in rare gas charge-transfer at surprisingly low energies using a crossed-molecular beam technique, S.L. Howard, A.L. Rockwood, W. Trafton, B. Friedrich, S.G. Anderson, and J.H. Futrell, *Chem. Phys. Letters*, **140(4)**, 385-388, (1987).
- 133 Crossed-beam investigation of the single-electron charge transfer process $\text{Kr}^{2+} + \text{He} \rightarrow \text{Kr} + \text{He}^+$ at sub eV collision energies, B. Friedrich, J. Vancura and Z. Herman, *Int. J. Mass. Spec. Ion Proc.*, **80**, 177-185, (1987).
- 134 Dynamics of charge transfer $\text{Ar}^{2+}(\text{3P}) + \text{He}(\text{1S}) \rightarrow \text{Ar}^+(\text{2P}) + \text{He}^+(\text{2S})$ at low collision energies: comparison of experimental results with quasi-classical calculations of the differential cross sections, B. Friedrich, B. Pick, L. Hladek, Z. Herman, E.E. Nikitin, A.I. Reznikow, and S. Ya. Urmanik, *J. Chem. Phys.*, **84**, 807-812, (1986).
- 135 A crossed beam study of the single-charge transfer process $\text{Hg}^{2+}(\text{1S}) + \text{Kr}(\text{1S}) \rightarrow \text{Hg}^+(\text{2S}) + \text{Kr}^+(\text{2P}_{3/2}, \text{2P}_{1/2})$ at eV collision energies, B. Friedrich, J. Vancura, M. Sadilvek and Z. Herman, *Chem. Phys. Letters*, **120**, 243-246, (1985).
- 136 Collision complexes in the reaction of CH_3^+ with C_2H_4 and C_2H_2 , D.M. Sanneniroh and J.M. Farrar, *J. Chem. Phys.*, **88(12)**, 7167-7177, (1988).

Chapter 2 references

- 137 Edwards EDM12, $14.6\text{m}^3\text{hr}^{-1}$, charged with Edwards nR. 15 mechanical pump oil
- 138 Edwards 1101 controller and pirani 1001 modules using pirani PRH10K gauge heads.
- 139 Edwards thermocouple TC1 and thermocouple 1 gauge heads.
- 140 Monsanto (Chemical) company St. Louis Missouri 63167, USA. Available from ref. 156.
- 141 Ionisation gauge Edwards VIG 20.
- 142 Ionisation gauge Edwards VIG 8.
- 143 Vacuum Generators, Menzies Rd, Hastings, East Sussex. TN34 1YQ.
- 144 Edwards diffstat Mk2 model M100-300 111mm throat diameter, pumping speed 300 l s^{-1} for air. Edwards high vacuum, Crawley, Sussex.
- 145 See Figure 4.2. *Single structure vapour pumping groups*, B.D. Power, N.T.M. Dennis, R.D. Oswald, B.H. Colwell, *Vacuum*, **24(3)**, 117-122, (1974).
- 146 Edwards diffstat Mk2 model 250-1700 251mm throat diameter pumping speed 1700 l s^{-1} for air. Edwards High Vacuum, Crawley, Sussex.
- 147 Thor Industrial Cryogenics, model 5050 cryogenic level controller with Peter Paul Electronics Co. Inc. valve 22X00640CM.
- 148 Model SSV200 dewar. Statebourne Cryogenics, 18, Parsons Rd, Washington, Tyne & Wear, NE37 1EZ.
- 149 See Chapter 4 of this work.
- 150 Edwards E2M12, $14.6\text{m}^3\text{hr}^{-1}$, charged with Edwards nR. 15 mechanical pump oil
- 151 Saunders valve speedvac 1", Edwards.
- 152 Edwards IG5M with fast preamplifier ref. 17.
- 153 *Fast pulsed gas valve* C.J. Keyser, M. Dembicki and P.K. John, *Rev. Sci. Instrum.*, **51**, 425-426, (1980).
- 154 Thurlby model DSA524 digital storage oscilloscope adapter, RS Components Ltd., P.O.Box 89, Corby, Northants, NN17 9RS. Gould model OS300 Oscilloscope.
- 155 North London Valve and Fitting Company Ltd., 56, Edgware Way, Edgware, Middlesex HA8 5JP.
- 156 Laik Engineering Ltd., Albert Drive, Burgess Hill, West Sussex, BN15 9NX.

- 157 Northern Scientific (York), 93, The village, Haxby, York, YO3 6JE.
- 158 Suhner Electronics Ltd, Telford Rd, Bicester, Oxon, OX6 0LA.11 SHV-50-3-10C, 34 SHV-50-0-3, 22 SHV-50-0-3, RG142 A/U
- 159 Private communication, R&D labs (24-25/11/88) via: Vacuum Generators (components) Ltd., Maunsell Rd, Castleham Industrial Estate, St. Leonards-on-sea, East Sussex. TN38 9NN.
- 160 "Physical Chemistry", 3rd, P.W. Atkins, . Oxford University Press, (1987).
- 161 Chell Baratron 220BHS-3A1-B-10. Chell Instruments Ltd., Tudor House, Grammar School Lane, North Walsham, Norfolk NR28 9JH.
- 162 Chell solenoid operated leak valve model 248A-V-1000.
- 163 Chell Mks Baratron, PDR-C-1B and 250A Pressure/Flow Controller.
- 164 Sims/Mass analyst 200: Vacuum Science Workshop Scientific Instruments Ltd., Warwick Rd South, Old Trafford, Manchester, M16 0JT.
- 165 Mullard X919BL channel electron multiplier. Supplied by Alrad Instruments Ltd., Turnpike Rd Industrial Estate, Newbury, RG13 2NS.
- 165a *The channeltron electron multiplier, a new radiation detector*, J. Adams and B.W. Manley, *Philips Tech. Rev.*, 58(5-6-7), 156-161, (1987).
- 165b *Low energy charged-particle detector using the continuous-channel electron multiplier*, D.S. Evans, *Rev. Sci. Instrum.*, 38(3), 375-382, (1965).
- 166 Swallow Metals and Components Ltd., Theale technology centre, Theale, Berkshire, RG7 4NW.
- 167 Tektronics oscilloscope camera model CR5B and T812 oscilloscope.
- 168 *The focussing of an ion beam from a quadrupole mass filter using an electrostatic octopole lens*, K. Birkinshaw, D.M. Hirst and M.F. Jarrold, *J. Phys. E*, 11, 1037-1040, (1981).
- 169 Galileo Electro Optics Scintered glass capillary array H25S05M05.
- 170 Farnell Electronic Components Ltd., Canal Rd, Leeds, LS12 2TU.
- 171 "Applied Probability and Statistical methods", G.C. Canavos, Little-Brown, (1984).
- 172 Goodfellow Cambridge Science Park, Milton Rd, Cambridge, CB4 4DJ.
- 173 7100/APPLE/01A Data transfer routines for Ortec 7100 MCA and the Apple IIe, D.J. Cutler, (1984).

Chapter 3 references

- 174 "Electron optics", 3rd, O. Klemperer and M.E. Barnett, Cambridge University Press, (1971).
- 175 "Electron beams: lenses and optics", (1.2), A.B. El-Kareh and J.C.J. El-Kareh, Academic press, (1970).
- 176 SIMION 3.0, D.A. Dahl, EG&G (Idaho), Idaho state, USA. (Version 4.02 in full 3D is now available).
- 177 Formation, trajectories and collisions of beams of multiatomic ions, S.C. Davis, PhD Thesis, University of New South Wales, (1988).
- 178 The quadrupole mass filter: Basic operating concepts, P.E. Miller and M.B. Denton, J. Chem. Ed., 63(7), 617-622, (1986).
- 179 "Quadrupole mass spectrometry and its applications", Ed. P.H. Dawson, Elsevier, New York, (1976).
- 179a Radiofrequency quadrupole mass spectrometers, P.H. Dawson, Adv. Elec. Electron. Phys., suppl. 13B, 173-256, (1980).
- 180 Radio frequency quadrupole mass spectrometers, G. Lawson and J.F.J. Todd, Chem.Br., 8(9), 373-380, (1972).
- 180a Quadrupole mass spectrometry, G.F. Lawson and J.F.T. Todd, Int. Rev. Sci. (mass spec.) Phys. Chem. ser. 2, 2, 291-394, (1975).
- 181 Pages 60 and 78, Technical manual, VSW Mass Analyst, VSW Scientific Instruments Ltd., Warwick Road South, Old Trafford, Manchester, M16 0JT.
- 182 Development of a SIMS apparatus and its application to the analysis of insulating and other surfaces, M.G. Dowsett, PhD thesis, (1977). Department of Physics, Sir John College of Science and Technology, London.
- 183a The acceptance of the quadrupole mass filter, Int. J. Mass Spectrom. Ion Phys., 17, 423-445, (1975). P.H. Dawson
- 183b Fringing fields in the quadrupole mass filter, Int. J. Mass Spectrom. Ion Phys., 2, 33-44, (1971). P.H. Dawson
- 183c Quadrupole mass filters with varying Mathieu parameters, Int. J. Mass Spectrom. Ion Phys., 21, 295-309, (1988). P.H. Dawson
- 184 An improved quadrupole mass analyser, W.M. Brubaker, Adv. in Mass Spectrom., 2, 293, (1987).
- 185 Transmission-resolution curves for a quadrupole mass spectrometer with separated rf and dc fields in the entrance aperture, H.F. Dylla, J.A. Jarrell, Rev. Sci. Instrum., 47(3), 331-333, (1976).

- 186 M.G. Dowsett, Private communication, 21/6/89, Department of Physics, University of Warwick, Coventry, CV4 7AL.
- 187 *Optimisation and performance of electrostatic particle analysers*, R. Jones, *Rev. Sci. Instrum.*, **49**(1), 21-23, (1978).
- 188 It is not possible to align the ion-beam source with the centre of the table.
- 189 After modifications to the ion source described on page 7, this test was seen to limit at 3.5 mA of electron emission. This is consistent with space charge limiting of the illuminated anode.
- 190 Hess' law: page 33 of ref. 159.

Chapter 4 references

- 191 *A high intensity source for the molecular beam part1: theoretical*, A. Kantrowitz and J. Gray, *Rev. Sci. Instrum.*, **22**, 328-332, (1951).
- 192 *A high intensity source for the molecular beam part2: experimental*, G. Kistiakowski and W.P. Slichter, *Rev. Sci. Instrum.*, **22**, 333-337, (1951).
- 193 "Molecular beams", Ed. J. Ross, *Adv. in Chem. Phys.*, **19**, 275, Interscience, (1966).
- 194 "Atomic and molecular beam methods", **1**, Ed. G. Scoles, Oxford University Press, Oxford, (1988).
- 195 "Molecular beams and low density gas dynamics" Ed. P.D. Wegener, Marcel Dekker Inc., New York (1974).
- 196 "Mechanics of fluids", 6th Edn., B.S. Massey, Van Nostrand Reinhold (International), London, (1989).
- 197a *Molekularstrahlrzeug mit Düsen im Impulsbetrieb*, O.F. Hagena, *Z. Angew. Phys.*, **18**, 183-187, (1964).
- 197b *Intensität und Geschwindigkeitsverteilung von gepulsten überschallmolekularstrahlen*, O.F. Hagena and P.G. Shuler, *Z. Angew. Phys.*, **17**, 542-547, (1964).
- 198 *Ten microsecond pulsed molecular beam source and a fast ionisation detector* W.R. Gentry and C.F. Giese, *Rev. Sci. Instrum.*, **49**(5), 595-605, (1978).
- 199 *A fast (30µs) pulsed supersonic beam source: Application to the photodissociation of CS₂ at 193nm*, M.D. Barry, N.P. Johnson and P.A. Gorry, *J. Phys. E*, **19**(10), 815-820, (1986).
- 200 *Versatile disturbance free electromagnetically driven supersonic beam source*, G. Sanna, M. Nardi and P. Cardoni, *Rev. Sci. Instrum.*, **58**(1), 28-31, (1987).
- 201 *High repetition rate pulsed nozzle beam source* J.B. Cross and J.J. Valentini, *Rev. Sci. Instrum.*, **53**, 38-42, (1982).

- 202 Pulsed metastable atomic beam source for time of flight applications A. Kohlhase and S. Kila, *Rev. Sci. Instrum.*, **57(12)**, 2925-2928, (1986).
- 203 Pulsed molecular beam source, D. Bassi, S. Iannotti and S. Nicolini, *Rev. Sci. Instrum.*, **52(1)**, 8-11, (1981).
- 203a A simple pulsed valve for use in supersonic nozzle experiments, C.E. Otis and P.M. Johnson, *Rev. Sci. Instrum.*, **51(8)**, 1128-1129, (1980).
- 204 Fluorescence excitation spectrum of the $^1A_u(n\pi^*) \leftarrow ^1A_g(0-0)$ band of oxaly fluoride in a pulsed supersonic free jet, M.G. Liverman, S.M. Beck, D.L. Monte, and R.E. Smalley, *J. Chem. Phys.*, **70(1)**, 192-197, (1979).
- 205 Dynamics of radiationless processes studied in pulsed supersonic free jets, F.M. Behien, N. Mikami and S. Rice, *Chem. Phys. Letts.*, **60(3)**, 364-367, (1979).
- 206 Pulsed molecular beams: A lower limit on pulse duration for fully developed supersonic expansions, K.L. Saenger, *J. Chem. Phys.*, **75(5)**, 2467-2469, (1981).
- 207 On the time taken to reach fully developed flow in pulsed supersonic free jets, K.L. Saenger and J.B. Fenn, *J. Chem. Phys.*, **79(12)**, 6043-6045, (1983).
- 208 Pulsed molecular beam experiments, W.R. Gentry, RGD, **14(2)**, 793-807, (1984). From the conference proceedings of the 14th International Symposium on Rarefied Gas Dynamics, Ed. H. Oguchi, University of Tokyo Press, Tokyo, (1984).
- 209 Low-energy pulsed beam sources, W.R. Gentry, chapter 3 in reference 194, 54-62, (1988).
- 210 "Engine emissions: pollutant formation and measurement", Ed. G.S. Springer and D.J. Patterson, chapter 9 (E. Knuth), *Direct sampling studies of combustion processes*, 319-363, (1983).
- 211 Nucleation and growth of clusters in expanding nozzle flows, O.F. Hagena, *Surface Sci.*, **100**, 101-116, (1981).
- 212 Cluster formation in free jets: results of theory and experiment, RGD, **14(2)**, 721-732, (1984).
- 213 High intensity supersonic molecular beam apparatus, R. Campargue, *Rev. Sci. Instrum.*, **25**, 111-112, (1984).
- 214 "Introduction to the theory and practice of high vacuum technology", L. Ward and J.P. Bunn, Butterworths, London, (1987).
- 215 Effective Separation of disparate mass mixtures in a single stage by double deflection separation nozzles, P. Bley, W. Ehrfield, and D. Schmidt, RGD, **14(2)**, 648-656, (1984).

- 216 *Absolute intensities and perpendicular temperatures of supersonic beams of polyatomic gases*, H.C.W. Beijerinck and N.F. Verster, *Physica*, 111(c), 327-352, (1981).
- 217 *Free jet sources*, D.R. Miller, chapter 2 in ref. 194, 14-53, (1988).
- 218 The velocity slip is the phenomenon where the heavier molecules in the expansion do not reach the predicted terminal velocity of the beam. For instance, a seeded beam, containing 10% Ar in 90% He would produce a higher terminal velocity (for Ar) than in the pure Ar expansion. The same ratio of 10% Xe in 90% He would not produce an equivalent percentage increase relative to pure Xe. The greater inertia of Xe means that the number of collisions required to accelerate the Xe is increased and it is said to be *velocity slipped*.

Appendix 2

Design Drawings

Contents in order:

Pulsed beam nozzle
Pulsed beam base plate
Pulsed beam pillars
Pulsed beam clamping jaws
Magnet pole pieces
Capillary array base plate
Pulsed beam box blanking flange
Stagnation pressure chamber
Stagnation chamber adjuster
Skimmers assembly location ring
Skimmers assembly location ring support plate No1
Skimmers assembly skimmers support plate No2
Skimmers assembly skimmers support plate No3
Skimmers assembly spacing rods
Skimmers and skimmers ring construction
Three part turret - top
Three part turret - bottom
Three part turret - front
Test rig layout
Base flange for the vacuum test-cell, FIG flange for
the vacuum test-cell
Test rig vacuum cell
Condensable vapours trap (for inlet trolley)

PULSED BEAM NOZZLE
THIRD ANGLE PROJECTION

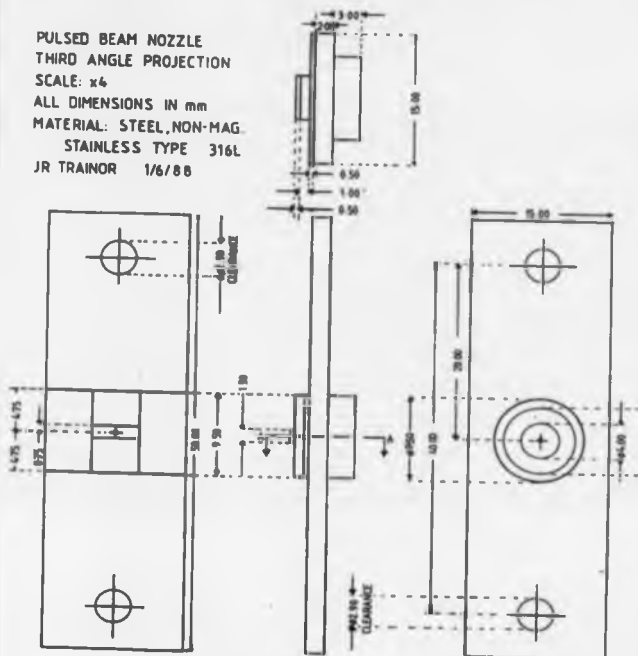
SCALE: x4

ALL DIMENSIONS IN mm

MATERIAL: STEEL, NON-MAG.

STAINLESS TYPE 316L

JR TRAINOR 1/6/88



NOTES:

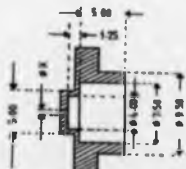
QUANTITY: 3 OFF

1x $\phi X = 0.50$

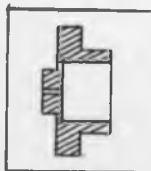
1x $\phi X = 0.60$

1x $\phi X = 0.00$

METHOD: SPARK EROSION



AA SECTION



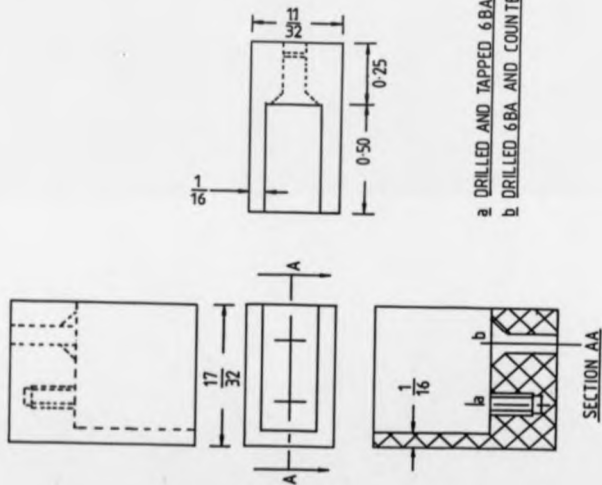
PULSED BEAM
PILLARS

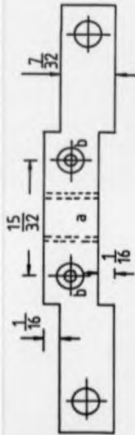
DRAWN JR TRINOR
FROM THE DESIGN
OF GORRY
16/1/90

THIRD ANGLE PROJECTION
SCALE: x4

DIMENSIONS IN INCHES

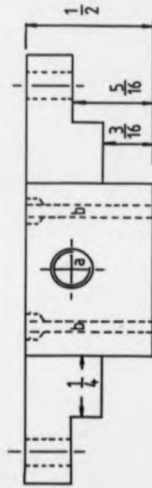
FOUR OFF





UPPER MANDIBLE

2x 216L ST'SS
STEEL



PULSED BEAM CLAMPING JAWS

DRAWN JR TRINOR FROM
THE DESIGN OF GORRY

16/11/90

THIRD ANGLE PROJECTION

SCALE $\times 4$

DIMENSIONS IN INCHES

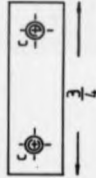
- a DRILL AND TAP 4BA
- b DRILL AND COUNTER SINK
8 BA (CLEAR)
- c DRILL AND TAP 8 BA

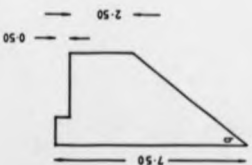
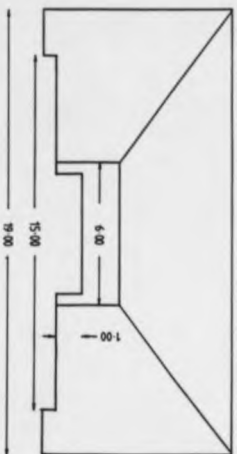
2x VITON IMPREGNATED
WITH GLASS FIBRE



LOWER MANDIBLE

2x PECK





NOTES:

ANGLES ARE 31.6° AND 47.4°
JOB - 2 OFF.

MAGNET POLE PIECE

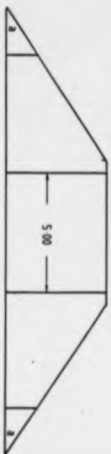
THIRD ANGLE PROJECTION

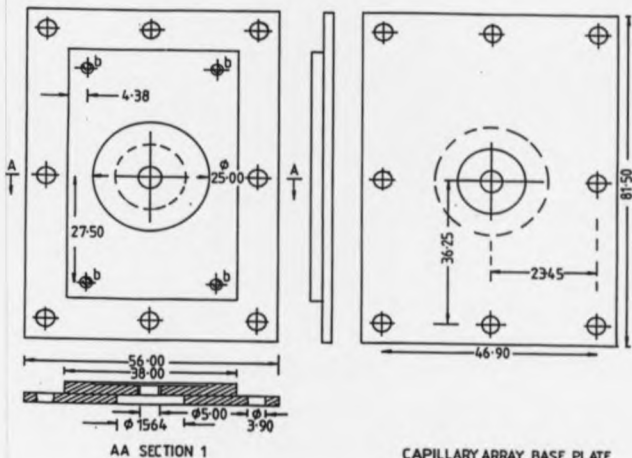
SCALE: X10

ALL DIMENSIONS IN MM

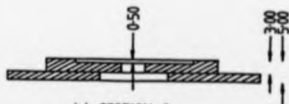
MATERIAL: MILD STEEL

JR. TRAINDOR 15/9/88





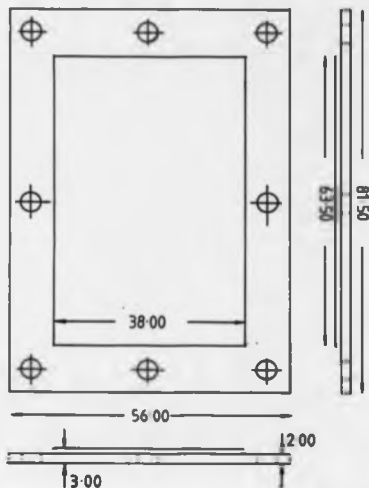
AA SECTION 1



AA SECTION 2

CAPILLARY ARRAY BASE PLATE
THIRD ANGLE PROJECTION
SCALE: x2 ALL DIM. IN mm
MATERIAL NON-MAG. STAINLESS
STEEL TYPE EN 58J
JR TRAINOR 5/5/89

NOTES:
ALL HOLES MARKED b
ARE DRILLED & TAPPED
6BA at 4.00 mm AND MUST
NOT BREAK THROUGH



PULSED BEAM BOX
BLANKING FLANGE

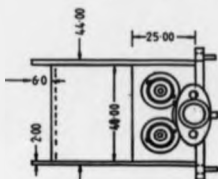
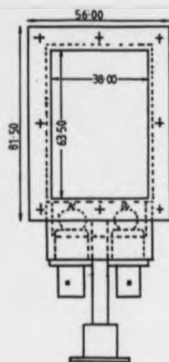
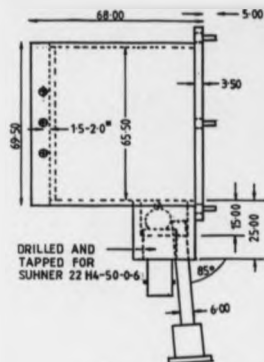
THIRD ANGLE PROJECTION

SCALE x2

MATERIAL: 316L

ALL DIM. - mm

JR TRAINOR 3/3/88



STAGNATION PRESSURE CHAMBER

JR TRAINOR 3/3/88

THIRD ANGLE PROJECTION

MATERIAL: 316L NON-MAGNETIC
STAINLESS STEEL

DIM.-mm SCALE: x1

*DEPENDS ON BOX AFTER WELDING
AND THE ADJUSTER

STAGNATION CHAMBER

ADJUSTEE:

JR TRAINOR

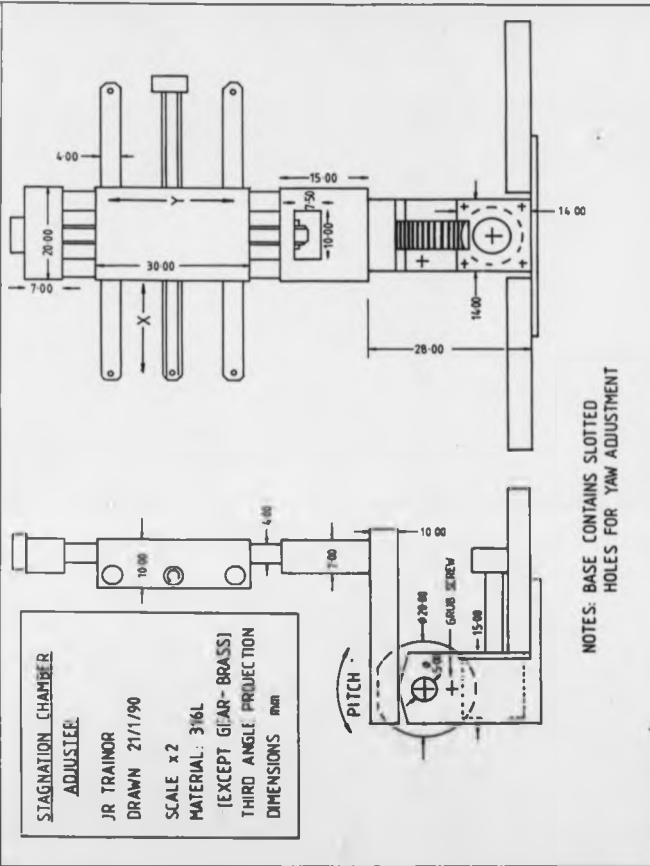
DRAWN 21/1/90

SCALE x2

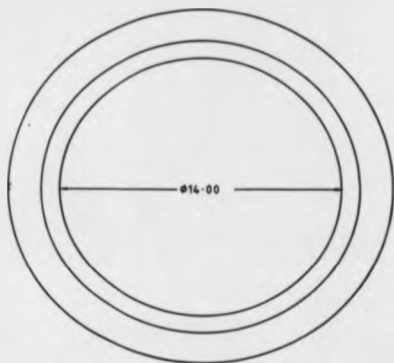
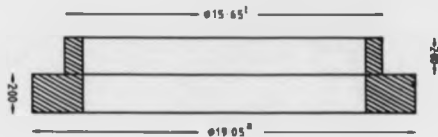
MATERIAL: 316L

(EXCEPT GEAR-BRASS)

THIRD ANGLE PROJECTION
DIMENSIONS mm



NOTES: BASE CONTAINS SLOTTED
HOLES FOR YAW ADJUSTMENT



NOTES

- a - THIS DIMENSION IS OVERSIZE FOR PUSH FITTING INTO THE "SKIMMERS BASE PLATE"
- b - MACHINE TO AN EXACT FIT TO THE "PLATED BEAM BASE PLATE"

SKIMMERS ASSEMBLY

LOCATION RING

SCALE x8

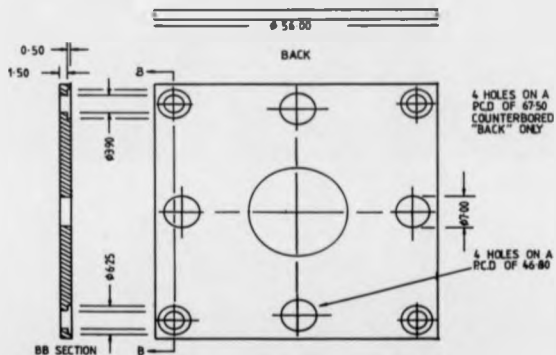
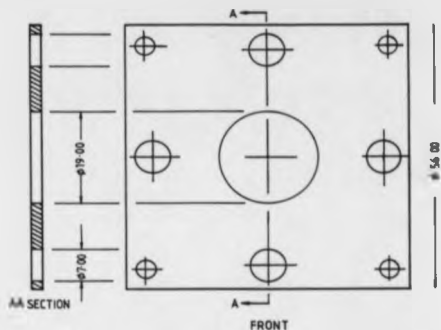
ALL DIMENSIONS IN mm

MATERIAL: STEEL, NON-MAG

STAINLESS TYPE 316L

JR TRAINOR 11/8/88

THIRD ANGLE PROJECTION

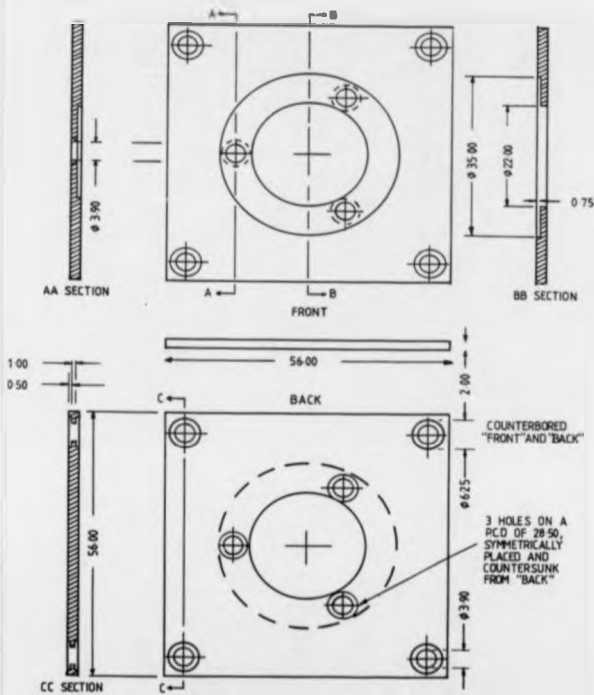


SKIMMERS ASSEMBLY LOCATION RING SUPPORT NO 1 PLATE

SCALE x2 ALL DIMENSIONS IN mm

MATERIAL NON MAG STAINLESS STEEL TYPE 316L

JR TRAINER 11/9/88 THIRD ANGLE PROJECTION

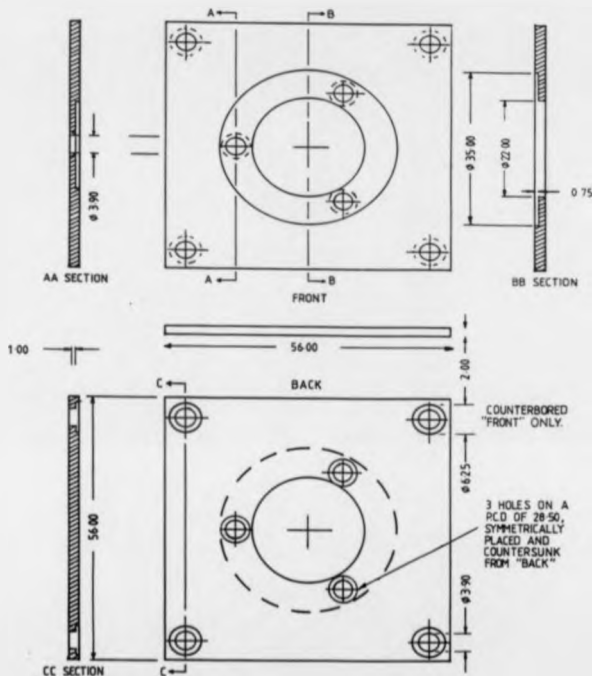


SKIMMERS ASSEMBLY SKIMMER SUPPORT NO 2 PLATE

SCALE: x2 ALL DIMENSIONS IN mm

MATERIAL STEEL NON-MAG STAINLESS TYPE 316L

JR TRAINOR 11/9/88 THIRD ANGLE PROJECTION



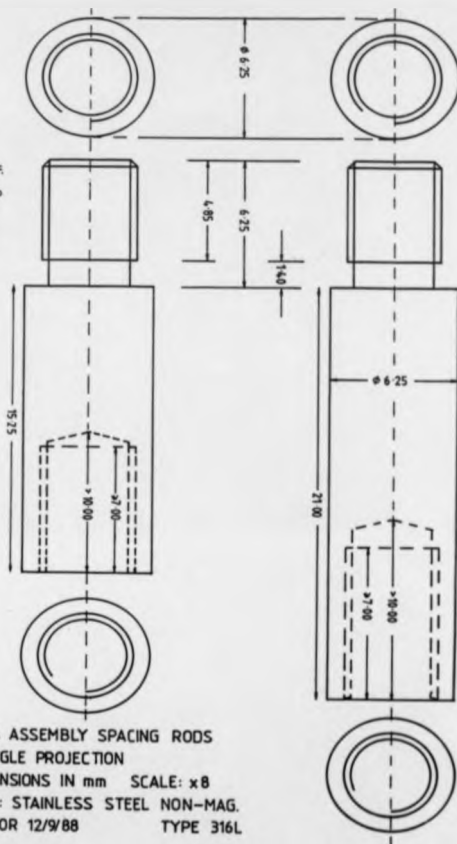
SKIMMERS ASSEMBLY SKIMMER SUPPORT NO 3 PLATE

SCALE: x2 ALL DIMENSIONS IN mm

MATERIAL: STEEL NON-MAG STAINLESS TYPE 316L

JR TRAINER 11/9/88 THIRD ANGLE PROJECTION

NOTES:
EACH ROD 4 OFF.
DRILL AND TAP
HOLES TO 6BA
TURN AND DIE
THE THREADS
TO FIT.



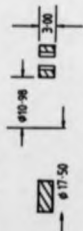
SKIMMERS ASSEMBLY SPACING RODS
THIRD ANGLE PROJECTION
ALL DIMENSIONS IN mm SCALE: x8
MATERIAL: STAINLESS STEEL NON-MAG.
JR TRAINOR 12/9/88 TYPE 316L

SKIMMER RINGS

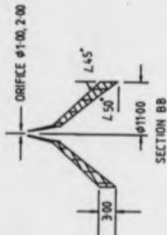
SKIMMERS



THREE HOLES
SYMMETRICALLY
PLACED ON A
CIRCLE OF 100
DIA. Holes
DRILLED AND
TAPPED 4 BA



SECTION A-A



SECTION B-B

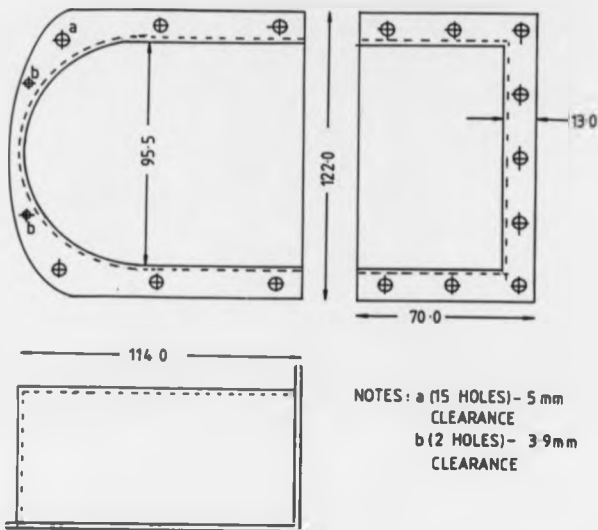
SKIMMER AND SKIMMER RING CONSTRUCTION

FROM THE DESIGN OF
SD KELLY

DRAWN JR TRAINER
15/1/90

SCALE x 2

THIRD ANGLE PROJECTION
ALL DIM. - mm

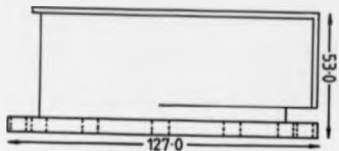
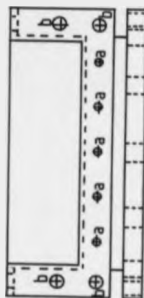
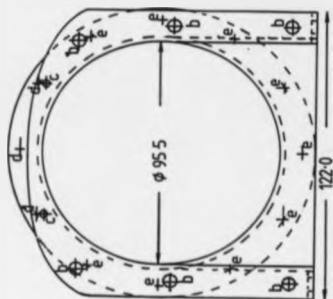


NOTES: a (15 HOLES) - 5 mm
CLEARANCE
b (2 HOLES) - 3.9 mm
CLEARANCE

THREE PART TURRET — TOP

JR TRAINOR
NON-MAG. STAINLESS STEEL - 316L
1 OFF

THIRD ANGLE PROJECTION
DIM - mm SCALE: x1



THREE PART TURRET — BOTTOM

JR TRAINOR
NON-MAG. STAINLESS STEEL - 316L
1 OFF

THIRD ANGLE PROJECTION
DIM — mm SCALE x1

NOTES: WELD THEN
MACHINE SEALING
SURFACE BACK

HOLES: a 4 BA TAP. BLIND

b 5mm CLEAR

c 4 BA CLEAR

d 7.5mm CLEAR

e 8 BA TAP. CLEAR

THREE PART TURRET -

FRONT

JR TRAINER 3/38

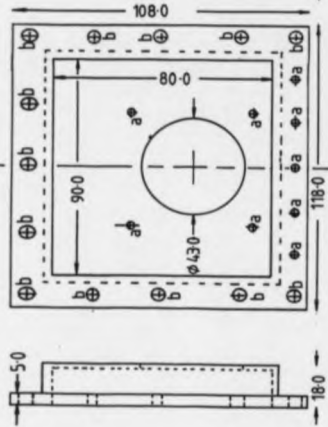
MATERIAL: 316L NON-MAG.
STAINLESS STEEL

1 OFF

THIRD ANGLE PROJECTION

DM. - mm

SCALE x1



NOTES: BACK MACHINE SEALING SURFACES AFTER WELDING.

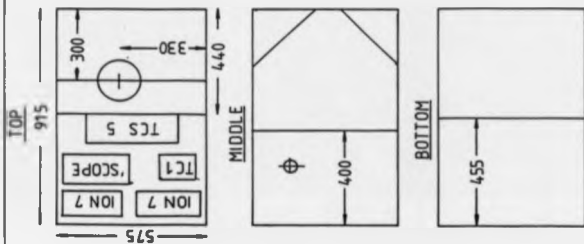
ALL HOLES ARE CLEARANCE

a - 6BA, b - 5mm

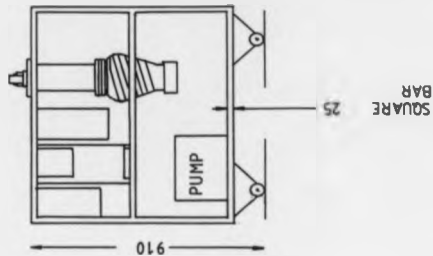
TEST RIG LAYOUT

JR TRAINER

REDRAWN 21/1/90



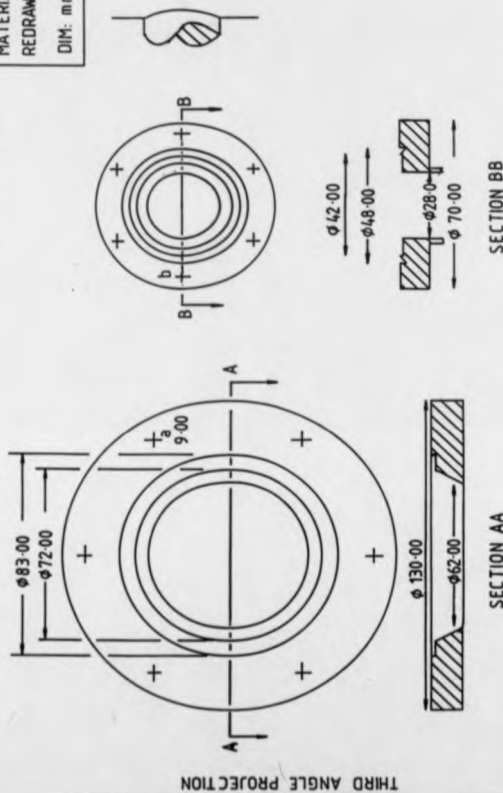
DIMENSIONS IN mm.



BASE FLANGE FOR THE
VACUUM TEST-CELL

FIG. FLANGE OF THE
VACUUM TEST-CELL

JR TRAINOR
MATERIAL: 316L
REDRAWN 21/1/90
DIM: mm



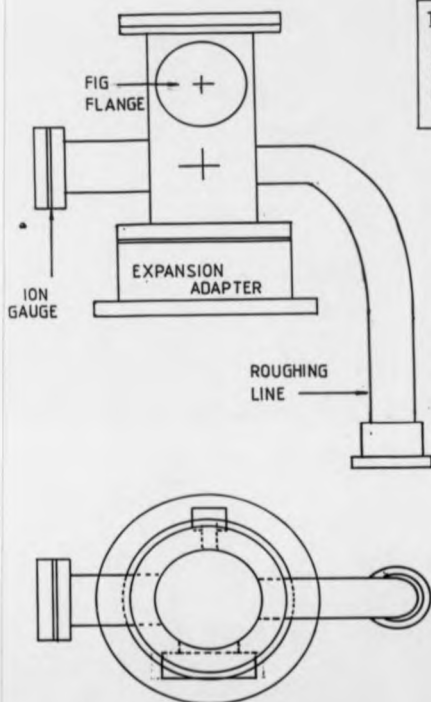
SECTION AA

SECTION BB

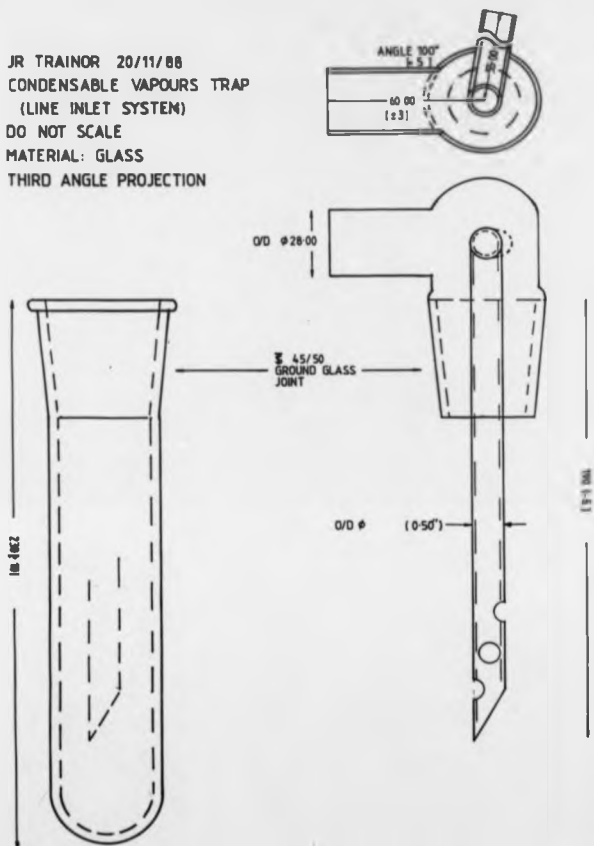
HOLES: a ON A PCD OF $\phi 11.40$ (9 HOLES), b CLEARANCE TAPPED 6.00 ON A PCD OF 58.40

TEST RIG VACUUM CELL

JR TRAINOR 22/1/90
FIRST ANGLE PROJECTION
ROUGH SCALE: $\times 0.5$



JR TRAINOR 20/11/88
 CONDENSABLE VAPOURS TRAP
 (LINE INLET SYSTEM)
 DO NOT SCALE
 MATERIAL: GLASS
 THIRD ANGLE PROJECTION



Appendix 3

Computer programs

These programs have been written in Applesoft basic and DOS 3.3. Source machine code routines are called from two libraries:

- 1. EG&G Ortec Apple IIe/7100/01A data transfer routines.**
- 2. Applesoft library routines.**

```

1 REM *****
2 REM *****
3 PRINT CHR$(4); "LOAD CHAIR AS20"
4 REM SAME AS MENU BUT WITH A MESSAGE
5 *****
6 *****
7 *****
8 *****
9 *****
10 *****
11 *****
12 *****
13 *****
14 *****
15 *****
16 *****
17 *****
18 *****
19 *****
20 *****
21 *****
22 *****
23 *****
24 *****
25 *****
26 *****
27 *****
28 *****
29 *****
30 *****
31 *****
32 *****
33 *****
34 *****
35 *****
36 *****
37 *****
38 *****
39 *****
40 *****
41 *****
42 *****
43 *****
44 *****
45 *****
46 *****
47 *****
48 *****
49 *****
50 *****
51 *****
52 *****
53 *****
54 *****
55 *****
56 *****
57 *****
58 *****
59 *****
60 *****
61 *****
62 *****
63 *****
64 *****
65 *****
66 *****
67 *****
68 *****
69 *****
70 *****
71 *****
72 *****
73 *****
74 *****
75 *****
76 *****
77 *****
78 *****
79 *****
80 *****
81 *****
82 *****
83 *****
84 *****
85 *****
86 *****
87 *****
88 *****
89 *****
90 *****
91 *****
92 *****
93 *****
94 *****
95 *****
96 *****
97 *****
98 *****
99 *****
100 *****

```

[illegible]

```

0 PRINT CH$ (4); "PARTILES"
1 REM *****
2 REM DATA PROCESSING
3 REM *****
4 LET CH$ = CH$ + CH$
5 LET CH$ = CH$ + CH$
6 LET CH$ = CH$ + CH$
7 LET CH$ = CH$ + CH$
8 LET CH$ = CH$ + CH$
9 REM *****
10 REM *****
11 REM *****
12 REM *****
13 REM *****
14 REM *****
15 REM *****
16 REM *****
17 REM *****
18 REM *****
19 REM *****
20 REM *****
21 REM *****
22 REM *****
23 REM *****
24 REM *****
25 REM *****
26 REM *****
27 REM *****
28 REM *****
29 REM *****
30 REM *****
31 REM *****
32 REM *****
33 REM *****
34 REM *****
35 REM *****
36 REM *****
37 REM *****
38 REM *****
39 REM *****
40 REM *****
41 REM *****
42 REM *****
43 REM *****
44 REM *****
45 REM *****

```

```

46 LET LB = CH$ / PEK (C) * PE = CH$ / PEK (C * 11)
47 LET PE = CH$ / PEK (C * 21) * CH = CH$ / PEK (C * 31)
48 LET CH = CH$ / PEK (C * 41) * CH = CH$ / PEK (C * 51)
49 LET LB = CH$ / PEK (C * 61) * CH = CH$ / PEK (C * 71)
50 LET LB = CH$ / PEK (C * 81) * CH = CH$ / PEK (C * 91)
51 LET C = C * 9
52 LET C = C * 9
53 PRINT CH$ (4); "WHITE Data record R" COUNT
54 LET TEMP = COUNT / INT (VAL (UTIME/60))
55 PRINT TEMP / COUNT
56 IF TEMP / COUNT / 58 THEN LET SR = TEMP / COUNT
57 PRINT COUNT
58 PRINT SR
59 RETURN
60 REM *****
61 REM *****
62 REM *****
63 REM *****
64 PRINT CH$ (4); "WHITE Data record R" COUNT
65 PRINT CH$ (4); "WHITE Data record R" COUNT
66 PRINT CH$ (4); "WHITE Data record R" COUNT
67 PRINT CH$ (4); "WHITE Data record R" COUNT
68 LET C = COUNT * C * 1
69 LET A1 = TEMP * C
70 LET SR = A1 * B1
71 LET SR = A1 * B1
72 LET SR = A1 * B1
73 LET SR = A1 * B1
74 PRINT CH$ (4); "WHITE Data record R" COUNT
75 PRINT CH$ (4); "WHITE Data record R" COUNT
76 PRINT CH$ (4); "WHITE Data record R" COUNT
77 PRINT CH$ (4); "WHITE Data record R" COUNT
78 PRINT CH$ (4); "WHITE Data record R" COUNT
79 PRINT CH$ (4); "WHITE Data record R" COUNT
80 PRINT CH$ (4); "WHITE Data record R" COUNT
81 PRINT CH$ (4); "WHITE Data record R" COUNT
82 PRINT CH$ (4); "WHITE Data record R" COUNT
83 PRINT CH$ (4); "WHITE Data record R" COUNT
84 PRINT CH$ (4); "WHITE Data record R" COUNT
85 PRINT CH$ (4); "WHITE Data record R" COUNT
86 PRINT CH$ (4); "WHITE Data record R" COUNT
87 PRINT CH$ (4); "WHITE Data record R" COUNT
88 PRINT CH$ (4); "WHITE Data record R" COUNT
89 PRINT CH$ (4); "WHITE Data record R" COUNT
90 PRINT CH$ (4); "WHITE Data record R" COUNT

```

[illegible]

THE BRITISH LIBRARY DOCUMENT SUPPLY CENTRE

TITLE Development of a crossed beam instrument
for studying ion-molecule
reactions

AUTHOR John Roland Trainor

INSTITUTION
and DATE University of Warwick
1970

Attention is drawn to the fact that the copyright of
this thesis rests with its author.

This copy of the thesis has been supplied on condition
that anyone who consults it is understood to recognise
that its copyright rests with its author and that no
information derived from it may be published without
the author's prior written consent.

THE BRITISH LIBRARY
DOCUMENT SUPPLY CENTRE

Boston Spa, Wellesley
West Yorkshire
United Kingdom



REDUCTION X

20

CAMERA

3